

國立臺灣大學 理學院化學系(所)

博士論文

Department or Graduate Institute of Chemistry

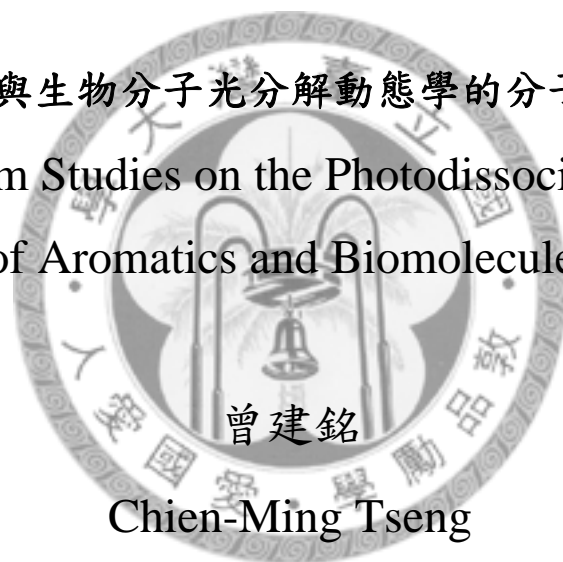
College of Science

National Taiwan University

Doctoral Dissertation

芳香族與生物分子光分解動態學的分束研究

Molecular Beam Studies on the Photodissociation Dynamics  
of Aromatics and Biomolecules



曾建銘

Chien-Ming Tseng

指導教授：李遠哲 教授

倪其焜 教授

Advisor: Yuan-Tseh Lee, Ph.D.

Chi-Kung Ni, Ph.D.

中華民國 97 年 7 月

July, 2008

## 摘要

利用多重離子影像技術來研究芳香族以及生物分子。對於苯胺(Aniline)、四甲基吡啶(4-methyl-pyridine)以及酚(Phenol)的光致異構與光致分解機構的探究。實驗觀測到許多分解途徑包含有出口能障與無出口能障的基態分解，以及沿著N-H/O-H鍵長的激發態分解。關於”七員環異構化”機構有所討論並且與甲苯做比較。這一系列研究幫助我們了解芳香族分子在照射紫外光後可能發生的反應。芳香族及生物分子在吸收紫外光後躍遷  $\pi\pi^*$  電子激發態經過位能面上二個不同的圓錐型交叉點(conical intersections)，分子過渡到  $\pi\sigma^*$  電子激發態，該相斥的位能面使得分子快速分解並且有極快的碎片動能分佈。此一反應途徑被認為是有O-H或N-H官能基的(氨基酸，DNA鹼基等)照射紫外光後的新典範。對於phenol與1-naphthol的光分解研究來測試上述反應機構。更進一步我們對於p-methylphenol, p-ethylphenol, phenylethylamine以及p-(2-Aminoethyl)phenol研究去了解不同官能基對於發光團的光分解動態學所扮演的角色。包含內轉換(internal conversion)，系統間跨越(intersystem crossing)與上述  $\pi\sigma^*$  分解反應途徑的相互競爭。此外，對於以吲哚(indole)為發光團(chromophore)的3-methylindole，tryptamine與色氨酸(tryptophan)也作了探討。左旋色氨酸(L-tryptophan)的光分解動態學可能與地球上生命的起源的關聯性也一起被討論。N-methyl-pyrrole, anisole與N-methylindole的光分解研究證明了對於非氫化雜環分子其N-CH<sub>3</sub>/O-CH<sub>3</sub>  $\pi\sigma^*$  電子激發態的存在。7-azaindole, 2-aminopyridine與8-Hydroxyquinoline的研究則提供了DNA典型分子其激發態光物理化學的新觀念。

## Abstract

The photodissociation dynamics of aromatics and biomolecules have been investigated by multimass ion imaging technique. The photoisomerization and photodissociation mechanisms of aniline, 4-methylpyridine and phenol were studied. Various dissociation channels including the ground state dissociation with or without exit barrier and excited state dissociation along with N-H/O-H bond distance were observed. The “seven membered ring isomerization” of these aromatic molecules was discussed and compared with toluene. These series of studies established the basic understanding of aromatic molecules under UV irradiation. The suggestion of the deactivation from the optical bright state ( $\pi\pi^*$  state) to the dark state (repulsive  $\pi\sigma^*$  state) through conical intersection has been made to explain the ultrafast decay pathway to dissipate the absorbed UV photon energy of aromatic and biomolecules. The results are the H-atom transfer (proton-electron concerted transfer) on the excited state or internal conversion to the ground state. The detail studies of photodissociation dynamics of phenol and 1-naphthol was performed to test the idea in these chemical systems. By extending the research to biomolecules, the chromophores of amino acid tyrosine and tryptophan were studied. The *p*-methylphenol, *p*-ethylphenol, phenylethylamine and *p*-(2-aminoethyl)phenol reveal the affects of “floppy” side chain and different functional groups (e.g., amino and hydroxyl groups) on the photodissociation dynamics of these chromophores. Likewise, the studies of indole, 3-methyl-indole, tryptoamine and tryptophan are also the way to go deep into the photochemistry issue of amino acid gradually. The photodissociation dynamics of L-tryptophan in a molecular beam and its relevance to the origin of life on earth will be briefly discussed. The photodissociation of N-methyl-pyrrole, anisole and N-methylindole is the another illustration of the non-hydrate heteroaromatic molecules with N-CH<sub>3</sub>/O-CH<sub>3</sub>  $\pi\sigma^*$  state. 7-azaindole, 2-aminopyridine and 8-Hydroxyquinoline were studied to clarify the repulsive N-H/O-H  $\pi\sigma^*$  state which opens up a new aspect to describe the excited-state photophysics of DNA model compounds.

## Table of Contents

Abstract

Acknowledgements

1. Introduction.....	1
References.....	5
2. Experimental techniques and methodology.....	7
I. Overview.....	7
II. Vacuum chamber, molecular beam, and laser beams.....	10
III. Mass spectrometer.....	15
IV. Methodology.....	17
A. Ground state dissociation without exit barrier.....	17
B. Ground state dissociation with exit barrier.....	18
C. Repulsive excited state dissociation.....	19
References.....	22
3. The photodissociation and photoisomerization of aniline and 4-methyl pyridine...23	
Abstract.....	23
Introduction.....	23
Experimental.....	27
Results.....	27
I. Aniline.....	27
II. 4-Methylpyridine.....	32
Discussions.....	35
I. Dissociation and isomerization mechanisms.....	35
A. 4-Methylpyridine.....	35
B. Aniline.....	37
II. Potential energy surface.....	39
III. Comparison to photodissociation of toluene.....	42
References.....	43
4. The photodissociation of phenol.....	46
Abstract.....	46

Introduction.....	46
Experimental.....	47
Results.....	48
A. Photofragments and translational energy distributions at 193 nm.....	48
B. Photofragments and translational energy distributions at 248 nm.....	51
Discussions.....	52
A. Dissociation channels.....	52
B. Potential surface and reaction pathway.....	54
Conclusions.....	58
References.....	58
5. The experimental evidence of $\pi\sigma^*$ repulsive state in phenol and 1-naphthol.....	60
Abstract.....	60
Introduction.....	60
Experimental.....	63
Results.....	63
I. The photodissociation of phenol at 248 nm and 193 nm.....	63
A. Photofragments and translational energy distribution at 248 nm.....	63
B. Photofragments and translational energy distribution at 193 nm.....	65
C. Discussions.....	66
II. The photodissociation of 1-naphthol at 248 nm and 193 nm.....	67
A. Photofragments and translational energy distribution at 193 nm.....	67
B. Photofragments and translational energy distribution at 248 nm.....	69
C. Discussions.....	70
III. Conclusions.....	72
IV. References.....	72
6. The photodissociation of <i>p</i> -methylphenol, <i>p</i> -ethylphenol, phenylethylamine and <i>p</i> -(2 aminoethyl)phenol, chromophores of the amino acid tyrosine.....	75
Abstract.....	75
Introduction.....	75
Experimental.....	76
Computational.....	77
Results.....	77
A. <i>p</i> -Methylphenol.....	77

B. <i>p</i> -Ethylphenol.....	80
C. phenylethylamine.....	82
D. <i>p</i> -(2-Aminoethyl)phenol.....	84
Discussions.....	87
References.....	89
7. The photodissociation of indole, 3-methyl-indole, tryptamine and tryptophan....	90
Abstract.....	90
Introduction.....	90
Experimental.....	91
Results.....	92
I. The photodissociation of indole at 248 nm and 193 nm.....	92
II. The photodissociation of 3-methylindole at 248 nm and 193 nm.....	94
III. The photodissociation of tryptamine at 248 nm and 193 nm.....	95
IV. The photodissociation of tryptophan at 248 nm and 193 nm.....	96
Discussions.....	96
References.....	98
8. The relevance of tryptophan photodissociation in a molecular beam and the origin of life on earth.....	100
Abstract.....	100
Introduction.....	100
Experimental.....	101
Results and discussions.....	102
References.....	105
9. The role of $\pi \sigma^*$ repulsive states in the non-hydride heteroaromatic molecules---N-methyl pyrrole, anisole and N-methyl indole.....	107
Abstract.....	107
Introduction.....	107
Experimental.....	109
Results and discussions.....	109
I. Anisole.....	109
II. N-methylpyrrole.....	112
III. N-methylindole.....	114
References.....	116
10. The photodissociation of DNA base model -7-azaindole, 2-aminopyridine and 8-Hydroxyquinoline.....	119
Abstract.....	119
Introduction.....	119

Experimental.....	123
Results.....	123
I. Photodissociation of 7-azaindole at 248 nm and 193 nm.....	123
A. Photofragments and translational energy distribution at 193 nm.....	123
II. Photodissociation of 2-aminopyridine at 248 nm and 193 nm.....	124
A. Photofragments and translational energy distribution at 248 nm.....	124
B. Photofragments and translational energy distribution at 193 nm.....	125
III. The photodissociation of 8-hydroxyquinoline at 248 nm and 193 nm.....	126
A. Photofragments and translational energy distribution at 248 nm.....	127
B. Photofragments and translational energy distribution at 193 nm.....	128
Discussions.....	129
Conclusions.....	131
References.....	131

Curriculum vitae



## Chapter 1. Introduction

The chemical dynamics and molecular spectroscopy of isolate molecules have been extensively investigated with the techniques of molecular beam and laser light source. The detail understanding of structures, dynamics and functions has already being a tremendous achievement in the field of physical chemistry. The attraction of new techniques applied to the molecules reveals the new horizon for human kind to pursuit the quest of changing world. Historically, the studies of diatomic and triatomic molecules were the outset of discovery and the beginning of knowledge of quantum mechanics of polyatomic species. During the past decays the maturation of laser and molecular beam techniques combined with the ab initio calculation have proved that the achievements can be far beyond the imagination of applied chemistry. Naturally, the treatment of even more complicated species will be the next step. The photochemistry and photophysics of bio-relevant molecules has been studied with various kinds of aspects, but mainly in the condensed phase. The complicated interaction between solvent and solute molecules raises the difficulty to account for the experimental data in a simple manner. Definitely, the condensed phase is the main “playground” of biomolecules. However, the simplification of the studies of biomolecules in the gas phase has a chance to give a clue to compare with theoretical calculation in an isolated condition. It brings the wave of studying biomolecules in the molecular beam and becomes one of the hot topics in physical chemistry nowadays.

Among the vigorous studies, a new paradigm of non-radiative decay in aromatic molecules which had been proposed by Sobolewski and Domcke<sup>1</sup> attracted most of the interest. The paradigm was from the results of the ab initio calculation of the excited state potential of pyrrole, phenol and indole. They suggested the deactivation from the optical bright state ( $\pi \pi^*$  state) to the dark state (repulsive  $\pi \sigma^*$  state) through conical intersection to account for the ultrafast decay pathway to dissipate the absorbed UV photon energy of aromatic and biomolecules. Moreover, the DNA base, adenine, had also been suggested to intrinsically photo-stabilized in a similar manner. The new mechanism raised countless studies in this topic. From February 2002 to June 2008, it has been cited by 217 papers (from the database of ISI Web of Knowledge), as shown in table 1.

Journal	Science	JACS	JCP	JPC A & B	CPL	CPC	PCCP	Others
Numbers of paper	5	17	44	41	13	8	33	56



Table 1. The citation number of the Sobolewski and Domcke' PCCP paper up to June 2008 (from the database of ISI Web of Knowledge)

i.e. JACS: Journal of the American Chemical Society

JCP: Journal of Chemical Physics

JPC A. & B : Journal of Physical Chemistry A and B

CPL: Chemical Physics Letters

CPC: CHEMPHYSCHEM

PCCP: Physical Chemistry Chemical Physics

One of the topics which had been discussed extensively is the dynamics of phenol-ammonia cluster. It has been a benchmark example of the excited state proton transfer (ESPT)<sup>2</sup> in the gas phase. Compare to the proton (H<sup>+</sup>) transfer, the new H-atom detachment (proton-electron concerted transfer) mechanism which was supported by experimental<sup>3</sup> and theoretical<sup>1,4</sup> studies recently can be considered as a revolutionary in the idea of "photo-acidity" in various chemical systems. Similar arguments had also been arisen in the 1-naphthol-ammonia cluster case. The detail studies of photodissociation dynamics of phenol and 1-naphthol performed by our group was described in the chapter 5.

Phenol and indole molecules are the touchstone molecules of the  $\pi\sigma^*$  state along with O-H/N-H bond. Furthermore, they are also the chromophores of amino acid tyrosine and tryptophan. The step-by-step studies of *p*-methylphenol, *p*-ethylphenol, phenylethylamine and *p*-(2 aminoethyl)phenol reveal the affects of "floppy" side chain and different functional groups (e.g., amino group) of the chromophore, as discussed in chapter 6. Likewise, the studies of 3-methyl-indole, tryptamine and tryptophan are also the way to go deep into the photochemistry issue of amino acid gradually. The details will be presented in chapter 7.

The origin of life on earth is a ceaseless question to curious mankind who want to trace where they come from, just like the homesickness of foreigners. The big question happened billion years ago left a clue to trace---the homochirality of amino acids. The amino acids in the human body are only the L-form amino acids, which is the most significant event that can be pursued. There are various scenarios to explain the homochirality, including <i> the parity violation in the weak interaction; <ii> asymmetric adsorption on chiral surfaces; <iii> spontaneous resolution; <iv> asymmetric photodissociation. The mostly probable scenario is the asymmetric photodissociation because of the circular dichroism (CD) spectra of amino acids. For

instance, the CD spectra of L-tryptophan have a reverse sign in  $\sim 213$  nm and  $\sim 193$  nm region. The photodissociation dynamics of L-tryptophan at these two wavelengths in a molecular beam and its relevance to the origin of life on earth will be briefly discussed in chapter 8.

By extending the research on N-H/O-H  $\pi\sigma^*$  state, another illustration is the non-hydrate heteroaromatic molecules with N-CH<sub>3</sub>/O-CH<sub>3</sub>. The photodissociation of N-methyl-pyrrole, anisole and N-methylindole at 248 nm and 193 nm has been investigated using the multi-mass technique. Large recoil velocity of methyl radicals is observed which indicates the N-R/O-R  $\pi\sigma^*$  state plays an important role in the UV photochemistry of biomolecules with this functional group. This topic is presented in chapter 9.

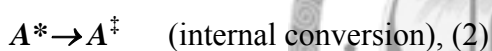
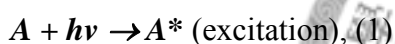
Excited-state double-proton transfer (ESDPT) has been considered as a model mechanism of DNA base pair. It has triggered an enormous effort in various fields of physical chemistry. Here, 7-azaindole, 2-aminopyridine and 8-Hydroxyquinoline were studied and the results were reported in chapter 10. Experimentally, the clarification of the repulsive N-H/O-H  $\pi\sigma^*$  state opens up a new aspect to describe the excited-state photophysics of DNA model compounds.

Moreover, the photodissociation studies of aniline and 4-methylpyridine in chapter 3 have discovered a new phenomena, so-called “seven-membered ring isomerization”, in the photoisomerization of nitrogen atom contained aromatic molecules. In chapter 4, another important aromatic molecule, phenol, has also been studied. The major dissociation channels at 193 nm include cleavage of the OH bond, elimination of CO, and elimination of H<sub>2</sub>O. Only the former two channels were observed at 248 nm. The comparison between experimentally measured photofragment translational energy distribution and theoretically ab initio calculated potential profile has also been made.

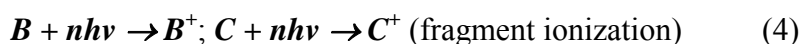
This thesis is not only the reflection of the tendency, the studies of the photodissociation dynamics of biomolecules in the gas phase, but also the new development of molecular beam techniques in the area of photodissociation dynamics. Honored in 1986 with the Nobel Prize, Professor Y. T. Lee developed a so called “General Type” machine, which composed of a molecule/molecule (or molecule/laser) crossed-beam and a rotatable detector with electron bombardment to ionize the neutral species in a ultrahigh vacuum condition ( $\sim 10^{-11}$  torr). The detector is located at an angle from the molecular beam axis and is displaced some distance from the photolysis volume. One can measure the velocity (by measuring time-of-flight profile) and angular (by rotation of detector) distribution of products to elucidate the reaction

mechanism in detail. However, there are some disadvantages. First, the velocities of the photofragments are measured in the laboratory frame; they have to be converted to the center-of-mass frame for data analysis. Second, photofragments are usually ionized by electron impact and detected by the quadrupole mass spectrometer. Fragments ionized by electron impact easily produce daughter fragment ions through the fragment cracking due to the high energy of electrons. If the mass of the daughter ions is the same as that of the primary fragment masses from another dissociation channel, the data analysis will be complicated due to the interference from the daughter ions. Finally, only a single mass at a given angle can be detected each time. It makes the measurement time consuming for large molecules having many product channels in the photodissociation process.

Another challenge of the large molecule photofragment velocity measurements is in the studies of UV photodissociation of polyatomic molecules like alkenes and aromatic molecules. Molecules excited by the UV photons quickly become highly vibrationally excited in the electronic ground state through fast internal conversion, and dissociate on the ground state



Here,  $A^*$  represents molecules in the excited state, and  $A^\ddagger$  represents highly vibrationally excited molecules in the electronic ground state. The dissociation rates of these molecules may be very slow and the lifetimes of  $A^\ddagger$  are in the microsecond region. In the conventional ion-imaging techniques and time-of flight mass spectrometry, the fragment detection is through the multiphoton ionization or VUV photoionization by the same laser pulse or using a second laser pulse



The delay time between the pump and the probe laser pulses is usually very short in these experiments. The delay time is less than 5 ns when the pump and the probe laser pulses are the same, and the delay time is as long as several hundred nanoseconds when the pump and the probe laser pulses are from two different sources. The short delay time ensures that the fragments flying with different velocities are equally sampled before they leave the detection region. Since the delay time is much shorter than the lifetime of the excited molecules ( $A^\ddagger$ ), most of these molecules do not dissociate into fragments when the probe laser pulse arrives. As a result, the probe laser can easily cause dissociative ionization of the excited molecules due to their

large internal energy



The photofragment translational energy distributions of the dissociative ionization [reaction (5)] are different from those of the products obtained from the dissociation processes [reaction (3)]. However, if the masses of fragments **B** and **D** happen to be the same, the images or the broadening of the arrival time of fragments **B**<sup>+</sup> and **D**<sup>+</sup> will be overlapped. These two reactions can not be distinguished from the images obtained by the conventional ion-imaging techniques or from the broadening of the features in the time-of-flight mass spectrum. The probability that **B** and **D** have the same value of mass is high for large molecules having many dissociation channels.

A new idea to measure the product translational spectra was proposed by Professor Y. T. Lee and the instrument was constructed in Professor C. K. Ni's laboratory<sup>5</sup>. The goal was to overcome the difficulties of the other available techniques mentioned previously. Basically, a mass spectrometer with a long entrance slit and a position sensitive detector are combined with a pulsed VUV laser to detect the translational spectroscopy of many different photofragments simultaneously. The translational energy spectroscopy is measured in the center-of-mass frame, based on the displacement from the origin of the center-of-mass frame, thus eliminating the effort of conversion between the laboratory frame and the center-of-mass frame. Fragments are ionized by a VUV laser pulse with the photon energy above the ionization threshold. The VUV photon energy is chosen such that the fragment's dissociation after ionization is minimized. Long delay time between the pump and the probe laser pulses (>10 μs) is used in order to distinguish the reactions between dissociative ionization and neutral molecule dissociation. Photofragment translational spectroscopy of many different fragments from large molecules can also be measured simultaneously, and the data analysis is straightforward.

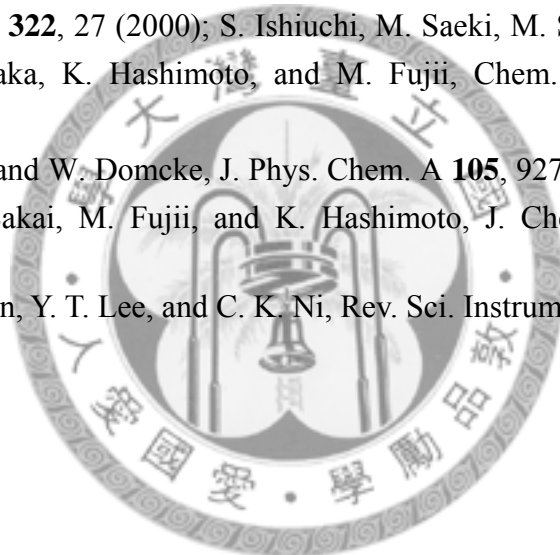
All of the experimental observations for the present study were taken using the multimass ion imaging technique in the Chi-Kung Ni' laboratory of the Institute of Atomic and Molecular Sciences. The multi-mass imaging technique is able to measure the complex dynamics of photofragmentation in the aromatic molecules and biomolecules.

## References

---

<sup>1</sup> A. L. Sobolewski, W. Domcke, C. Dedonder-Lardeux, and C. Jouvet, Phys. Chem.

- 
- Chem. Phys. **4**, 1093 (2002).
- <sup>2</sup> D. Solgadi, C. Jouvét, and A. Tramer, *J. Phys. Chem.* **92**, 3313 (1988); C. Jouvét, C. Dedonder-Lardeux, M. Richard-Viard, D. Solgadi, and A. Tramer, *J. Phys. Chem.* **94**, 5041 (1990); J. Steadman and J. A. Syage, *J. Phys. Chem.* **92**, 4630 (1990); J. A. Syage and J. Steadman, *J. Chem. Phys.* **95**, 2497 (1991); J. Steadman and J. A. Syage, *J. Am. Chem. Soc.* **113**, 6786 (1991); J. A. Syage and J. Steadman, *J. Phys. Chem.* **96**, 9606 (1992); J. A. Syage, *Chem. Phys. Lett.* **202**, 227 (1993); M. F. Hineman, D. F. Kelley, and E. R. Bernstein, *J. Chem. Phys.* **99**, 4533 (1993).
- <sup>3</sup> C. Jacoby, P. Hering, M. Schmitt, W. Roth, and K. Kleinermanns, *Chem. Phys.* **23**, 239 (1998); G. Pino, G. Gre'goire, C. Dedonder-Lardeux, C. Jouvét, S. Martrenchard, and D. Solgadi, *J. Chem. Phys.* **111**, 10747 (1999); G. Pino, G. Gre'goire, C. Dedonder-Lardeux, C. Jouvét, S. Martrenchard, and D. Solgadi, *Phys. Chem. Chem. Phys.* **2**, 893 (2000); S. Ishiuchi, M. Saeki, M. Sakai, and M. Fujii, *Chem. Phys. Lett.* **322**, 27 (2000); S. Ishiuchi, M. Saeki, M. Sakai, K. Daigoku, T. Ueda, T. Yamanaka, K. Hashimoto, and M. Fujii, *Chem. Phys. Lett.* **347**, 87 (2001).
- <sup>4</sup> A. L. Sobolewski and W. Domcke, *J. Phys. Chem. A* **105**, 9275 (2001); K. Daigoku, S. Ishiuchi, M. Sakai, M. Fujii, and K. Hashimoto, *J. Chem. Phys.* **119**, 5149 (2003).
- <sup>5</sup> S. T. Tsai, C. K. Lin, Y. T. Lee, and C. K. Ni, *Rev. Sci. Instrum.* **72**, 1963(2001)



## Chapter 2. Experimental techniques and methodology

### I. Overview

Detail description of the multi-mass ion imaging technique was given in detail elsewhere.<sup>1,2,3,4</sup> Brief description is given in this chapter. This apparatus consists of a molecular beam, a photolysis laser beam, a VUV probe laser beam, a mass spectrometer, and a two-dimensional ion detector. The schematic diagram is shown in Fig. 1. The molecular beam, photolysis laser beam, and VUV laser beam are perpendicular to each other. However, the crossing points of the photolysis laser beam and the VUV laser beam with the molecular beam are not the same. The crossing point of the photolysis laser beam with the molecular beam is several centimeters upstream with respect to the crossing point of the VUV laser with the molecular beam. Molecules in the molecular beam are photodissociated by a photolysis laser pulse. Due to the recoil velocity of dissociation products and center-of-mass velocity, the fragments are distributed on an expanding sphere on their flight to the ionization region, and are then ionized by a VUV laser pulse. The distance and time delay between the VUV laser pulse and the photolysis laser pulse are set such that the time delay matches with the arrival of undissociated molecules. This time delay ensures that the VUV laser beam passes through the center of the fragment sphere and, therefore, the fragment's velocity distribution is measured in the center-of-mass frame. The VUV laser pulse generates a segment of photofragment ions along the laser path through the center of fragment sphere by photoionization. There could be many fragment ions of different masses within this segment according to the photodissociation mechanisms of parent molecules. Each fragment has its own intensity distribution along the segment. The length of the segment is proportional to the fragment recoil velocity in the center-of-mass frame multiplied by the delay time.

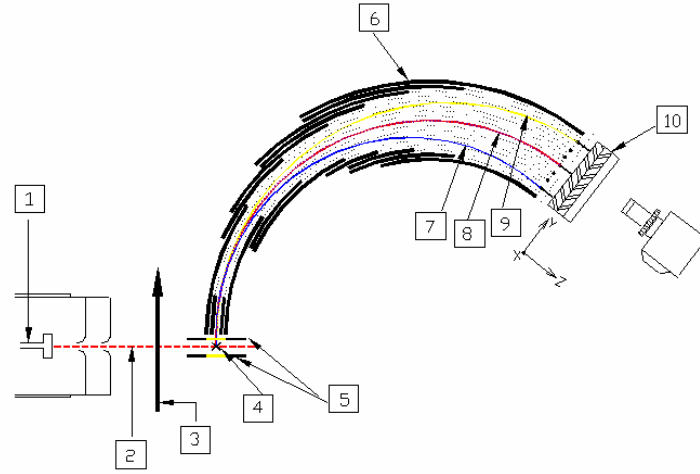


Fig.1. Schematic diagram of the multimass ion imaging system. (1) Nozzle, (2) molecular beam, (3) photolysis laser beam, (4) VUV laser beam, which was perpendicular to the plane of the paper, (5) ion extraction plates, (6) energy analyzer (7-9) simulation ion trajectories of  $m/e = 16, 14,$  and  $12,$  respectively, and (10) two-dimensional detector, where the  $Y$  axis is the mass axis and the  $X$  axis (perpendicular to the plane of the paper) is the velocity axis.

After the ions have been generated by the VUV laser pulse, a pulsed electric field is used to extract the ions into a mass spectrometer in order to separate different masses within the ion segment. The entrance of the mass spectrometer has a long slit parallel to the VUV laser beam to accept the ions produced at various positions in the line of VUV laser irradiation. The mass spectrometer basically is a radial cylindrical energy analyzer. In this instrument, the pulsed electric field used to extract ions is very short so that the electric field is turned off before any ions leave the extraction region and enter into the energy analyzer. The momentum,  $\mathbf{P}$ , of the ions obtained from the pulsed field can be expressed by the following equations:

$$P = \int F dt = \int ma dt = \int m(qE/m) dt = \int qE dt. \quad (1)$$

Here,  $m$  is the mass of the ion,  $a$  is the acceleration of the ion by the electric field  $E$  in the extraction region,  $q$  is the charge of the ion, and  $F$  is the force. The range of time  $t$  in the integral is equal to the duration which the ion is accelerated by the electric field. In conventional time-of-flight instrument, the electric field is turned on all the time when ions travel through the extraction region. Because different masses require different time

to travel through the extraction region, the range of time  $t$  in the integral of Eq. (1) is different for different masses. Thus, the momentum obtained from the electric field is different between different masses, though the energy is the same. However, in our instrument, the pulsed electric field is turned off before any ions leave the extraction region, thus the range of time in the integral of Eq. (1) is the same for all masses. Therefore, all the ions will be accelerated to the same linear momentum along the direction of the field. In other words, the ion's translational energy that is obtained from the pulsed electric field is proportional to the reciprocal of the fragment's mass. Different fragment ions entering the radial cylindrical energy analyzer can be separated according to the difference of energies obtained from the pulsed electric field.

Since the VUV laser beam passes through the center of the fragment sphere, fragments ionized by the VUV laser have the recoil velocity in the direction of the VUV laser beam axis. These recoil velocities would not be affected by the pulsed field or the energy analyzer. During the flight through the energy analyzer, the length of the fragment ion segment generated by the VUV laser keeps expanding according to the fragment recoil velocity. Meanwhile, ions of different masses start separating from each other in the energy analyzer. At the exit port of the energy analyzer, a 7 cm x 8 cm two-dimensional ion detector is used to detect the ion position and intensity distributions. In this two dimensional detector, one direction is the recoil velocity axis ( $X$  axis, as shown in Fig. 1) and the other is the mass axis ( $Y$  axis, as shown in Fig. 1). The recoil velocity distributions in the center-of-mass frame of many different fragments can be obtained simultaneously from the position and intensity distributions of the image.

The change in distance between the crossing points of the photolysis laser and VUV laser with a molecular beam has to match with the delay time between these two laser pulses, according to the velocity of the molecular beam to ensure the ionization laser passes through the center-of-mass of the products. This adjustment also changes the length of fragment ion segment in the image. The relation between the length of the ion image and the position of the photolysis laser is shown in Fig. 2. If the molecules are not dissociated after the absorption of the photolysis photons, those molecules with a large internal energy will stay within the molecular beam. They fly with the same velocity to the ionization region and are ionized by the VUV laser, resulting in dissociative ionization. The ion image from the dissociative ionization is very much different from the fragment image due to the dissociation products of neutral molecules. The image from dissociative ionization is a 2D projection of the photofragment ion's 3D-recoil velocity distribution. It is very similar to the image from the conventional ion imaging techniques



and is a disk-like image. With the VUV laser fixed in position, only the intensity of the disk-like image changes with the delay time between the two laser pulses, but the size of the disk-like image would not change with the delay time. Therefore, the ion image resulted from the dissociative ionization can be distinguished easily from the image resulted from the dissociation products of the neutral molecules by the shape of the image.

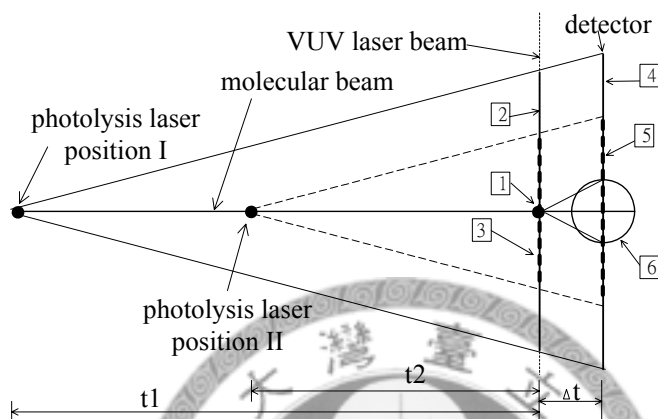


Fig. 2. Relationship between the lengths of the line shape images, resulting from different photolysis laser positions and the disk-like image from the dissociative ionization. [1] represents the crossing point for the molecular beam and the VUV laser beam, where dissociative ionization occurs. [2] and [3] represent the lengths of the fragment ion segment created by the VUV laser photoionization from two different photolysis laser positions. [4] and [5] represent the lengths of the fragment ion image on the detector from two different photolysis laser positions. [6] represents the disk-like image.  $t_1$  and  $t_2$  give the two different delay times between the photolysis laser pulse and the VUV laser pulse.  $\Delta t$  is the flight time in the mass spectrometer.

## II. Vacuum chamber, molecular beam, and laser beams

The vacuum chamber consists of a source chamber, a differential pumping chamber, and a main chamber. The molecular beam is formed by the supersonic expansion of gas through a pulsed nozzle. It is then collimated by two skimmers, and enters the main chamber. The molecular beam first interacts with the photolysis laser beam in the main chamber, and then with the VUV laser beam. The VUV laser beam is generated by frequency tripling or four wave mixing of UV/ visible (VIS) laser beams in rare gas. After the generation of VUV radiation, the coaxial UV/VIS and VUV laser beams are sent to a homemade vacuum monochromator to separate the VUV laser beam from the

UV/VIS laser beam. The VUV laser beam alone is sent to the ionization region. A concave grating with 1200 1/mm and radius of 114 cm is used in the vacuum monochromator. The distances are set such that the focal point of UV/VIS laser beams is 120 cm away from the grating. The concave grating refocuses the expanding VUV radiation onto the molecular beam, which is 82 cm away from the grating. The grating is set near the normal incidence ( $18^\circ$ ) and the first order of the VUV radiation from the grating is used, as shown in Fig. 3. The crossing position of the molecular beam with a VUV laser beam is fixed. However, changing the position of the photolysis laser beam can change the crossing position of the photolysis laser beam with the molecular beam. In general, the distance between these two crossing points is set to be long for the detection of fragments with a small recoil velocity, whereas it is set to be short for the detection of fragments with a large recoil velocity.

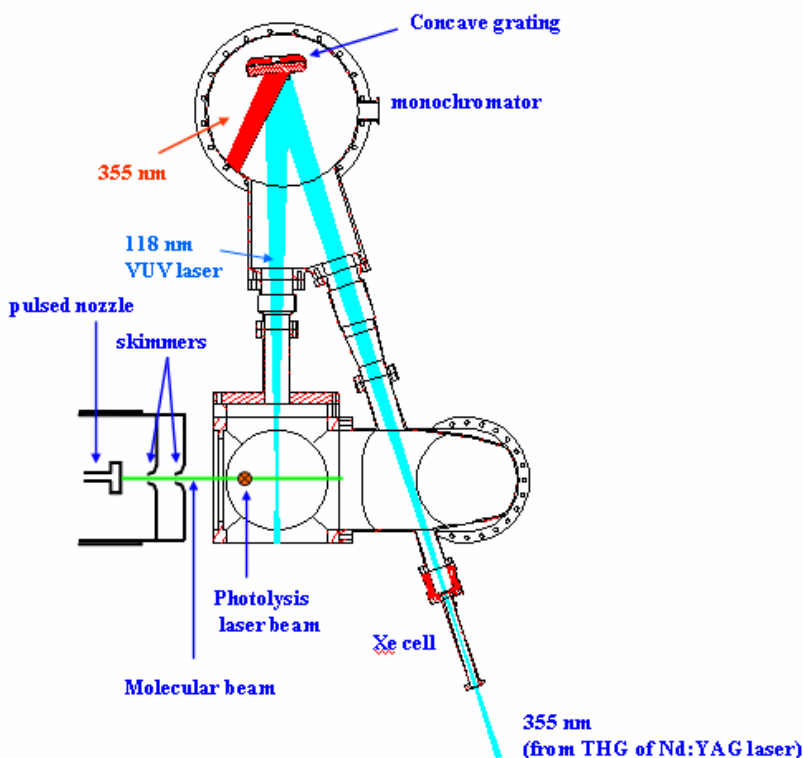


Fig. 3. Schematic diagram of VUV laser generation and monochromator setup. Focus the 355 nm laser by a UV lens ( $f = 20$  cm) into a Xe cell ( $\sim 10$  torr) to generate 118 nm VUV laser. Then, separate the 355 nm and 118 nm by a concave grating and refocus the 118 nm VUV laser onto the molecular beam.

In general, the generation of molecular beam is generated by bubbling carrier gas

(rare gases, including He, Ne, Ar, Kr) through a glass sample cell. We used this method for the compounds in liquid phase under normal condition (1 atm., room temperature). If the samples are solids, a metal sample cell was used. It is maintained at high temperature in order to have sufficient vapor pressure from the solid phase. Both sample cells were placed outside the vacuum chamber and the mixture of sample vapor and rare gas was transferred through a heated sample line into a pulsed nozzle in the vacuum chamber. The mixture is then expanded through a pulsed nozzle to form a molecular beam, as shown in Fig. 4(a). The temperature was gradually increased from the sample cell to the nozzle in order to prevent condense of sample in the sample line, moreover, to reduce the formation of clusters in the molecular beam.

Some biomolecules have very low vapor pressure. Some functional groups of these molecules are reactive to the material of sample line and nozzle. For example, compounds with amino group will react with the O-ring and the metal of sample transfer line. We found that the O-ring got damaged and the rust happened on the metal surface. To reduce these problems, we design an oven attached onto the front of the nozzle to minimize the contact time of the sample gas with the reactive components, as shown in Fig. 4(b). A long plunger has been made for the purpose to control the exit port of the oven. The pulsed nozzle (General Valve, Series 9) was modified so that the plunger can extend to the oven. The oven is mainly made by stainless steel. There is a glass container inside the oven and polymer coating on the most of the metallic surface, including the plunger and oven. But there is still some metallic surface exposures to the sample gas.

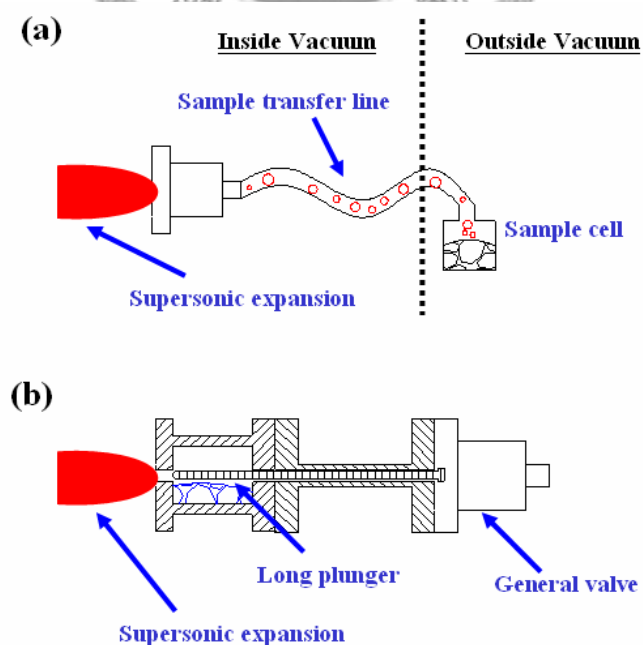


Fig. 4. Schematic diagram of different nozzle setup. (a) Typical setup for generation of molecular beam. (b) Special design for putting the sample in a oven attached to the general valve.

The decomposition of compounds still occurred. For example, tryptophan and tryptoamine thermally decomposed with  $\text{CO}_2$  and  $\text{CH}_2\text{NH}_2$  loss respectively, as shown in Fig.5. After heating up the oven, the black and sticky substance, like bitumen, was found and bound on the metallic surface. In order to disassemble the oven, the menthol was used to dissolve the bitumen. The bitumen was only found on the metal surface. The glass container and the surface coated with polymer had no such substance. Moreover, the bitumen stuck on the exposed metal surface due to the ablation of coated polymer after heating.

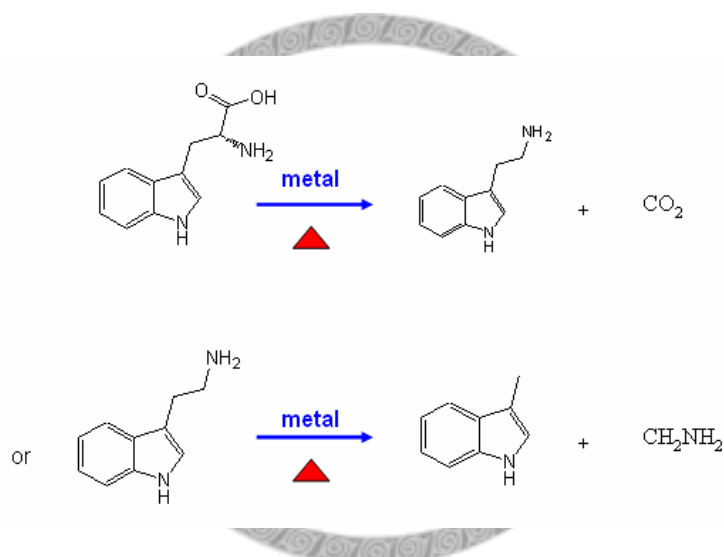


Fig 5. The thermal decomposition of tryptophan and tryptoamine in a metal oven.

A suspect is raised naturally: according to the above observation the metal surface might play a catalytic role when heating up these samples. Additionally, T. Hashimoto et al<sup>5</sup> suggested the construction of the oven with plastic polymer. They can generate an amino acid, L-phenylalaine in a molecular beam and detected the parent molecules by resonance enhanced multiphoton ionization spectroscopy. Thus, a non-metallic oven might be the solution.

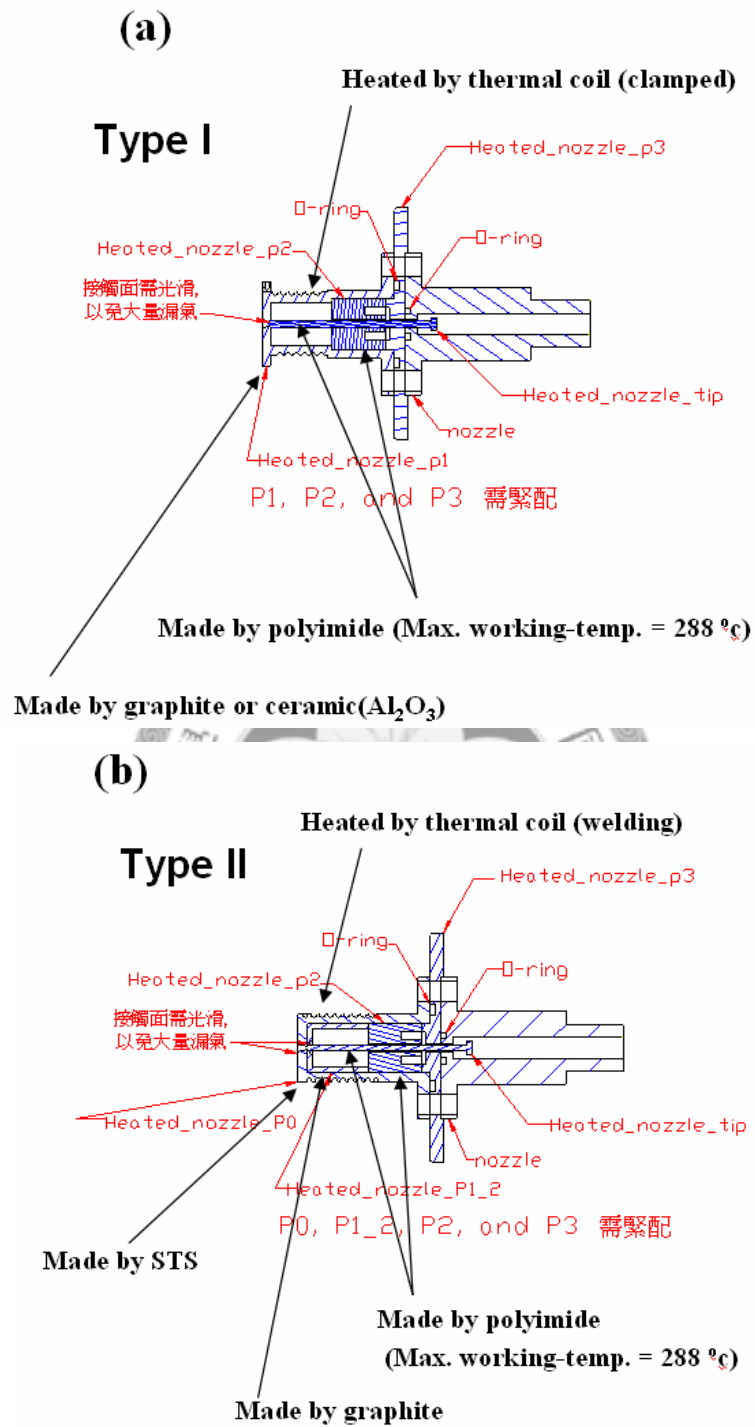


Fig 6. Schematic diagram of non-metallic ovens (type I and type II) attached to the nozzle.

Fig. 6 shows two types of non-metallic ovens which we have constructed. Type I

was made by graphite or ceramic. The high-density graphite that we need is not dense enough and it causes a leak. It needs to use with caution because the oven made by the machine-able ceramics is fragile. In addition, the heating coil can only be clamped on the oven; hence the heating efficiency is not good. Type II was made by stainless steel and a graphite cup was inserted inside. The oven is mechanically strong outside and chemically inert inside. The heating efficiency of Type II oven is much better because the welding of the heating coil on the oven can be made. The front surfaces of the pulsed valve in both types are covered by a polymer sheet (Heated\_nozzle\_p2, made by polyimide) and an extended polymer plunger (Heated\_nozzle\_tip, made by polyimide) was used. The performance of the non-metallic oven in the experiment of DNA base, adenine is shown in Fig. 7. Only the parent mass was detected when the non-metallic oven at 110°C was used. On the other hand, the seriously thermal decomposition occurred for the metallic oven when the temperature was just increased to  $\sim 100^\circ\text{C}$ . It shows that a molecular beam containing biomolecules can be produced from the non-metallic oven in front of the nozzle. In this thesis, most of the biomolecules were studied using this non-metallic oven.

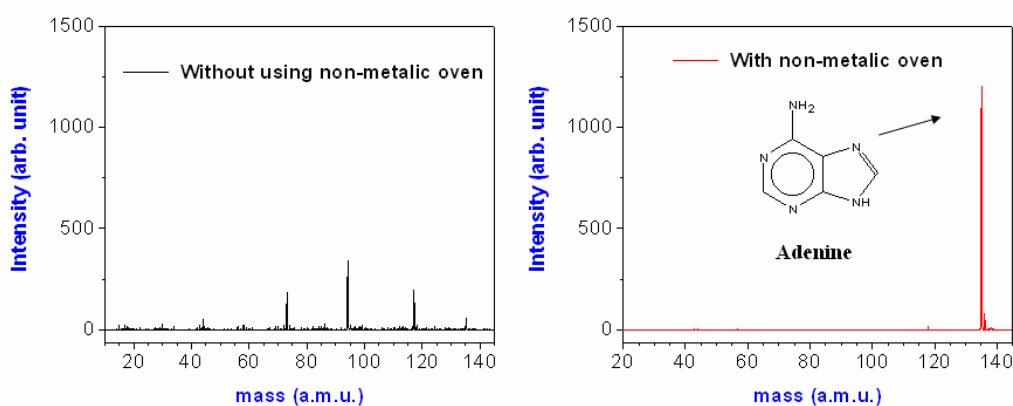


Fig 7. The time-of-flight mass spectrum of DNA base, adenine was proved by 118 nm laser. It shows that the validation of the non-metallic oven to generate a bio-molecular beam.

### III. Mass spectrometer

One of the key components in the system is the mass spectrometer. Fragments are ionized by a VUV laser pulse between a pair of plane parallel-plate electrodes (6 x 14 cm). One of the plane electrodes has a slit of 1 x 10 cm, which is covered by a metal mesh. The slit is parallel to the VUV laser beam and is the entrance of the mass spectrometer. Ions are accelerated by a pulsed electric field present between the plane

parallel-plate electrodes, and pass through the slit before they enter the mass spectrometer.

The mass spectrometer is a homemade radial cylindrical energy analyzer. A radial electric field is produced by an electrical potential applied to the inner and outer concentric cylindrical electrodes. The radii of the outer and inner electrodes are 26 and 18 cm, respectively. In order to reduce the fringing field effect, fifteen U-shaped concentric cylindrical electrodes, which are mounted on two grooved parallel ceramic plates, are placed in equal distance between the inner and outer cylindrical electrodes, as shown in Fig. 7. The distance between these two parallel ceramic plates is 12 cm. The voltages of these concentric cylindrical electrodes  $V_i$  with a radius  $R_i$  are related to the central concentric cylindrical electrode voltage  $V_0$  with a radius  $R_0$  by the following equation:

$$V_i = V_0 + 2V_0 \ln(R_i/R_0).$$

The cylindrical electrodes subtend an angle of  $127.3^\circ$  to obtain first order focusing. However, this focusing condition is valid only for the incident ion kinetic energy related to the central cylindrical electrode voltage  $V_0$  by  $E = qV_0$ , where  $E$  is the ion kinetic energy, in which the velocity is in the plane perpendicular to the VUV laser beam.

At the exit port of the energy analyzer, nine tungsten wires of 30 mm diameter are spot welded on every other concentric cylindrical electrode, as shown in Fig. 8. These wires effectively reduce the fringing field and also provide high ion transmission efficiency. An 8x 10 cm metal mesh, having a voltage equal to the central cylindrical electrode voltage, is placed between the analyzer exit port and the two dimensional detector to reduce further the fringing field effect. Ions from the exit port of the energy analyzer pass through this mesh and fly to the detector. The detector is an assembly of z-stack microchannel plates and a phosphor screen. Signals are recorded by a charge-coupled device (CCD) video camera, and are accumulated in the computer.

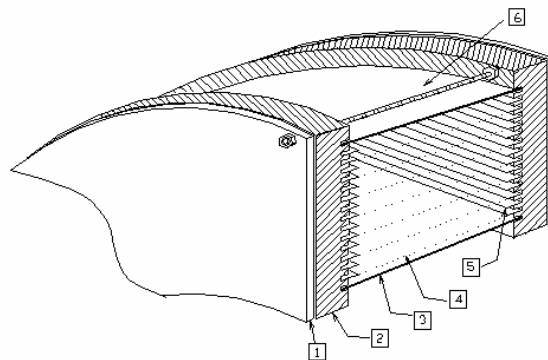


Fig. 8. Exit port of the energy analyzer: (1) stainless steel plates to support the ceramic plates, (2) grooved ceramic plates to support the concentric cylindrical electrodes, (3) inner cylindrical electrodes, (4) 30 mm diameter tungsten wire, (5) a total of 15 concentric cylindrical electrodes separated equally between the inner and outer cylindrical electrodes, and (6) Outer cylindrical electrode

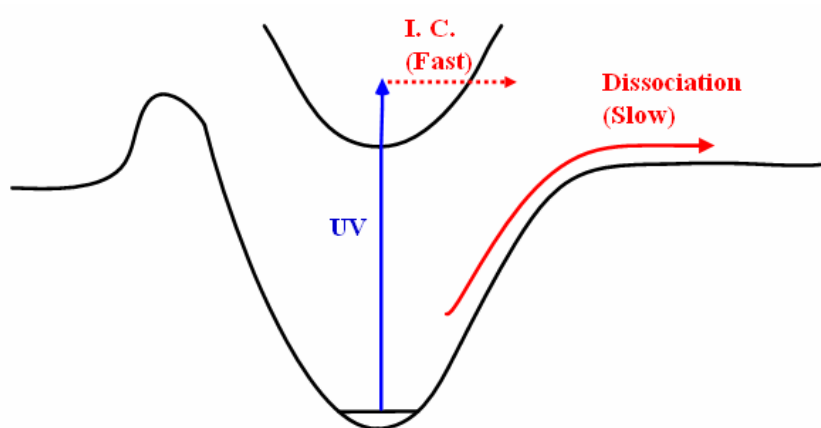
## IV. Methodology

After decades of development, the photofragment translational energy measurement has been recognized as a powerful method to investigate the reaction mechanism. Mutual interaction between atoms, which is rationalized in terms of potential energy surface, binds them together as a molecule. The basic idea of this method is to measure the photofragment recoil velocity in order to justify the potential surface that the fragments pass through. In other words, breaking the molecules into pieces and the measurement of the recoil velocity actually is a way to understand the potential energy surface. Brief description of the methodology is given below.

### A. Ground state dissociation without an exit barrier

Internal conversion (IC) of the initially prepared excited state yields a microcanonical ensemble of vibrational states on the ground state potential energy surface (PES). In the absence of a barrier, unimolecular dissociation of a microcanonical ensemble can be treated classically in terms of Liouville's theorem; a system with an equilibrium distribution in one part of phase space evolves with an equilibrium distribution in other parts of phase space, so that all parts of an undivided phase space are in equilibrium. The consequence of this is that energy is randomized with equal probability among all vibrational levels (up to the fixed excitation energy) and all product states have an equal population probability. It means that the intramolecular vibration energy redistribution (IVR) is completed. As a result, the photofragment translational energy distribution is monotonically decreased as the translational energy increase and the most probable translational energy is close to zero, as shown in Fig. 9. and Fig 10.





**Intra-molecular vibration energy redistribution (IVR) completely  
The photofragment translational energy distribution-- "Statistically"**

Fig. 9. Ground state dissociation mechanism without exit barrier.

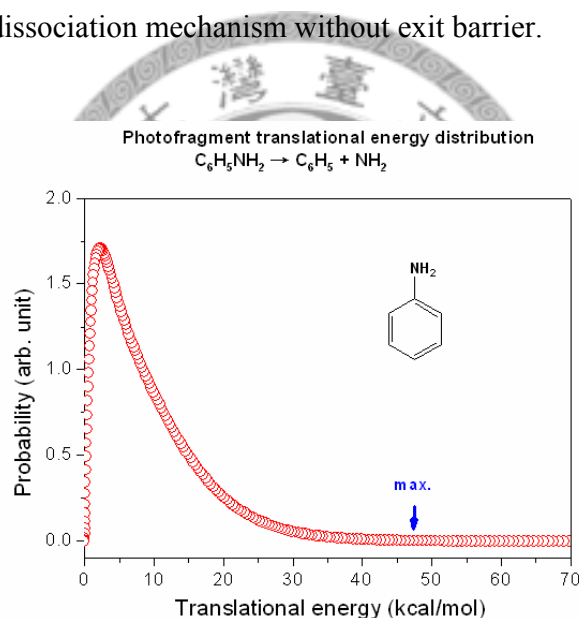


Fig. 10. The photofragment translational energy distribution of  $C_6H_5NH_2 \rightarrow C_6H_5 + NH_2$ .

## B. Ground state dissociation with an exit barrier

The presence of a barrier along the reaction coordinate of the ground state surface forms a dynamical bottleneck, which divides phase space into reactant and product regions.<sup>6</sup> The energy available to products can be divided into two independent reservoirs: statistical and impulsive energy reservoirs. There is the available energy in excess of the barrier, and the other is the barrier height with respect to the exit valley. As

a result, the photofragment translational energy distribution is peak away from zero. The peak position can be very close to the barrier height in the case of late barrier, as shown in Fig. 11 and Fig 12.

### Ground state dissociation over a barrier

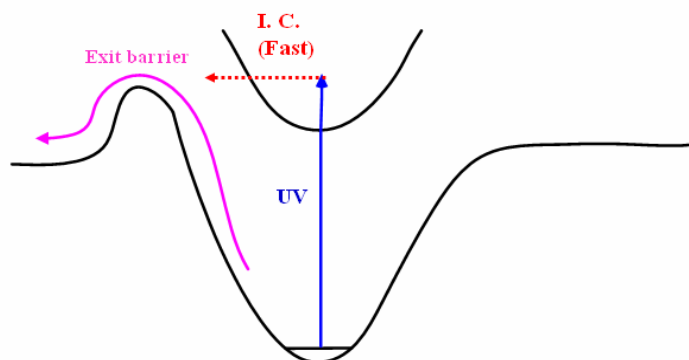


Fig. 11. Ground state dissociation over a barrier in the exit valley.

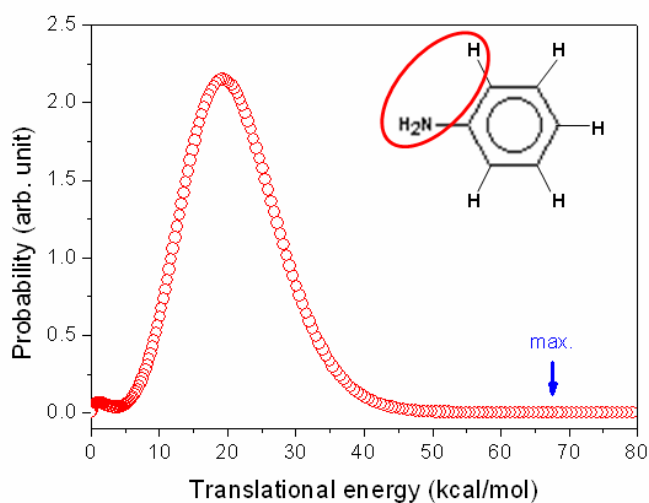
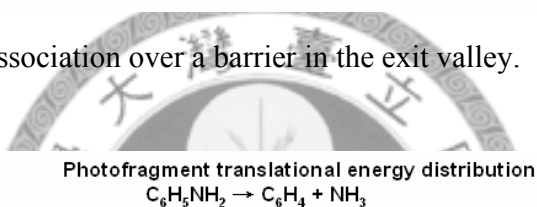


Fig. 12. The photofragment translational energy distribution of  $C_6H_5NH_2 \rightarrow C_6H_4 + NH_3$ .

### C. Repulsive excited state dissociation

Molecules excited by UV photon are promoted to the electronic excited state. Because the transition occurs “instantaneously”, i.e., much faster than the nuclear motion,

the molecule does not change its shape during the transition. In general the molecules on the excited state right after excitation are not in the equilibrium structures. If molecule is on the steep slope of a repulsive excited state, dissociation occurs quickly. Even if the initial excited state is a bound state, molecules could cross over to a repulsive excited state through conical intersection between potential surfaces. This is called “predissociation”, as shown in Fig.13. The peak of photofragment translational energy distribution is far away from zero and the maximum translational energy can reach the maximum available energy. For example, photodissociation of phenol at 248 nm is given in Fig. 14.

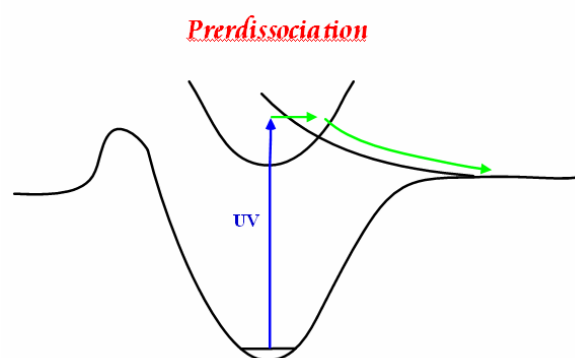


Fig. 13. Predissociation

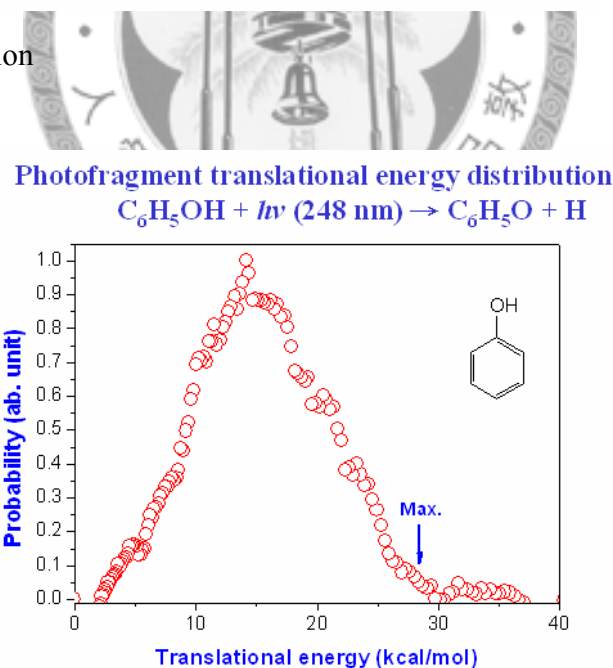


Fig. 14. The photofragment translational energy distribution of  $C_6H_5OH \rightarrow C_6H_5O + H$ .

The correspondent multi-mass ion image of aniline at 193 nm which dissociates in

the ground state with or without barrier has shown in Fig. 15. The photodissociation of aniline ( $m/e = 93$ ) at 193 nm has two channels on the image: one is  $C_6H_5NH_2 \rightarrow C_6H_5$  ( $m/e = 77$ ) +  $NH_2$ , ground state dissociation without barrier; another is  $C_6H_5NH_2 \rightarrow C_6H_4$  ( $m/e = 76$ ) +  $NH_3$ , ground state dissociation with an barrier. The  $m/e = 78$  is the naturally abundant  $C_{13}$  isotopomer of  $C_6H_5$ .

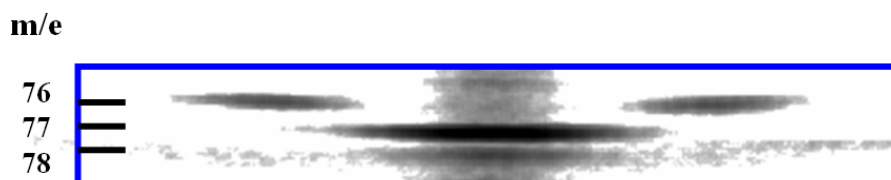


Fig. 15. The multi-mass ion image of aniline at 193 nm. The delay between pump laser (193 nm) and probe laser (118 nm) is 14  $\mu s$ .

The multi-mass image clearly shows that the center-of-mass velocity distribution of different channels simultaneously. The fast recoil velocity of  $m/e = 76$  reveal a “hump shape” image and the slow one shows a line shape image.

The image from predissociation is shown in Fig. 16. The photodissociation of phenol ( $m/e = 94$ ) at 248 nm in different delay time:  $C_6H_5OH \rightarrow C_6H_5O$  ( $m/e = 93$ ) +  $H$ . The line image increases the length and gradually becomes a “hump shape” image due to the fast recoil velocity of photofragment.

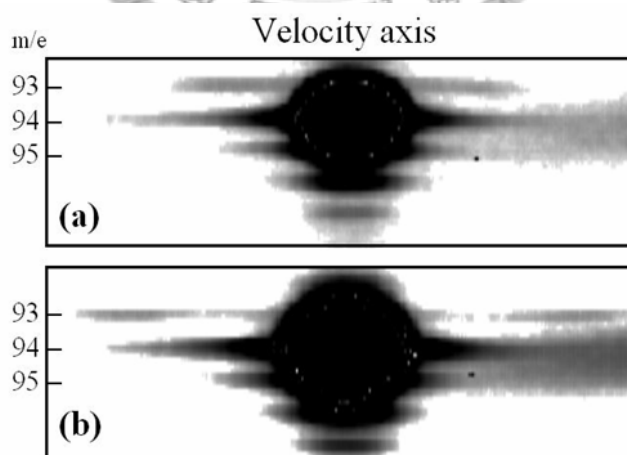


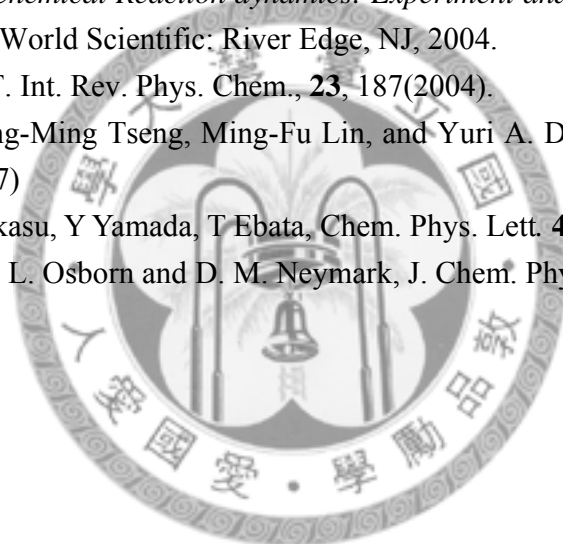
Fig. 16. The multi-mass ion image of phenol at 248 nm. The delay between pump laser (193 nm) and probe laser (118 nm) are (a) 53  $\mu s$  and (b) 95  $\mu s$ .

In summary, we describe the main idea of the multi-mass ion imaging techniques and the experimental setup, including the molecular beam, VUV laser and detection scheme. A brief introduction of the methodology of photofragment translational energy distribution is also given. The following chapters will present the studies of various aromatic molecules and biomolecules separately.

## References

---

- <sup>1</sup> Tsai, S. T.; Lin, C. K.; Lee, Y. T.; Ni, C. K. *Rev. Sci. Instrum.*, **72**, 1963(2001).
- <sup>2</sup> Huang, C. L.; Lee, Y. T.; Ni, C. K. Multimass ion imaging, A new experimental technique and the application in photodissociation of small aromatic molecules. In *Modern Trends in Chemical Reaction dynamics: Experiment and Theory (Part II)*; Liu, K., Yang, X., Eds.; World Scientific: River Edge, NJ, 2004.
- <sup>3</sup> Ni, C. K.; Lee, Y. T. *Int. Rev. Phys. Chem.*, **23**, 187(2004).
- <sup>4</sup> Chi-Kung Ni, Cheng-Ming Tseng, Ming-Fu Lin, and Yuri A. Dyakov, *J. Phys. Chem. B*, **111**, 12631(2007)
- <sup>5</sup> T Hashimoto, Y Takasu, Y Yamada, T Ebata, *Chem. Phys. Lett.* **421**, 227 (2006).
- <sup>6</sup> D. H. Mordaunt, D. L. Osborn and D. M. Neymark, *J. Chem. Phys.*, **108**, 2448(1998)



## Chapter 3. The photodissociation and photoisomerisation of aniline and 4-methyl pyridine

### Abstract

Photoisomerization and photodissociation of aniline and 4-methylpyridine at 193 nm were studied separately using multimass ion imaging techniques. Photofragment translational energy distributions and dissociation rates were measured. Our results demonstrate that more than 23% of the ground electronic state aniline and 10% of 4-methylpyridine produced from the excitation by 193 nm photons after internal conversion isomerize to seven-membered ring isomers, followed by the H atom migration in the seven-membered ring, and then rearomatize to both methylpyridine and aniline prior to dissociation. The significance of this isomerization is that the carbon, nitrogen, and hydrogen atoms belonging to the alkyl or amino groups are involved in the exchange with those atoms in the aromatic ring during the isomerization.

### Introduction

The UV fluorescence quantum yields of most aromatic molecules decrease rapidly with the increase of photon energy.<sup>1,2,3,4,5</sup> For these molecules, the most characteristic monomolecular processes in the condensed phase after excitation to the  $S_1$  state is photoisomerization with formation of the derivatives of fulvenes, benzvalenes, Dewar benzenes, and prismanes, as well as isomerization with a change of the alkyl substitute's position in the aromatic ring.<sup>6, 7, 8, 9, 10</sup> The generally accepted view is that photoisomerization of this kind proceeds by the intermediary formation of isomers like fulvene, benzvalene, and Dewar benzene with their further rearomatization. It has been suggested that all isomerization processes of benzene and its alkyl derivatives can be described in terms of ring permutation.<sup>11</sup> Fig. 1 shows some of the ring permutations of benzene and xylene. Note that not only the positions of the alkyl group can be changed during the ring permutation isomerization, but also the carbon atoms within the aromatic ring can be exchanged during the ring permutations. One important characteristic of the ring permutation is that the carbon and hydrogen atoms belonging to the alkyl group are not involved in the exchange with those atoms in the aromatic ring. The ring permutation has been observed in benzene and alkylsubstituted benzene in the condensed phase and the gas phase after the excitation to the  $S_1$  state.<sup>12,13,14</sup> Similar ring permutations were

also used to describe the isomerization of nitrogen containing heterocyclic aromatic molecules.<sup>15,16,17</sup>

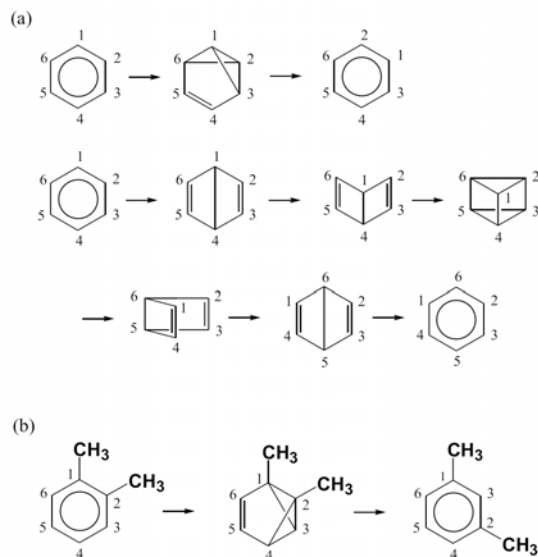


Fig. 1 Some of the isomerization pathways of benzene and xylene through ring permutation.

In contrast to the photon emission and isomerization following the excitation to the  $S_1$  state, no UV fluorescence<sup>18</sup> or isomerization has been observed after the excitation to the  $S_2$  state. Photodissociation after internal conversion to the ground state was found to be the major channel in the  $S_2$  state for benzene and alkyl-substituted benzene. All dissociation mechanisms of benzene and alkyl-substituted benzene, including toluene, and xylene, ethylbenzene, and propylbenzene after the 193 nm excitation to the  $S_2$  state have been interpreted as the direct C-H bond or C-C bond cleavages after the internal conversion to the ground electronic state.<sup>19,20,21,22,23,24,25,26,27</sup> On the other hand, photochemistry of heterocyclic aromatic molecules in the  $S_n$  ( $n \geq 2$ ) state has received little attention. Not much information about the photodissociation of heterocyclic aromatic molecules is available.

Under collisionless conditions, energy in the molecules is conserved (except the deactivation by photon emission) and molecules would not be deactivated and stabilized through the isomerization. If the initial photon energy is larger than the dissociation threshold and no photon emission occurs, molecules eventually dissociate into fragments. However, the dissociation rate and dissociation channels after isomerization can be very different from that of molecules before isomerization.

Photodissociation of  $d_3$ -toluene at 193 nm in a molecular beam was studied.<sup>28</sup> In addition to the major dissociation fragments,  $C_6H_5CD_2$ ,  $C_6H_5$  and  $CD_3$  from the dissociation of  $C_6H_5CD_3 \rightarrow C_6H_5CD_2 + D$  and  $C_6H_5CD_3 \rightarrow C_6H_5 + CD_3$ , observations of the heavy fragments  $C_7H_4D_3$ ,  $C_6H_4D$ ,  $C_6H_3D_2$ , and  $C_6H_2D_3$ , and the corresponding lighter fragment partners,  $CD_2H$ ,  $CDH_2$ , and  $CH_3$  as shown in the figure 2, suggest the existence of the other dissociation channel, i.e., isotope exchange prior to dissociation. The respective fragment ratios for  $CH_3:CH_2D:CHD_2:CD_3$  are  $5.6 \pm 0.9:9.5 \pm 0.2:6.2 \pm 1.1:100$ . Translational momentum matches of two fragments in each dissociation channel further confirm that each fragment pair,  $C_6H_5$  and  $CD_3$ ,  $C_6H_4D$  and  $CD_2H$ ,  $C_6H_3D_2$  and  $CDH_2$ ,  $C_6H_2D_3$  and  $CH_3$ , is from the dissociation of  $C_6H_5CD_3$ .

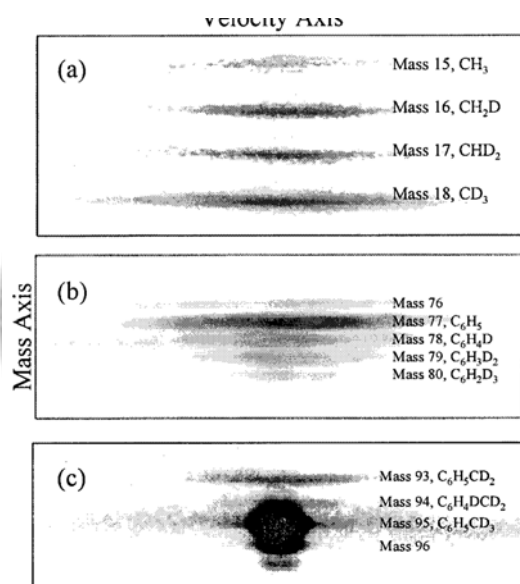


Fig. 2 Photofragment ion images of  $C_6H_5CD_3$  in three different mass regions. The image of  $m/e$  76 in part b results from two-photon dissociation. The parent molecule  $m/e$  95 and  $m/e$  96 and 97 due to the  $^{13}C$  natural abundance are also shown in image c.

Photodissociation of  $C_6H_5^{13}CH_3$  was also studied. In addition to the major dissociation channel,  $C_6H_5^{13}CD_3 \rightarrow C_6H_5 + ^{13}CH_3$ , the observation of  $^{13}CC_5H_5$  and  $CH_3$  indicates that the methyl carbon atom is also involved in the exchange with aromatic carbon atoms prior to dissociation. The experimental ratio of fragments  $CH_3:^{13}CH_3$  is 21:100.

Our observation of a small amount of  $CD_2H$ ,  $CDH_2$  and  $CH_3$  and their heavy



fragment partners,  $C_6H_4D$ ,  $C_6H_3D_2$ ,  $C_6H_2D_3$ , from the dissociation of  $C_6H_5CD_3$  clearly indicates that direct C-H bond and C-C bond cleavage is not the only dissociation mechanism. Another dissociation mechanism must exist, which allows for the exchange of D atoms in the methyl group with H atoms in the aromatic ring prior to dissociation. The small amount of  $CH_3$  resulting from  $C_6H_5^{13}CH_3$  dissociation indicates that not only are hydrogen atoms involved in the scrambling, but also that carbon atoms in both the methyl group and the aromatic group are involved in the exchange. The translational energy distributions measured from various isotope-substituted fragments were found to be very similar. They indicate that those molecules entering the other channel for isotope exchange must isomerize back to toluene before dissociation. The results can not be explained by the existing isomerization mechanisms for aromatic molecules, i.e., ring permutation, because the ring permutation involves only hydrogen and carbon atom exchange within the aromatic group.

A reasonable isomerization mechanism that explains the experimental results is the isomerization from a six-membered ring (toluene) to a seven-membered ring (cycloheptatriene). After isomerization to a seven-membered ring, isotopic scrambling of the H/D and carbon atoms occurs through H or D atom migration around the seven-membered ring. In the end, the rearomatization of cycloheptatriene to toluene and the subsequent dissociation through C-C bond cleavage results in the formation of fragments  $CD_2H$ ,  $CDH_2$  and  $CH_3$ , and their heavy fragment partners,  $C_6H_4D$ ,  $C_6H_3D_2$ ,  $C_6H_2D_3CH$ . The same mechanism can be used to explain the formation of the respective photofragments  $CH_3$ ,  $^{13}CH_3$ ,  $C_6H_5$ ,  $C_5^{13}CH_5$  from the dissociation of  $C_6H_5^{13}CH_3$ . This particular isomerization pathway is supported by *ab initio* calculations.

Similar H and D atom exchange prior to dissociation was also observed from the photodissociation of  $d_6$ -m-xylene at 193 nm in a molecular beam. In addition to the major dissociation products,  $C_6H_4CD_3CD_2$ ,  $C_6H_4CD_3$ , and  $CD_3$  from D atom elimination and C-C bond cleavage, various isotope substituted fragments, including  $C_8H_3D_6$ ,  $C_7H_3D_4$ , and  $C_7H_2D_5$ , and some of their light fragment partners,  $CD_2H$  and  $CDH_2$ , were also observed. The isomerization mechanism that was described in a previous section can be used to explain the observation from  $d_6$ -m-xylene. This six-membered ring to seven-membered ring isomerization in xylene is also supported by *ab initio* calculations.

In this work, we extend the study to photoisomerization of aniline and 4-methylpyridine. The results suggest that the isomerization from six-membered ring to seven-membered ring after internal conversion also plays a very important role in nitrogen atom contained aromatic molecules. A comparison of 4-methylpyridine and

aniline with potential energy from ab initio calculation and toluene has been made.

## Experimental

The experimental techniques have been described in chapter two and only a brief description is given here. Aniline or 4-methylpyridine vapor was formed by flowing ultrapure He (or Ne) at pressures of 500 Torr through a reservoir filled with liquid sample at 20 °C. The aniline/He or 4-methylpyridine/He mixture was then expanded through a 500  $\mu\text{m}$  pulsed nozzle at 50 °C to form a molecular beam. Aniline (99.8%), d5-aniline (99%), and 4-methylpyridine (99%) were purchased from Acros Organics. d3-4-methylpyridine (98%) was from Aldrich. These chemicals were used directly without further purification. The amounts of impurities were checked by both TOF mass spectrum and NMR spectroscopy. Mass spectrum shows that the total ion intensity of  $m/e$  values other than that of parent molecule is less than 1% in both aniline and 4-methylpyridine. In addition, NMR spectroscopy shows that no 4-methylpyridine can be detected in aniline, and no aniline can be detected in the 4-methylpyridine (less than 0.3% according to the S/N ratio of the spectrum).

## Results

### I. Aniline

Figure 3 shows the photofragment ion images of aniline. Fragments of  $m/e = 92, 91, 90, 78, 77, 76, 17,$  and  $15$  were observed. The study of photolysis laser power dependence in the region of  $1.2\sim 10 \text{ mJ/cm}^2$  showed that  $m/e = 90$  was due to the two photon dissociation and all the other fragments were from one-photon dissociation. Fragments resulted from multiphoton dissociation will not be discussed in this work.

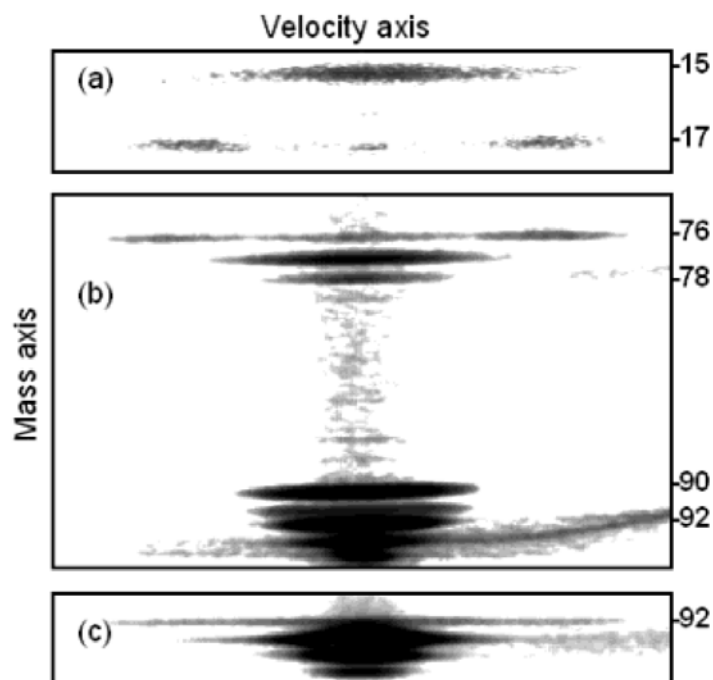


Figure 3. Photofragment ion images of aniline in three different mass regions. (a)  $m/e = 15\sim 17$ , (b)  $m/e = 75\sim 94$ , and (c)  $91\sim 95$ . The pump and probe delay time between two laser pulses were 2.5, 15, and 83  $\mu\text{s}$ , respectively. The delay time in (c) was very long such that the fragment  $m/e = 91$  flight out of the detection region.

Images of  $m/e = 92, 91, 77,$  and  $76$  represent four major dissociation channels of aniline, i.e., H,  $\text{H}_2$ ,  $\text{NH}_2$ , and  $\text{NH}_3$  eliminations, respectively. Some of the light fragment partners with ionization potentials lower than the VUV photon energy were observed, as presented in Figure 3a. In addition, the image intensity of  $m/e = 78$  is 2.8 times larger than that of  $^{13}\text{C}$  isotope of  $m/e = 77$ , indicating the existence of fragment  $\text{C}_5\text{NH}_4$ . It corresponds to the minor dissociation channel of  $\text{CH}_3$  elimination. This channel can be further confirmed by the observation of its light fragment partner  $\text{CH}_3$ , as shown in Figure 2a. The momentum matches between the heavy and light fragment partners also exclude the contribution from three-body dissociation, like the dissociation of clusters, or the contribution from cation dissociation. Some fragments corresponding to the ring opening dissociation channel like  $m/e = 66, 54, 53, 52, 41, 40,$  and  $39$  were also observed. However, they were all very small and will not be discussed in this work

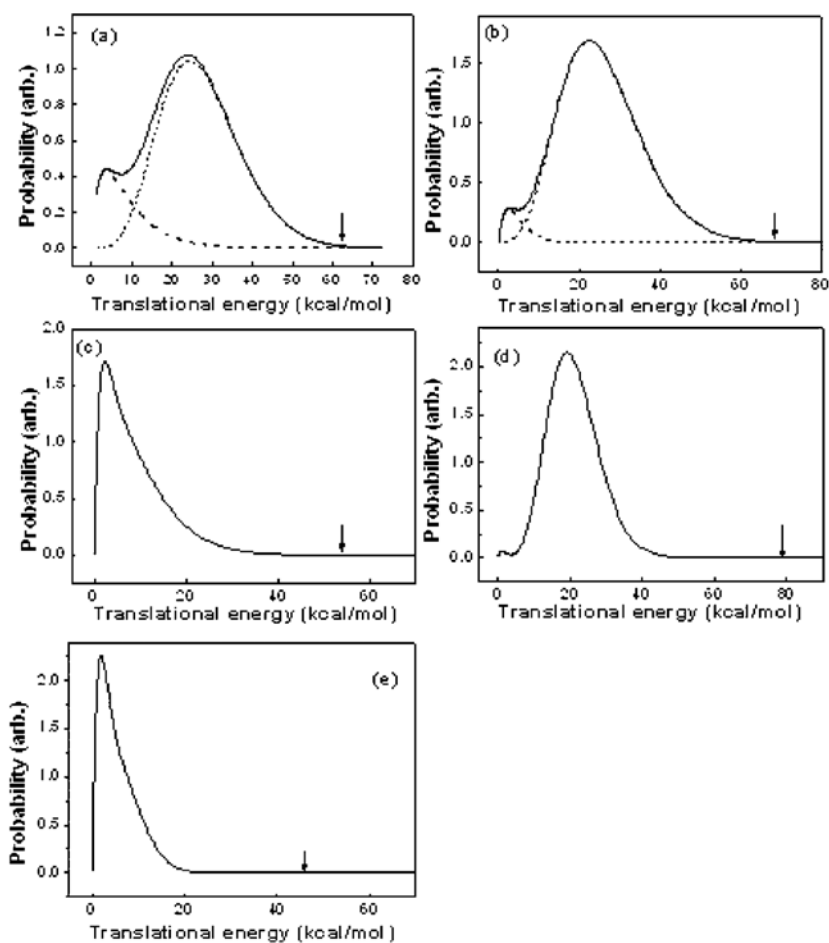


Figure 4. Photofragment translational energy distributions of (a)  $\text{C}_6\text{H}_5\text{NH}_2 \rightarrow \text{C}_6\text{H}_5\text{NH} + \text{H}$ , (b)  $\text{C}_6\text{H}_5\text{NH}_2 \rightarrow \text{C}_6\text{H}_3\text{NH}_2 + \text{H}_2$ , (c)  $\text{C}_6\text{H}_5\text{NH}_2 \rightarrow \text{C}_6\text{H}_5 + \text{NH}_2$ , (d)  $\text{C}_6\text{H}_5\text{NH}_2 \rightarrow \text{C}_6\text{H}_4 + \text{NH}_3$ , (e)  $\text{C}_6\text{H}_5\text{NH}_2 \rightarrow \text{C}_5\text{NH}_4 + \text{CH}_3$ . Arrows indicate the maximum available energies in each dissociation channel.

Photofragment translational energy distributions obtained from the image are illustrated in Figure 4. Translation energy distribution of H atom elimination shows two components. The ratio between the fast and slow components is about 3:1. For the slow component, the average translational energy release is small and the probability of fragment translational energy distribution decreases monotonically with the increase of energy. These are the typical characteristics of the dissociation from hot molecules. On the other hand, the average released translational energy for the fast component is large, and the peak of the distribution is located at 24 kcal/mol. It must result from a repulsive state, or a state with a large exit barrier. Image intensity profiles of  $m/e$  ) 92 at the

photolysis laser polarization parallel and perpendicular to the VUV laser beam are shown in Figure 5. They have the same shape and intensity, indicating the isotropic fragment distribution of both the slow and fast H atom components.

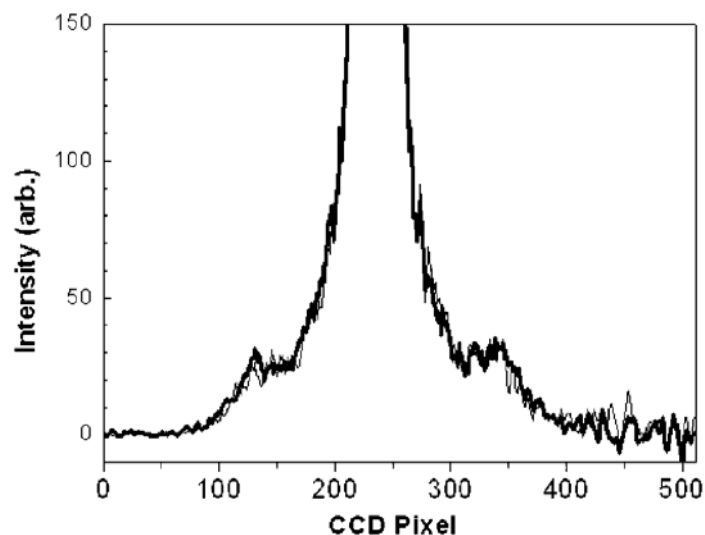


Figure 5. Image intensity profiles of  $m/e = 92$  at the photolysis laser polarization parallel (thick solid line) and perpendicular (thin solid line) to the VUV laser beam.

Two-component translational energy distribution was also observed in  $H_2$  elimination channel. The ratio between the fast and slow components is about 10:1. For the  $NH_3$ ,  $CH_3$ , and  $NH_2$  eliminations, however, there is only one component in the translational energy distribution. A dissociation rate of  $(4.5 \pm 1) \times 10^6 \text{ s}^{-1}$  was obtained from the  $m/e = 91, 78, 77,$  and  $76$  product growths with respect to the delay time between pump and probe laser pulses. The same dissociation rate suggests the dissociation of these channels must occur in the same electronic state.

Isotope substituted  $d_5$ -aniline was also studied. The fragment ion images are shown in Figure 6. It shows that  $C_6D_4$ , corresponding to  $NH_2D$  elimination is the major products from the ammonia molecular elimination channel. However, small amount of fragments  $m/e = 79$  and  $78$ , corresponding to the  $NHD_2$  and  $ND_3$  elimination were also observed. For amino group elimination,  $NH_2$  elimination is the dominant process, as it is shown at  $m/e = 82$ . But small amount of fragments corresponding to  $NHD$  and  $ND_2$  elimination were also found. Although fragments of  $C_6D_3H$ ,  $C_6D_3H_2$ ,  $C_6D_4H$ ,  $C_6D_5$ , corresponding to the eliminations of  $NH_2D$ ,  $ND_2$ ,  $NHD$ , and  $NH_2$  have the same masses as those of  $C_5ND_2H_2$ ,  $C_5ND_3H$ , and  $C_5ND_4$ , corresponding to the eliminations of  $CD_3$ ,  $CD_2H$ , and

CDH<sub>2</sub>. However, the study of nonisotope labeled aniline suggests that the contribution from methyl group elimination is much smaller than that from ammonia and amino group elimination. In addition, the image intensity distribution of ammonia elimination is very different from that of amino group elimination. They can be separated from each other easily. Similar isotope substituted fragments were also observed in both H atom and H<sub>2</sub> elimination channels. In these channels, H atom, HD, and D<sub>2</sub> molecule eliminations are the major channels and D atom elimination is the minor channel. However, no H<sub>2</sub> elimination was observed. The observation of these fragments indicates the D atom and H atom exchange to some extent prior to dissociation.

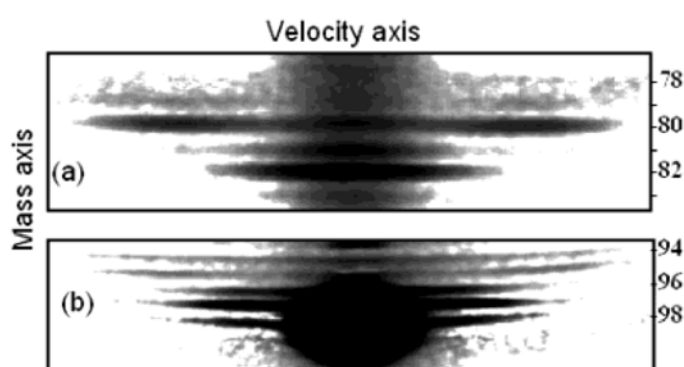


Figure 6. Photofragment ion images of d<sub>5</sub>-aniline (a)  $m/e = 78\sim 83$  (b)  $m/e = 94\sim 100$ .

The relative intensities of these isotope substituted fragments and their translational energy distributions are shown in Figure 7. Although the translation energy distribution of H atom elimination channel has two components, however, the distribution of D atom elimination channel has only one component, and it decreases monotonically with the increase of energy. It suggests that dissociation mechanisms of H atom and D atom elimination are different. For the analogous H<sub>2</sub>, NH<sub>2</sub>, and NH<sub>3</sub> elimination channels, the translational energy distributions of these isotope substituted fragments show very similar distributions to each other, indicating the similar dissociation mechanism.

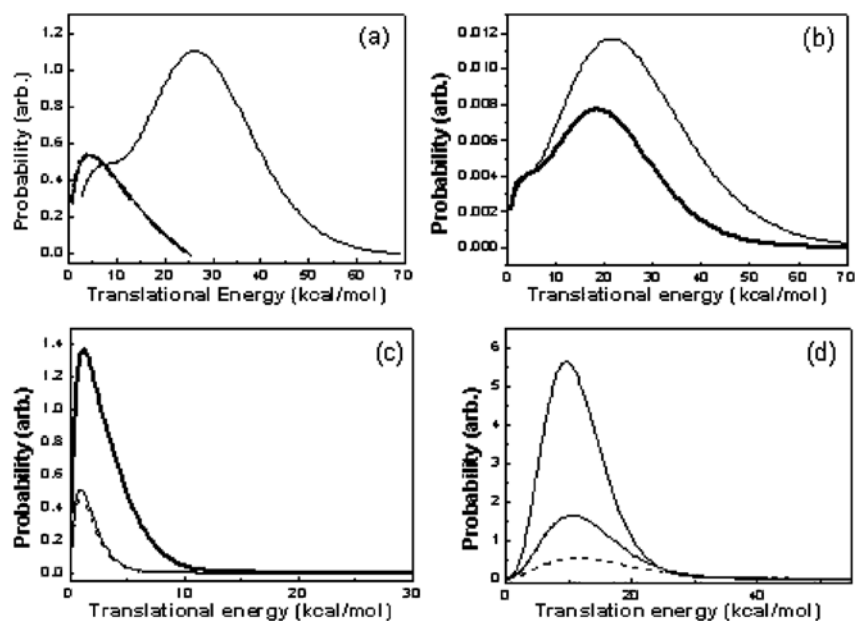


Figure 7. Photofragment translational energy distributions of d<sub>5</sub>-aniline. (a) H (thin), D (thick) elimination. (b) HD (thin), D<sub>2</sub> (thick) elimination. (c) NH<sub>2</sub> (thick), NHD (dot), and ND<sub>2</sub> (thin) elimination. (d) NH<sub>2</sub>D (thin), NHD<sub>2</sub> (thick), ND<sub>3</sub> (dot) elimination.

## II. 4-Methylpyridine.

4-Methylpyridine shows very similar dissociation channels to those of aniline. However, fragment relative intensities are very different. Photofragment ion images from the photodissociation of 4-methylpyridine at 193 nm are shown in Figure 8. The study of photolysis laser power dependence in the region of 7~28 mJ/cm<sup>2</sup> showed that  $m/e = 90$  and  $m/e = 91$  resulted from two photon absorption. Images of  $m/e = 92$  and 78 have the largest intensities, they represent two major dissociation channels of 4-methylpyridine, i.e.,  $C_5NH_4CH_3 \rightarrow C_5NH_4CH_2 + H$ , and  $C_5NH_4CH_3 \rightarrow C_5NH_4 + CH_3$ . It is interesting to note that images of  $m/e = 77$  and 76 with small intensities were observed. They correspond to the NH<sub>2</sub> and NH<sub>3</sub> eliminations. In addition, fragment ions with small intensities of  $m/e = 66, 54, 53, 52, 41, 40,$  and 39 were also observed. However, these signals are very small and they will not be discussed in this work.

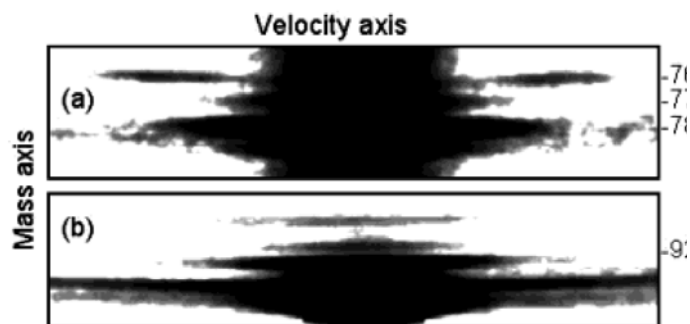


Figure 8. Photofragment ion images of 4-methylpyridine (a)  $m/e = 75\sim 80$ . (b)  $m/e = 90\sim 95$ .

The fragment translational energy distributions obtained from the ion image are presented in Figure 9. Compared to the maximum available energies, the average released translation energies are all very small. They are only 5.4%, 7.1%, 19.4%, and 6.6% of the maximum available energies for H atom, CH<sub>3</sub>, NH<sub>3</sub>, and NH<sub>2</sub> elimination channels, respectively.

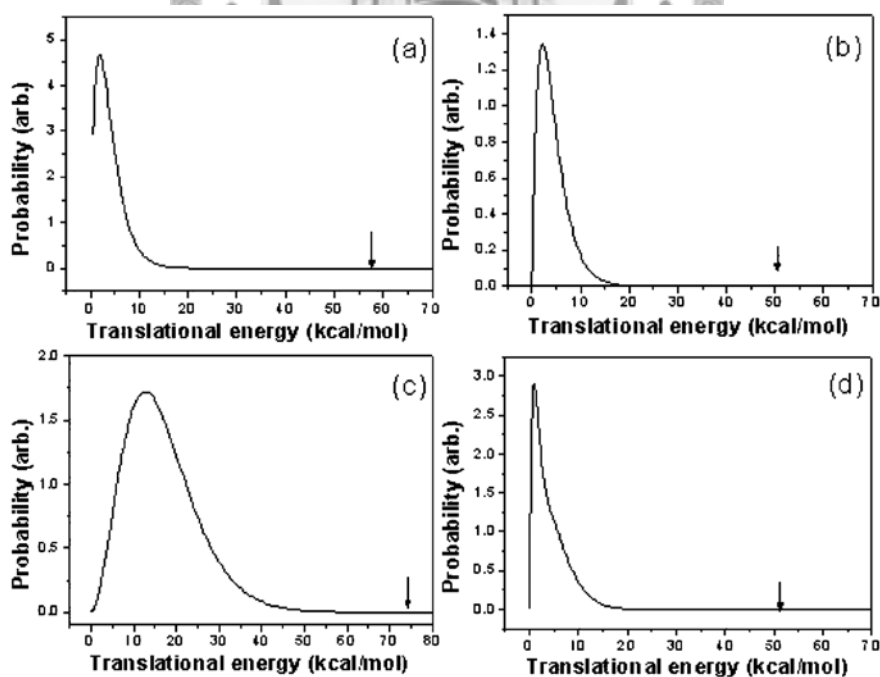


Figure 9. Photofragment translational energy distributions of reactions (a)  $C_5NH_4CH_3 \rightarrow C_5NH_4CH_2 + H$  (b)  $C_5NH_4CH_3 \rightarrow C_5NH_4 + CH_3$  (c)  $C_5NH_4CH_3 \rightarrow C_6H_4 + NH_3$  (d)  $C_5NH_4CH_3 \rightarrow C_6H_5 + NH_2$ . Arrows indicate the maximum available energies in each



dissociation channel.

The similar dissociation channels were also observed in the photodissociation of d<sub>3</sub>-4-methylpyridine. Photofragment images are shown in Figure 10.  $m/e = 96$  was from parent molecule,  $m/e = 95$  was from the contribution of H atom elimination as well as some incomplete isotope-labeled d<sub>2</sub>-methylpyridine (5%), and  $m/e = 94$  corresponded to the D atom elimination. Photofragments of  $m/e = 78, 79, 80,$  and  $81$  were mainly from C<sub>5</sub>NH<sub>4</sub>, C<sub>5</sub>NH<sub>3</sub>D, C<sub>5</sub>NH<sub>2</sub>D<sub>2</sub>, and C<sub>5</sub>NHD<sub>3</sub>, as a result of CD<sub>3</sub>, CHD<sub>2</sub>, CH<sub>2</sub>D, and CH<sub>3</sub> elimination. Since the ionization potential of NH<sub>2</sub> is larger than the VUV photon energy we used in this work, no amino radicals could be ionized. The relative branching ratios of CHD<sub>2</sub>, CH<sub>2</sub>D, and CH<sub>3</sub> elimination channels can be obtained directly from the intensity of light fragments in order to avoid the interference from ND<sub>2</sub>, NHD, and NH<sub>2</sub> eliminations. Fragment ion intensity ratios were found to be CD<sub>3</sub>:CD<sub>2</sub>H:CDH<sub>2</sub>:CH<sub>3</sub> = 91:3.6:4.5:0.9. Since the branching ratios of the analogues NH<sub>2</sub> and NH<sub>3</sub> elimination channels are very small, we did not intend to observe these channels for this isotope-labeled compound. The observation of various D atom substituted methyl radicals indicates that H and D atoms exchange before dissociation.

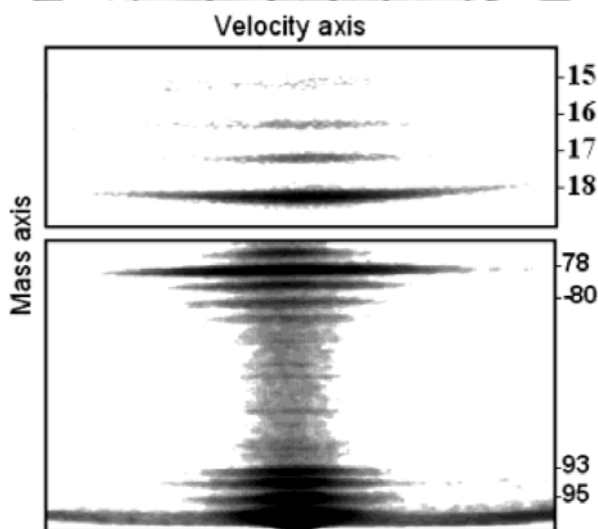


Figure 10. Photofragment ion images of d<sub>3</sub>-picoline (a)  $m/e = 15\sim 18$  (b)  $m/e = 77\sim 96$ .

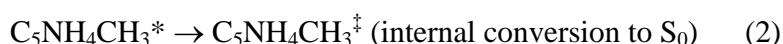
Dissociation rates of  $(1.4 \pm 0.8) \times 10^6 \text{ s}^{-1}$  and  $(1.8 \pm 0.5) \times 10^6 \text{ s}^{-1}$  were obtained from product growths with respect to the delay time between pump and probe laser pulses for C<sub>5</sub>NH<sub>4</sub>CH<sub>3</sub> and C<sub>5</sub>NH<sub>4</sub>CD<sub>3</sub>, respectively. The dissociation rate of C<sub>5</sub>NH<sub>4</sub>CD<sub>3</sub> is only a little slower than that of C<sub>5</sub>NH<sub>4</sub>CH<sub>3</sub>.

## Discussion

### I. Dissociation and Isomerization Mechanisms.

#### A. 4- Methylpyridine.

Previous studies of methylpyridine mainly focused on the excitation to the  $S_1$  and  $S_2$  states. The fluorescence quantum yield and intersystem crossing quantum yield decrease rapidly with the decrease of photon wavelength from 290 to 250 nm.<sup>26</sup> Fluorescence quantum yield changes from  $10^{-4}$  at 290 nm to less than  $2 \times 10^{-6}$  at 250 nm and the quantum yield of intersystem crossing also drops from 0.8 to 0.04. Internal conversion to the ground electronic state becomes the dominant process. However, very little study has been done at the region of 193 nm. Since the methyl group is not an electronic chromophore in this region, UV absorption of 4-methylpyridine at 193 nm only correlates to the excitation of the electrons of the pyridyl ring. The excitation of the pyridyl ring results in an excited state, stable with respect to dissociation. Dissociation must occur either through the coupling of the stable and repulsive states, or after the internal conversion from an initial excited state to a lower electronic state. Since the dissociation in the ground state usually results in a limited release of kinetic energy due to their extensive energy randomization among vibrational degrees of freedom and has a slow dissociation rate, the observation of small kinetic energy release and slow dissociation rate suggest all of the 4-methylpyridine molecules relax to the ground electronic state through internal conversion prior to dissociation. The results can be represented by the following reactions.

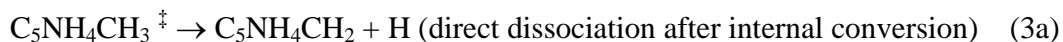


Here,  $C_5NH_4CH_3^*$  represents 4-methylpyridine in the electronic excited states, and  $C_5NH_4CH_3^\ddagger$  represent 4-methylpyridine in the ground electronic state, respectively.

After internal conversion to the ground electronic state, 4-methylpyridine molecules could dissociate through various possible dissociation channels. Statistical transition-state theory has predicted that, given comparable pre-exponential factors for different bond fissions, the reaction pathway with the lowest energetic barrier should dominate the dissociation. Since the C-CH<sub>3</sub> and methyl C-H bond energies are relatively small compared to the other bond energies in the aromatic ring and this dissociation have no exit barrier because of the production of two radicals in the ground electronic state, H

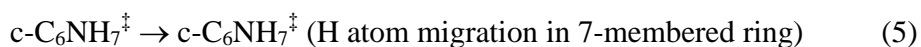
atom and CH<sub>3</sub> eliminations are expected to be the major dissociation channels.

Indeed, they are the major channels observed in the experiment. These dissociation channels are described by the following reactions.



However, the observation of C<sub>6</sub>H<sub>5</sub> shows that a small fraction of 4-methylpyridine molecules go through a complicated isomerization prior to dissociation. To produce fragment C<sub>6</sub>H<sub>5</sub> and NH<sub>2</sub> from 4-methylpyridine, H atoms in the molecule must migrate until nitrogen atom gathers two H atoms and then C-N bond breaks. This involves successive H atom migration and ring isomerization. The similar isomerization must occur in order to generate fragments C<sub>6</sub>H<sub>4</sub> and NH<sub>3</sub>. Since the minor channels observed in 4-methylpyridine correspond to the major channels in aniline and they have the similar translational energy distributions, some of the 4-methylpyridine must isomerize to aniline before dissociation occurs. A reasonable isomerization mechanism that explains the experimental results is the isomerization similar to that of toluene and xylene found in our previous experiments. The isomerization starts from the change of 4-methylpyridine to a seven-membered ring isomer.

After the isomerization to the seven-membered ring isomer, the exchange of relative nitrogen and carbon atoms' positions occur through H migration around the seven-membered ring. In the end, the rearomatization of seven-membered ring to six-membered ring produces both methylpyridine and aniline. The subsequent dissociation produces all kinds of fragments we observed in the experiment.



Although reaction 7e was not observed in 4-methylpyridine due to the obstacle of multiphoton dissociation, it is likely to occur since it is one of the major dissociation channels of aniline.

The observation of CD<sub>3</sub>, CD<sub>2</sub>H, CDH<sub>2</sub>, and CH<sub>3</sub>, from d<sub>3</sub>-4-methylpyridine indicates some molecules undergo isotope exchange prior to dissociation. These exchanges can be achieved by the H and D atom migration around seven-membered ring in reaction 5. Fragment isotope ratios of [CH<sub>3</sub> + CH<sub>2</sub>D + CHD<sub>2</sub>] / [CD<sub>3</sub>] from d<sub>3</sub>-4-methylpyridine suggest that 10% of 4-methylpyridine isomerize to seven-membered ring isomers and then rearomatize back to methylpyridine prior to dissociation.

## B. Aniline.

Aniline is one of the aromatic molecules that the UV photochemistry has been studied extensively. High resolution laser induced fluorescence spectroscopy of the S<sub>1</sub> state has been investigated, and the fluorescence lifetime and quantum yield of each vibronic level were obtained.<sup>29</sup> It shows that the fluorescence lifetime is about 5~9 ns and quantum yield is 0.1~0.2, depending on the vibronic levels. Intersystem crossing is the main nonradiative process in the S<sub>1</sub> state relaxation. The rate of intersystem crossing as large as 8.2 x 10<sup>7</sup> s<sup>-1</sup> was found.<sup>29</sup> The decay of the triplet state generated from the S<sub>1</sub> state through intersystem crossing is very fast. Triplet state lifetime at the energy level corresponding to band origin of the S<sub>1</sub> state (294 nm) is 5653 ns, but it decreases rapidly as the energy increases. Lifetime as short as 168 ns was observed at energy 3800 cm<sup>-1</sup> above the S<sub>1</sub> band origin.<sup>30</sup> Although the intersystem crossing rate from S<sub>1</sub> to T<sub>1</sub> is fast, however, no phosphorescence was observed in the gas phase due the rapid decay from T<sub>1</sub> to S<sub>0</sub>.

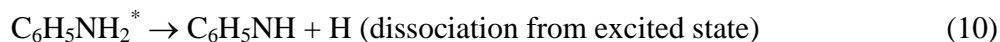
Compared to the studies of the S<sub>1</sub> state, the photochemistry at 193 nm has received little attention. Early experimental investigation<sup>31, 32</sup> and recent theoretical study<sup>31</sup> suggest the absorption of 193 nm photons corresponds to the excitation of electrons of the phenyl ring ( $\pi$ - $\pi^*$ ). Internal conversion of the phenyl ring electronic excited state at such high energy level usually is very fast. The dissociation therefore is expected to be very similar to that of 4-methylpyridine, i.e., dissociation occurs in the ground state and the channels with low dissociation barrier heights are the dominant processes. Indeed, cleavage through weak chemical bonds such as N-H and C-N bonds was found to be the major dissociation channels. Dissociation occurs in the ground electronic state is further confirmed by the fact that the maximum translational energy release of the H<sub>2</sub> elimination

reaches the maximum available energy of the reaction  $C_6H_5NH_2 \rightarrow C_6H_3NH_2 + H_2$ . Since the fragment with maximum translational energy corresponds to the products  $C_6H_3NH_2$  and  $H_2$  produced in the ground electronic state and the ground state of these two close shell fragments only correlates to the ground state of the parent molecule, the dissociation must result in the ground electronic state.

The observation of fragment  $C_5NH_4$  and  $CH_3$  from aniline and various isotope-substituted fragments such as  $NH_3$ ,  $NH_2D$ ,  $NHD_2$  from  $d_5$ -aniline can be explained by the similar isomerization and dissociation mechanism described in 4-methylpyridine, i.e., the isomerization from aniline to seven-membered ring, followed by H and D atom migration in seven-membered ring, and then the rearomatization to both aniline and methylpyridine prior to dissociation.

Although there are many similarities between the dissociation properties of 4-methylpyridine and aniline, however, some difference was also observed. For example, the elimination of close shell molecules, like  $H_2$ ,  $NH_3$ , plays a very important role in aniline, but they were not observed in the direct dissociation of 4-methylpyridine. In addition, the fast component in the translational energy distributions of H atom elimination was only found in aniline. This component must result from the dissociation in the excited state of a repulsive potential, or from an electronic state with a large exit barrier. Since the reverse reaction of H atom elimination has no barrier in the ground electronic state, the fast component must result from the dissociation in the electronic excited state. Very recently, it was proposed that in several aromatic molecules, a  $\pi \sigma^*$  state exists in the vicinity of  $S_1$  state,<sup>33,34,35</sup> and the potential energy surface of this state is essentially a repulsive state along the N-H coordinate. It is possible that the fast component of H atom elimination we observed in the experiment resulted from this state. Since the fragment distribution of the fast component is isotropic, dissociation does not occur directly on the repulsive potential energy surface. Instead, dissociation must occur indirectly through the coupling between the repulsive surface and other excited states on a time scale much longer than the parent molecule rotation. On the other hand, H atom elimination also has an exit barrier in the triplet state. Dissociation from the triplet state cannot be totally excluded without the additional information about the intersystem crossing quantum yield at this wavelength.

The isomerization and dissociation mechanism of aniline can be summarized as followings.



Reactions following reaction 12 are the same as reactions (5)~(7).

According to this isomerization and dissociation mechanisms, the ratio  $[\text{ND}_3 + \text{NHD}_2]/[\text{NH}_2\text{D}]$  observed from  $d_5$ -aniline indicates that 23% of aniline in the ground electronic state isomerize to seven-membered ring, followed by H/D atom migration, and then rearomatize to aniline prior to dissociation.

Although the slow dissociation rates and translational energy distributions obtained from the experimental measurement suggest that both aniline and 4-methylpyridine dissociation occurs on the ground electronic state (except the fast component of H atom elimination in aniline), the possibility that isomerization occurs to some extent in the excited state before molecules reach the ground state through internal conversion cannot be totally excluded. This kind of isomerization, like pyridine undergoes ring opening isomerization in the excited state, has been observed.<sup>36</sup> However, the different intermediates produced directly in the electronic excited state from 4-methylpyridine and aniline, respectively, must be able to isomerize to each other with low enough barrier heights in order to explain the experimental results. Due to the lack of excited-state potential energy surfaces at this moment, there is no compelling evidence to claim their intermediacy in the present case.

## II. Potential Energy Surface.

This particular isomerization between six-membered ring and seven-membered ring is supported by ab initio calculations. The energies of isomers and various transition states along the isomerization and dissociation pathways from ab initio calculation are shown in Figure 11. In the calculation, the geometries were optimization by B3LYP/

6-31G\* and the energies were calculated by G3 scheme. The dissociation of 4-methylpyridine has barrier heights of 91.0 kcal/mol for C-H bond cleavage, and 105.9 kcal/mol for C-C bond cleavage. The isomerization of 4-methylpyridine to seven-membered ring starts with the H atom shift from methyl group to the carbon atom next to the methyl group, followed by the formation of bicyclo-isomer as an intermediate, and finally the isomerization to form seven-membered ring isomer. The six-membered ring to seven-membered ring isomerization has a barrier height of 88.7 kcal/mol. Since the barrier heights are all very close in energy, isomerization to seven-membered ring competes with C-C bond and C-H bond dissociation. Although most of the 4-methylpyridine molecules dissociate directly through C-C and C-H bond cleavages after the internal conversion, however, experimental data shows that at least 10% of 4-methylpyridine molecules isomerize to seven-membered ring prior to dissociation.

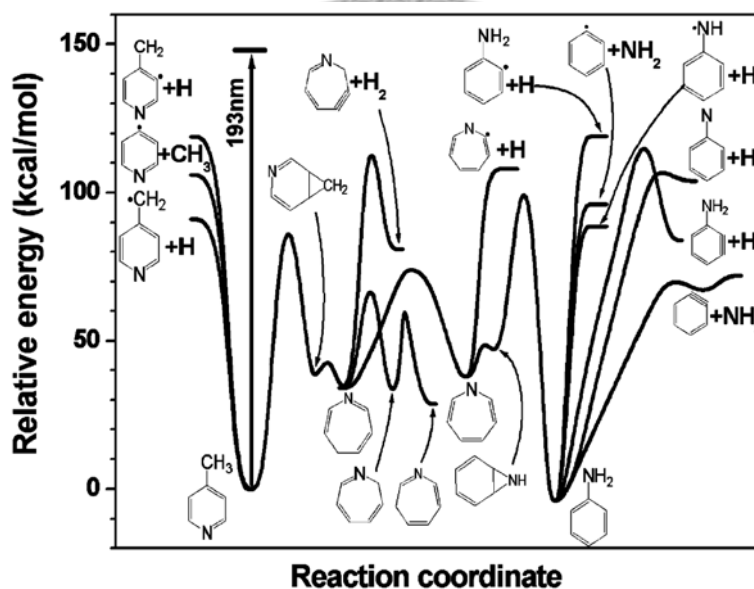


Figure 11. Energy diagram for isomerization and dissociation of 4-methylpyridine and aniline. The energies were computed at the G3 level of theory and the geometry optimized by B3LYP/6-31G\*.

Dissociation and isomerization barrier heights in the ground electronic state of aniline show the similar properties to that of 4-methylpyridine. Eliminations of H atom, H<sub>2</sub>, NH<sub>2</sub>, NH<sub>3</sub> have barrier heights of 86.4, 104, 116, 100.7, and 72 kcal/mol, respectively. Isomerization of aniline to seven-membered ring isomer also starts with the H atom shift from amino group to the carbon atom next to the amino group, forming a

bicyclointermediate, and then followed by the isomerization to seven-membered ring. The barrier height of the isomerization is only 102.4 kcal/mol, which is very close to various dissociation barrier heights. Isomerization to seven-membered ring therefore competes with the direct dissociation channels in the ground electronic state. Most of the aniline molecules in the ground electronic state dissociate directly, but at least 23% of aniline in the ground-state isomerize to seven-membered ring.

It is interesting to note that there are four different seven-membered ring isomers, depending on the positions of H atoms. Among these isomers, 1-aza-1,3,6-cycloheptatriene and 1-aza-2,4,6-cycloheptatriene can be produced directly from 4-methylpyridine and aniline respectively after the six-membered ring to seven-membered ring isomerization. The other isomers including 1-aza-2,4,7-cycloheptatriene and 1-aza-1,3,5-cycloheptatriene require further H atom migration around the seven-membered ring. For example, 1-aza-1,3,5-cycloheptatriene can be produced from 1-aza-1,3,6-cycloheptatriene through 2,5-H shift, and 4,7-H shift of 1-aza-1,3,5-cycloheptatriene can generate 1-aza-2,4,7-cycloheptatriene. The isomerization between 1-aza-1,3,6-cycloheptatriene and 1-aza-2,4,6-cycloheptatriene can be achieved through 1,5-H shift. The barrier heights between these seven-membered ring isomers are only about 32~40 kcal/mol. Consequently, H and D atoms can easily migrate around the seven-membered ring due to the low barrier heights, resulting in several seven-membered ring isomers. The exchange of H and D atom and the change of relative nitrogen and carbon atoms' positions all come from these H or D atom migration around the seven-membered ring.

The potential energies corresponding to the elimination of close shell molecules including H<sub>2</sub> and NH<sub>3</sub> are also shown in Figure 11. NH<sub>3</sub> elimination starts from the migration of H atom in the position 2 toward N atom of the amino group, followed by forming the C<sub>6</sub>H<sub>4</sub>-NH<sub>3</sub> complex, and then NH<sub>3</sub> elimination occurs. It has the lowest dissociation threshold. The maximum available energy is as large as 75 kcal/mol. As a result, the photofragment translational energy release in this channel is relatively large.

In contrast to NH<sub>3</sub> elimination, there are many dissociation channels leading to H<sub>2</sub> elimination. They can be classified into two types of H<sub>2</sub> elimination, according to the values of the exit barrier height. The H atoms can be both eliminated from phenyl ring and produce 2-aminobenzynes and 3-aminobenzynes. The calculation shows that they are endothermic by 80.6 and 83.8 kcal/mol and have the dissociation barriers of 113.4 and 119.3 kcal/mol, respectively. The exit barrier heights for this type of elimination channel are as large as 32.8 and 35.5 kcal/mol, respectively. This type of H<sub>2</sub> elimination occurs



through the H atom migration in phenyl ring, and then H<sub>2</sub> dissociated from the parent molecule through three-center elimination. It is similar to the benzene H<sub>2</sub> elimination mechanism.<sup>37</sup> Another channel belonging to this type of elimination is the H<sub>2</sub> elimination from seven-membered ring. The barrier height is 114.6 kcal/mol, and it is endothermic by 81 kcal/mol. The exit barrier of 33 kcal/mol in this channel is similar to the values in the other two channels. For the other type of H<sub>2</sub> elimination, H atoms can be both eliminated from amino group, or one is from amino group and the other is from phenyl ring. This type of H<sub>2</sub> elimination has dissociation barriers of 104.2 and 11 kcal/mol and is endothermic by 103.1 and 105.7, respectively. In contrast to the other type of H<sub>2</sub> elimination, the exit barriers are small. They are only 1.1 and 4.3 kcal/mol.

The photofragment translational energy distribution of the H<sub>2</sub> elimination shows two components, indicating two different dissociation mechanisms. For the fast component, the average released translational energy is large, and the peak of the distribution is located at 23 kcal/mol. It must result from a dissociation channel with large exit barrier, i.e., both H atoms are eliminated from phenyl ring and benzyne-like derivatives are produced, or from the seven-membered ring isomer. This can be confirmed from the fact that the maximum translational energy of the fast component reaches the maximum available energies of these reaction C<sub>6</sub>H<sub>5</sub>NH<sub>2</sub> → C<sub>6</sub>H<sub>3</sub>NH<sub>2</sub> (or c-C<sub>6</sub>NH<sub>5</sub> within experimental error) + H<sub>2</sub>, corresponding to the products C<sub>6</sub>H<sub>3</sub>NH<sub>2</sub> (or c-C<sub>6</sub>NH<sub>5</sub>) and H<sub>2</sub> produced in the ground electronic state. On the other hand, the slow component has limited translational energy released. It must result from a dissociation channels with small exit barrier, corresponding to both H atoms eliminated from amino group or one from amino group and the other from phenyl ring. However, this type of H<sub>2</sub> elimination is less than 10% of the total H<sub>2</sub> elimination.

### III. Comparison to Photodissociation of Toluene.

Toluene has the similar structure to those of methylpyridine and aniline. Since the photophysics and photochemistry processes of toluene have been studied extensively, it is thus interesting to compare the photodissociation of methylpyridine and aniline to that of toluene. Toluene in the S<sub>2</sub> state produced by 200 nm excitation was found to undergo fast internal conversion to the S<sub>0</sub> and S<sub>1</sub> states with a lifetime of ~50 fs.<sup>38</sup> Dissociation rate of toluene after 193 nm excitation under collision-free conditions was found to be 2 x 10<sup>6</sup> s<sup>-1</sup>.<sup>28</sup> The fast relaxation from the S<sub>2</sub> and S<sub>1</sub> states to S<sub>0</sub>, and the slow dissociation rate suggest the dissociation occurs from the vibrationally excited ground electronic state after

internal conversion. In the ground state, 75% of hot toluene dissociate directly through methyl H atom and CH<sub>3</sub> elimination. However, 25% of toluene isomerize to seven-membered ring and rearomatize back to toluene, and eventually they all dissociate through H and CH<sub>3</sub> elimination channels from six-membered ring. No dissociation from seven-membered ring isomer was observed.

4-methylpyridine has very similar dissociation properties to those of toluene. Most of the 4-methylpyridine dissociates through methyl C-H and C-CH<sub>3</sub> bond cleavages after internal conversion. Since seven-membered ring can isomerize to both methylpyridine and aniline, the ratio of [CH<sub>3</sub> + CH<sub>2</sub>D + CHD<sub>2</sub>]/ [CD<sub>3</sub>] from d<sub>3</sub>-4-methylpyridine suggest that more than 10% of 4-methylpyridine molecules isomerize to seven-membered ring and then rearomatize to six-membered ring prior to dissociation. On the other hand, aniline shows different dissociation properties from those of toluene. Excited-state dissociation plays an important role at this photon energy. 75% of H elimination occurs in the electronic excited state. Although the NH<sub>2</sub> and H atom eliminations from the ground state and the isomerization to seven-membered ring are analogous to those of toluene, however, the elimination of closed shell molecules, like H<sub>2</sub> and NH<sub>3</sub> in aniline, were not observed in toluene. Indeed, closed shell molecule elimination channel has not been observed for any alkylbenzenes in this photon energy region.

Compared to 25% of toluene, at least 10% of 4-methylpyridine and more than 23% of aniline in the ground state isomerize to seven-membered ring and then rearomatize to six-membered ring prior to dissociation. The results demonstrate that this isomerization not only plays a very important role in toluene and xylene, but also plays a very important role in nitrogen atom contained aromatic molecules. The significance of this isomerization is that the carbon, nitrogen, and hydrogen atoms belonging to the alkyl or amino group are involved in an exchange with those atoms in the aromatic ring during the isomerization. They cannot be achieved by the other isomerization.

## References

---

- <sup>1</sup> C. E. Otis, J. L. Knee, P. M. Johnson, *J. Chem. Phys.*, **78**, 2091(1983).
- <sup>2</sup> N. Nakashima, K. Yoshihara, *J. Chem. Phys.*, **77**, 6040(1982).
- <sup>3</sup> M. Sumitani, D. V. Oconnor, Y. Takagi, N. Nakashima, K. Kamogawa, Y. Udagawa, K. Yoshihara, *Chem. Phys.*, **93**, 359(1985).
- <sup>4</sup> M. A. Duncan, T. G. Dietz, M. G. Liverman, R. E. Smalley, *J. Phys. Chem.*, **85**,

- 
- 7(1981).
- <sup>5</sup> M. Suto, W. Wang, J. Shan, L. C. Lee, *J. Quant. Spectrosc. Radiat. Transfer*, **48**, 79(1992).
- <sup>6</sup> K. E. Wilzbach, L. Kaplan, *J. Am. Chem. Soc.*, **86**, 2307(1964).
- <sup>7</sup> A. W. Burgstahler, P. L. Chien, *J. Am. Chem. Soc.*, **86**, 2940(1964).
- <sup>8</sup> L. Kaplan, K. E. Wilzbach, W. G. Brown, S. S. Yang, *J. Am. Chem. Soc.*, **87**, 675(1965)
- <sup>9</sup> K. E. Wilzbach, L. Kaplan, *J. Am. Chem. Soc.*, **87**, 4004(1965).
- <sup>10</sup> I. E. Den Besten, L. Kaplan, K. E. Wilzbach, *J. Am. Chem. Soc.*, **90**, 5868(1968).
- <sup>11</sup> D. Bryce-Smith, A. Gilbert, In *Rearrangement in Ground and Excited States* ( De Mayo, P., Ed.; Academic Press: New York, vol. 3, 1980).
- <sup>12</sup> A. H. Jackson, G. W. Kenner, G. McGillvray, G. S. Sach, *J. Am. Chem. Soc.*, **87**, 675(1965).
- <sup>13</sup> K. E. Wilzbach, A. L. Harkness, L. Kaplan, *J. Am. Chem. Soc.*, **90**, 1116(1968).
- <sup>14</sup> K. E. Wilzbach, L. Kaplan, *J. Am. Chem. Soc.*, **86**, 2307(1964).
- <sup>15</sup> K. E. Wilzbach, D. J. Rausch, *J. Am. Chem. Soc.*, **92**, 2178(1970).
- <sup>16</sup> S. Caplain, A. Lablache-Combier, *Chem. Commun.* 1247(1970).
- <sup>17</sup> D. W. Johnson, V. Austel, R. S. Feld, D. M. Lemal, *J. Am. Chem. Soc.*, **92**, 7505(1970).
- <sup>18</sup> N. Nakashima, K. Yoshihara, *J. Chem. Phys.*, **79**, 2727(1983).
- <sup>19</sup> S. T. Tsai, C. K. Lin, Y. T. Lee, C. K. Ni, *J. Chem. Phys.*, **113**, 67,(2000).
- <sup>20</sup> S. T. Tsai, C. L. Huang, Y. T. Lee, C. K. Ni, *J. Chem. Phys.*, **115**, 2449(2001).
- <sup>21</sup> H. Hippler, V. Schubert, J. Troe, H. Wendelken, *J. Chem. Phys.*, **84**, 253(1981).
- <sup>22</sup> J. Park, R. Bersohn, I. Oref, *J. Chem. Phys.*, **93**, 5700(1990).
- <sup>23</sup> R. Fröchtenicht, *J. Chem. Phys.*, **102**, 4850(1994).
- <sup>24</sup> N. Nakashima, K. Yoshihara, *J. Phys. Chem.*, **93**, 7763(1989).
- <sup>25</sup> K. Luther, J. Troe, K. L. Weitzel, *J. Phys. Chem.*, **94**, 6316(1990).
- <sup>26</sup> U. Brand, H. Hippler, L. Lindemann, J. Troe, *J. Phys. Chem.*, **94**, 6305(1990).
- <sup>27</sup> T. Shimada, Y. Ojima, N. Nakashima, Y. Izawa, C. Yamanaka, *J. Phys. Chem.*, **96**, 6298(1992).
- <sup>28</sup> C. K. Lin, C. L. Huang, J. C. Jiang, H. Chang, S. H. Lin, Y. T. Lee, C. K. Ni, *J. Am. Chem. Soc.*, **124**, 4068(2002).
- <sup>29</sup> R. Scheps, D. Florida, S. A. Rice, *J. Chem. Phys.*, **61**, 1730(1974).
- <sup>30</sup> J. L. Knee, P. M. Johnson, *J. Chem. Phys.*, **80**, 13(1984).
- <sup>31</sup> K. Kimura, H. Tsubomura, S. Nagakura, *Bull. Chem. Soc. Jpn.*, **37**, 1336(1964).

- 
- <sup>32</sup> K. Kimura, K. Nagakura, *Mol. Phys.*, **9**, 117(1965).
- <sup>33</sup> A. L. Sobolewski, W. Domcke, *J. Phys. Chem. A.*, **105**, 9275(2001).
- <sup>34</sup> A. L. Sobolewski, W. Domcke, C. Dedonder-Lardeux, C. Jouvet, *C. Phys. Chem. Chem. Phys.*, **4**, 1093(2002).
- <sup>35</sup> T. Ebata, C. Minejima, N. Mikami, *J. Phys. Chem. A.*, **106**, 11074(2002).
- <sup>36</sup> V. A. Lobastov, R. Srinivasan, B. M. Goodson, C. Y. Ruan, J. S. Feenstra, A. H. Zewail, *J. Phys. Chem. A.*, **105**, 11159(2001).
- <sup>37</sup> A. M. Mebel, M. C. Lin, D. Chakraborty, J. Park, S. H. Lin, Y. T. Lee, *J. Chem. Phys.*, **114**, 8421(2001).
- <sup>38</sup> Radloff, W.; Freudenberg, Th.; Ritze, H. H.; Stert, V.; Noack, F.; Hertel, I. V. *Chem. Phys. Lett.*, **261**, 301(1966).



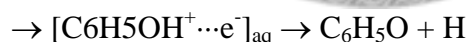
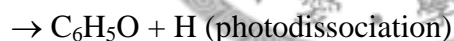
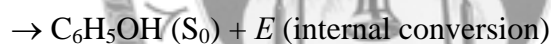
## Chapter 4. The photodissociation of Phenol

### Abstract

The photodissociation of phenol at 193 and 248 nm was studied using multimass ion-imaging techniques. The major dissociation channels at 193 nm include cleavage of the OH bond, elimination of CO, and elimination of H<sub>2</sub>O. Only the former two channels are observed at 248 nm. The translational energy distribution shows that H-atom elimination occurs in both the electronically excited and ground states, but elimination of CO or H<sub>2</sub>O occurs in the electronic ground state.

### Introduction

Because of its antioxidative properties, the photophysics and photochemistry of phenol (C<sub>6</sub>H<sub>5</sub>OH) are of great interest to various fields of science and technology. The following paths of a phenol molecule excited to its first excited singlet state (S<sub>1</sub>) in the condensed phase have been suggested<sup>1,2</sup>



(photoionization in aqueous solution at high pH)

Laser flash photolysis of phenol at 253 nm with detection by both picosecond and nanosecond emission and absorption has been performed to reveal information of the deactivation channels of the first excited singlet state.<sup>1</sup> The fluorescence lifetime on phenol near 295 K was found to be a few nanoseconds. The photodissociation yield of phenol was found to be ~0.1, nearly independent of solvent, but the quantum yield of intersystem crossing varied between 0.2 and 0.3, with smaller values in nonpolar media and larger ones in polar media. No dissociation occurred upon excitation at 266 nm in the condensed phase because the photon energy was insufficient for direct fission of the OH bond.

Most research on gaseous phenol in its S<sub>1</sub> state has been focused on its

spectroscopy. Phenol and various phenol containing clusters have been investigated. For instance, phenol ammonia clusters have been studied extensively by fluorescence and multiphoton ionization.<sup>3,4,5,6,7,8,9,10</sup> Accordingly, this system was considered to be a model system to investigate proton-transfer reactions in the excited state in molecular clusters, but further experiments indicate that, instead of proton transfer on the excited-state surface, transfer of a H atom occurs on the  $S_1$  surface.<sup>11,12,13,14,15</sup> Quantum chemical calculations show that an excited singlet state of  $\pi\sigma^*$  character, being repulsive with respect to stretching of the OH bond, intersects the bound state  $S_1(\pi\sigma^{**})$  near an energy level of 5 eV ( $\sim 248$  nm).<sup>16,17,18</sup> Hydrogen transfer in phenol-ammonia clusters was explained as predissociation of the  $S_1(\pi\sigma^*)$  state via this low-lying  $\pi\sigma^*$  state. The role of a repulsive  $\pi\sigma^*$  state in dissociation is consistent with the large release of translational energy in the channel involving H-atom elimination observed in the photodissociation of phenol in a molecular beam.<sup>19,20</sup>

The excitation of phenol to the  $S_2$  excited state has also been investigated, but varied conclusions have been derived. For phenol in solution, Dellonte et al.<sup>21,22</sup> studied the temperature dependence of internal conversion (IC) from  $S_2$  to  $S_1$ , competing electron-solvation processes, and the cleavage of the OH bond by observing fluorescence quantum yields. A rate coefficient of  $k_{IC} = 3 \times 10^{11} \text{ s}^{-1}$  was determined, and the intersystem crossing (ISC) to a dissociative triplet state with  $k_{ISC} = 7 \times 10^{11} \text{ s}^{-1}$  was suggested. In contrast, time-resolved photoelectron spectra after two-photon ionization showed that the internal conversion from  $S_2$  to  $S_1$  is the dominant pathway, with a time scale in the range of 150-350 fs.<sup>23</sup> It also showed no evidence of competing processes, such as intersystem crossing to a triplet surface, as previously postulated, or an intramolecular vibrational energy redistribution (IVR) process within  $S_2$ . Absorption spectra of the gaseous phenoxyl radical were recorded upon excitation of phenol to the  $S_2$  state at 193 nm.<sup>24</sup> The dissociation was explained in terms of predissociation. Photodissociation of phenol at 193 nm in a condensed phase studied by Fourier-transform electron paramagnetic resonance and transient absorption spectroscopy also produced cleavage of the OH bond.<sup>2</sup>

In this work, we investigated the photodissociation of gaseous phenol at 193 and 248 nm. Distributions of the translational energy of photofragments and of the vibrational and rotational states of CO were measured. We characterized the potential energy hypersurfaces with quantum chemical calculations.

## Experimental

As the experimental techniques have been described in detail,<sup>25,26,27</sup> only a brief description is given here. Phenol vapor was prepared on flowing ultrapure He (or Ne) at a pressure of 400 Torr through a reservoir containing solid phenol at 323 K. The phenol/He mixture was then expanded through a pulsed nozzle (diameter 500  $\mu\text{m}$ ) maintained at 353 K to form a molecular beam. Molecules in that beam were photodissociated with a pulsed UV laser, followed by ionization with a pulsed VUV laser at 118 nm; a pulsed electric field served to extract the ions into a mass spectrometer. At the exit port of the mass spectrometer, a two dimensional ion detector was used to detect the ion positions and intensity distribution. In this two-dimensional detector, one axis pertained to the recoil velocity and the other to the mass.

## Results

### A. Photofragments and Translational Energy Distributions at 193 nm.

Figure 1 depicts the photofragment ion images obtained upon photodissociation of phenol at 193 nm. Fragments with  $m/z = 93, 76, 66, 65, 64,$  and  $63$  were observed; images with  $m/z = 94, 95,$  and  $96$  correspond to phenol and its  $^{13}\text{C}$  isotopes in natural abundance. The power dependence of the photolysis laser in the range of  $0.43\text{-}3.43 \text{ mJ cm}^{-2}$  showed that fragments with  $m/z = 63$  and  $64$  were produced via two photon dissociation, whereas all other fragments were from one photon dissociation. Fragments resulting from multiphoton dissociation are not discussed here.

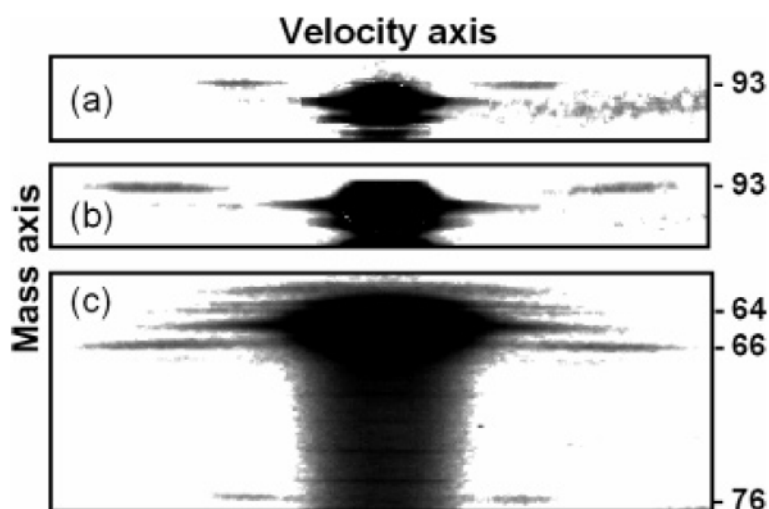


Figure 1. Images of photofragment ions upon photodissociation of phenol at 193 nm.

The delays between pump and probe laser pulses are (a) 49, (b) 81, and (c) 10  $\mu$ s.

The image for  $m/z = 93$  corresponds to the phenoxy radical. The images at two delay intervals between pump and probe laser pulses are shown in Figure 1a and b. As the interval between pump and probe laser pulses was increased, the length of the image increased rapidly. This observation indicates that phenoxy radicals are produced from the dissociation of excited phenol via elimination of a H atom. Both fragments with  $m/z = 76$  and 66, corresponding to elimination of H<sub>2</sub>O and CO molecules, respectively, have images of linear shape.

The image of the fragment with  $m/z = 65$  possesses two components. A linearly shaped component is superimposed on a disk-like component at the center; the latter component resulted from the dissociative ionization of a heavier fragment by VUV photoionization because of the small ionization threshold of this fragment. There are only three possible fragments,  $m/z = 93$ , 76 and 66, which are heavier than  $m/z = 65$ . The fragment with  $m/z = 76$  cannot crack into one with  $m/z = 65$  because the difference of these two masses matches no observed or conceivable masses of atoms or molecules. Because the mass difference is small, fragment cracking from one with  $m/z = 66$  into another with  $m/z = 65$  would have insufficient recoil velocity to produce such a large disk-like image. As a result, the most likely fragment to generate the disk-like image has  $m/z = 93$ ; the image at the center spreading from  $m/z = 93$  to 65 represents the dissociation of an ion with  $m/z = 93$  into another with  $m/z = 65$  during the flight in the mass spectrometer. The translational energy distribution of the H-elimination channel, illustrated in Figure 2a, has taken the disk-like image for  $m/z = 65$  into account. The slow component in the distribution of translational energy in the H-elimination channel results from only the disk-like component for  $m/z = 65$ , but the rapid component in the distribution of translational energy in the H-elimination channel results from ions with both  $m/z = 65$  and 93.

The linearly shaped component with  $m/z = 65$  corresponds to the fragment C<sub>5</sub>H<sub>5</sub>, but its corresponding fragmentation partner HCO was undetected. The translational energy (>30 kcal mol<sup>-1</sup>) obtained from the image is greater than the available energy for the channel to produce C<sub>5</sub>H<sub>5</sub> + CO + H. The most likely explanation is that it results from dissociative ionization of the central image corresponding to an ion with  $m/z = 66$ ; that is, C<sub>5</sub>H<sub>6</sub> with large internal energy. Unlike the disk-like image from other fragments, the image of  $m/z = 65$  is linear because of the large mass ratio between C<sub>5</sub>H<sub>5</sub> and H. We cannot exclude the possibility of a three-body dissociation channel to form C<sub>5</sub>H<sub>5</sub> + CO + H, which has a small translational energy located at the



central part of the linearly shaped image for an ion with  $m/z = 65$ .

The translational energy distributions for photofragments in various channels are shown in Figure 2. Except for the slow component in the H elimination (Figure 2a), all distributions of translational energy show a large release of translational energy. The observed maximum translational energy almost attains the maximum available energy of each channel.

In order to examine the relevance the seven-membered-ring isomeration as we discover in aniline and 4-methylpyridine, the photodissociation of phenol-1- $^{13}\text{C}$  was also studied. For the channel involving elimination of CO, we observed only  $^{13}\text{CO}$  but no  $^{12}\text{CO}$  from phenol-1- $^{13}\text{C}$ . This result indicates that carbon atoms of the aromatic ring do not exchange before dissociation occurs.

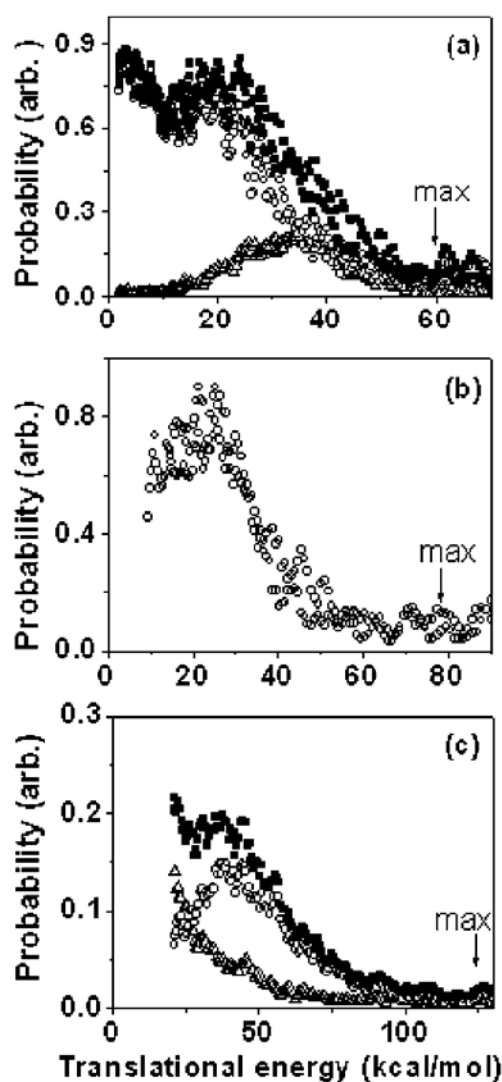


Figure 2. Distributions of translational energy for photofragments from (a)  $\text{C}_6\text{H}_5\text{OH} + h\nu (193 \text{ nm}) \rightarrow \text{C}_6\text{H}_5\text{O} + \text{H}$ . Open triangles show the contribution from ions with  $m/z$

= 93, open circles show the contribution from the disk-like image for ions with  $m/z = 65$ , and solid squares denote the sum of these two, (b)  $\text{C}_6\text{H}_5\text{OH} + h\nu$  (193 nm)  $\rightarrow$   $\text{C}_6\text{H}_4 + \text{H}_2\text{O}$ , and (c)  $\text{C}_6\text{H}_5\text{OH} + h\nu$  (193 nm)  $\rightarrow$   $\text{C}_5\text{H}_6 + \text{CO}$ . Open circles show the contribution from ions with  $m/z = 66$ , open triangles are from the line shape image for ions with  $m/z = 65$ , and solid squares denote the sum of these two. Arrows indicate the maximum available energy.

## B. Photofragments and Translational Energy Distributions at 248 nm.

The images of photofragment ions obtained upon irradiation of phenol at 248 nm are similar to those obtained at 193 nm, as shown in Figure 3. Fragments with  $m/z = 93, 76, 66$ , and  $65$  were observed, but only ions with  $m/z = 93$  and  $66$  and a disk-like component for  $m/z = 65$  were from one-photon dissociation. At this wavelength, elimination of  $\text{H}_2\text{O}$  was unobserved in the one-photon process. The proportion of fragments with  $m/z = 93$  cracking into the disk-like image with  $m/z = 65$  due to dissociative ionization is much smaller than that observed at 193 nm. The distributions of translational energy of these dissociation channels are shown in Figure 4.

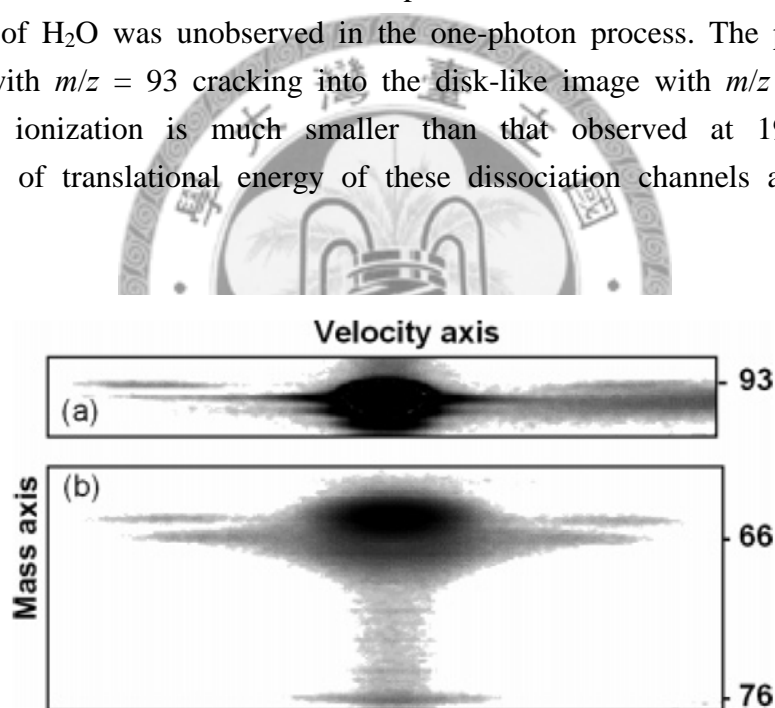


Figure 3. Images of photofragment ions upon the photodissociation of phenol at 248 nm. The delays between pump and probe laser pulses are (a) 95 and (b) 10  $\mu\text{s}$ .

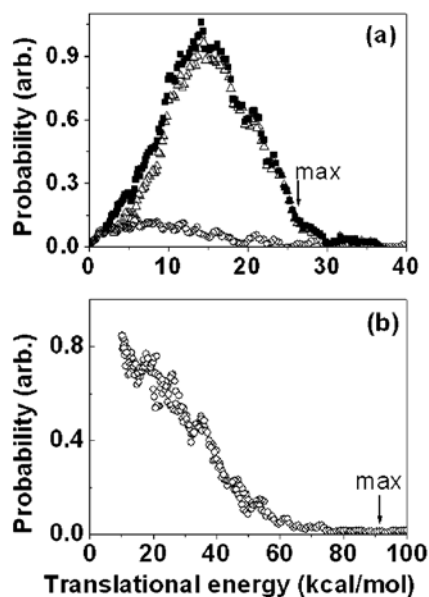
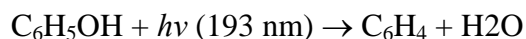
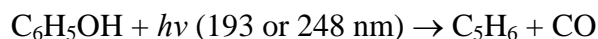
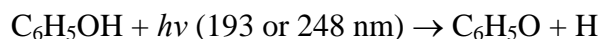


Figure 4. Distribution of translational energy for photofragments from (a)  $\text{C}_6\text{H}_5\text{OH} + h\nu$  (248 nm)  $\rightarrow$   $\text{C}_6\text{H}_5\text{O} + \text{H}$ . Open triangles denote the contribution from ions with  $m/z = 93$ , open circles are from the disk-like image of ions with  $m/z = 65$ , and solid squares denote the sum of these two, (b)  $\text{C}_6\text{H}_5\text{OH} + h\nu$  (248 nm)  $\rightarrow$   $\text{C}_5\text{H}_6 + \text{CO}$ . Arrows indicate the maximum available energy.

## Discussion

### A. Dissociative Channels.

The results of the experiments are describable according to the following reactions



Although a small contribution of the following reaction cannot be positively ruled out experimentally, theoretical calculations suggest that the contribution of this channel is small (see below).



The UV irradiation of phenol at 248 and 193 nm is expected to excite phenol to its  $S_1$  and  $S_2$  (or  $S_3$ ) states, respectively. As these states are stable, dissociation must occur through the coupling of these bound states with a repulsive state or via internal

conversion or intersystem crossing to a lower electronic state, followed by dissociation. For the H-elimination channel, previous quantum chemical calculations show that an excited singlet state of  $\pi\sigma^*$  character, which is repulsive with respect to the stretching of the OH bond, intersects both the  $S_1$  and  $S_2$  states.<sup>16-18</sup> H elimination at 248 nm was interpreted as involving predissociation via this repulsive state.<sup>19</sup> H elimination upon excitation at 193 nm might also be interpreted as a dissociation via the  $\pi\sigma^*$  state through a coupling between  $S_2$  and  $\pi\sigma^*$  or through a coupling between  $S_1$  and  $\pi\sigma^*$  after internal conversion from  $S_2$  to  $S_1$ . The fast component in the distribution of translational energy observed in the H-elimination channel must correspond to dissociation via this repulsive  $\pi\sigma^*$  state. Although dissociation through the triplet state has been suggested<sup>21,22</sup> and the triplet potential energy surface correlating to dissociation products  $H + C_6H_5O$  might have an exit barrier leading to a large translational energy release,<sup>28,29</sup> the dependence of the quantum yield on intersystem crossing and the independence of the quantum yield on dissociation on solvents indicate that dissociation of phenol in solution does not occur in the triplet state.<sup>1</sup> Furthermore, from studies of photodissociation of phenol at 193 nm in a condensed phase with Fourier-transform electron paramagnetic resonance and transient absorption spectra, the results indicate that the triplet state is not involved in the dissociative process.<sup>2</sup>

The slow component in the translational energy distribution of the H-elimination channel must correspond to dissociation from the ground state. The proportion of the slow component that increases as the excitation varies from 248 to 193 nm indicates the importance of H elimination from the electronic ground state at shorter UV wavelengths. Perhaps the rate of internal conversion to the ground state becomes very large at a short UV wavelength. The analogous phenomena with a large yield of internal conversion to the ground state upon excitation at 193 nm, in contrast to the large yield of internal conversion and/or intersystem crossing to the other electronic excited state upon excitation at 248 nm, have been observed in similar systems such as ethylbenzene and propylbenzene.<sup>28,29</sup>

The mechanisms for dissociation into CO and  $H_2O$  differ from that for elimination of a H atom. The average translational energies in the CO-elimination and  $H_2O$ -elimination channels are large. The observed maximum translational energy nearly attains the maximum available energy for both channels. The difference between the observed maximum translational energy and the maximum available energy is smaller than the energies of the electronically excited states of these fragments. As a result, fragments of both channels,  $C_5H_6 + CO$  and  $C_6H_4 + H_2O$ , were produced in their electronic ground states. As the ground state of these closed-shell

fragments correlates only with the ground state of the parent molecule, the dissociation must occur on the ground electronic surface.

## B. Potential surface and reaction pathway

The following calculation in this paragraph was performed by Pro. M. C. Lin's group. The vertical excitation energies of phenol for the singlet and triplet states was calculated with time dependent density functional theory (TD-B3LYP) using Gaussian 03 and complete active space second-order perturbation theory (CASPT2) using MOLPRO with the 6-311G(d,p) basis set, as shown in the figure 7. Eight active orbitals and eight active electrons were specified in the CASPT2 calculation. According to Figure 7, we predict that light at 248 nm is able to excite a phenol molecule from the ground state to the first excited state  $S_1$  for the isomerization and decomposition reactions to proceed. Apparently because of the spin-forbidden nature of the transition from  $S_0$  to  $T_1$ , the reaction seems not to occur in the triplet excited state, despite the energies of the first three triplet states being less than those of photons corresponding to laser lines at 248 or 193 nm.

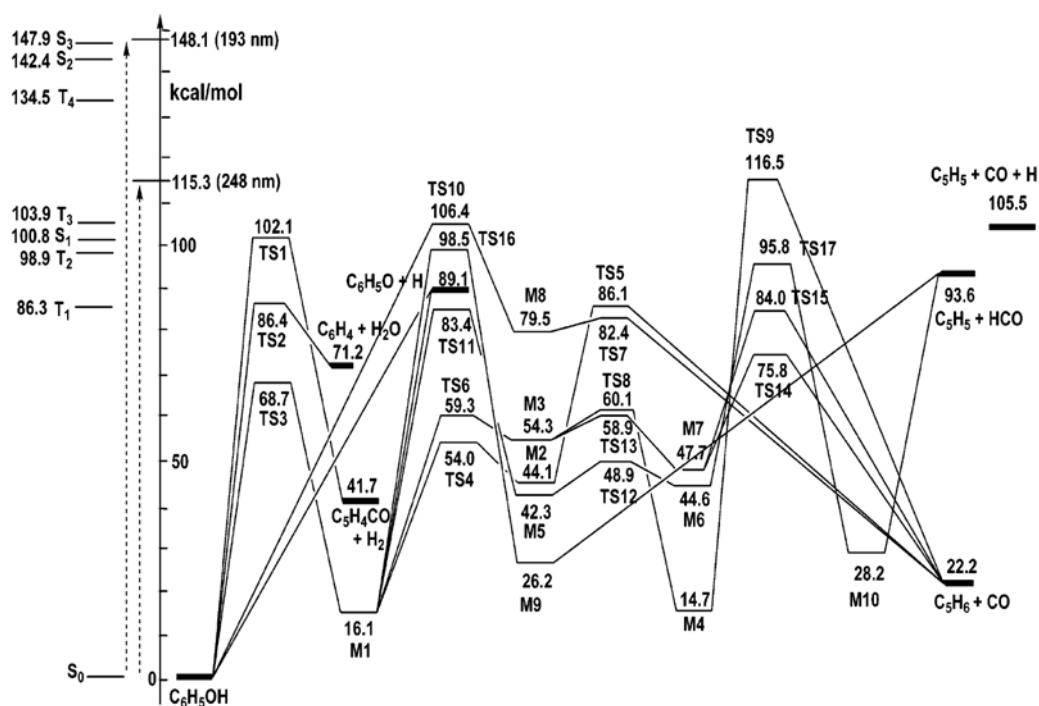
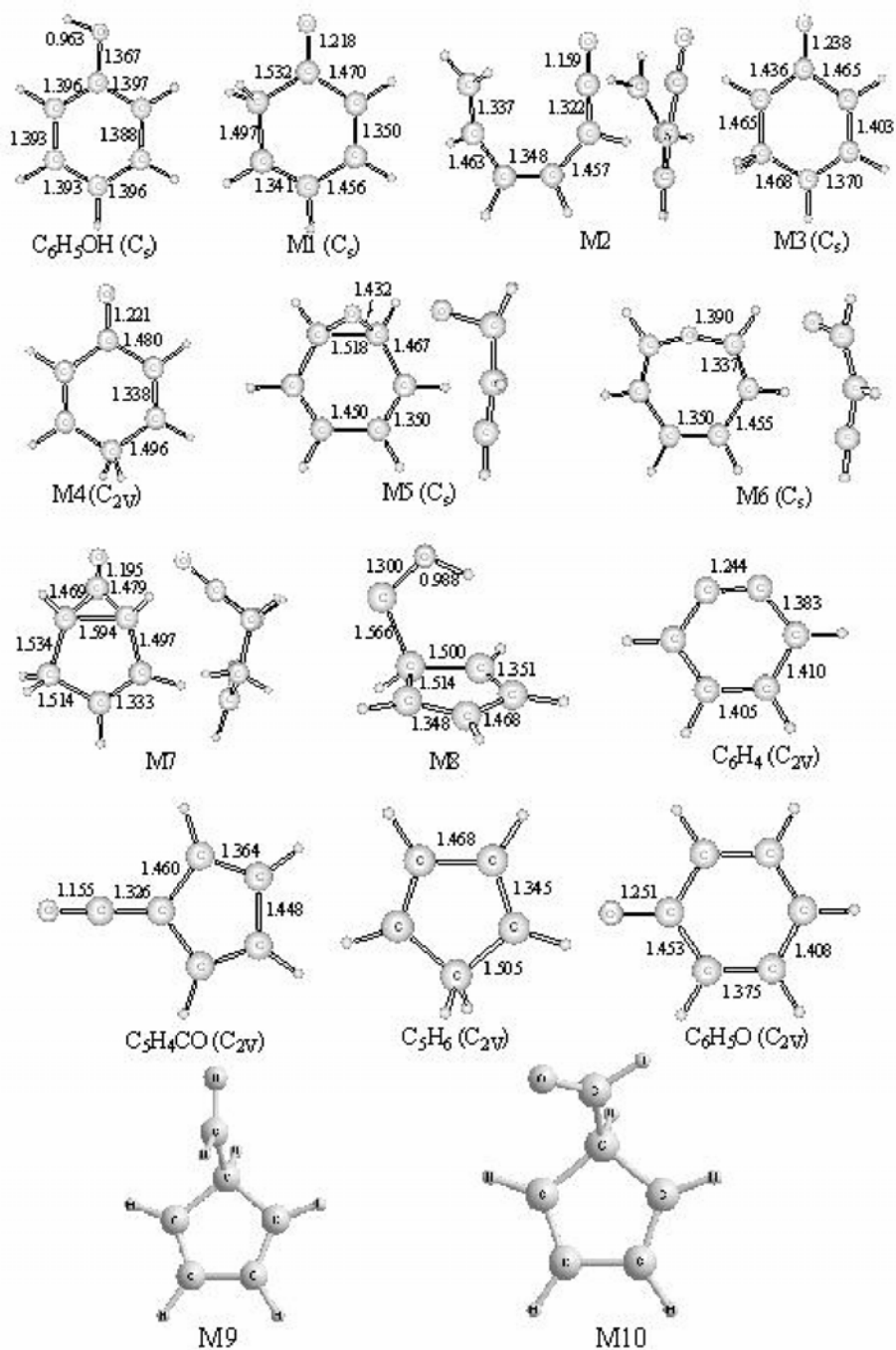


Figure 7. Schematic diagram of the energy for isomerization and dissociation reactions of  $C_6H_5OH$  at the G2M//B3LYP/6-311G(d,p) level of theory and the excited energy levels of  $C_6H_5OH$  at the CASPT2 level of theory.

Various dissociation channels of phenol in its ground electronic surface have

already been calculated with the G2M// B3LYP/6-311G(d,p) method. Figure 7 shows a simplified potential energy diagram for these channels. The structures of intermediates (M1-M10) and transition states (TS1-TS17) have shown in the Figure 8.



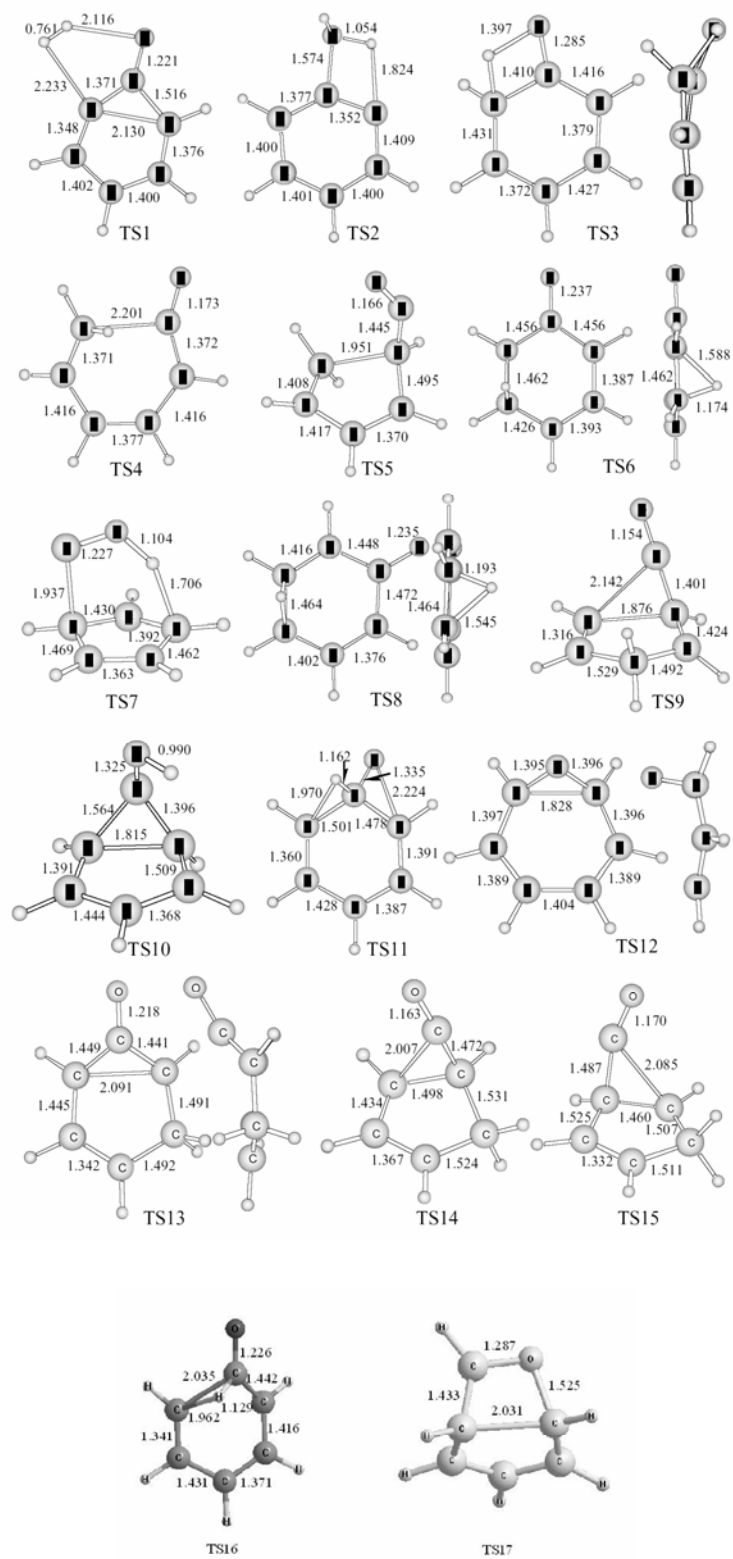
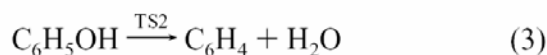
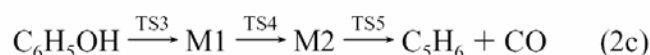
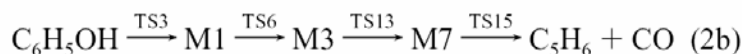
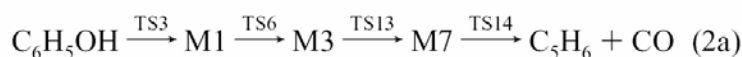
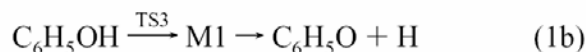
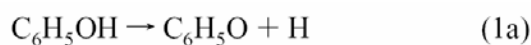


Figure 8. Geometries of the intermediates and transition states optimized at the B3LYP/6-311G\*\* level of theory

If we neglect contributions of the channels via transition states TS<sub>1</sub>, TS<sub>9</sub>, TS<sub>10</sub>, TS<sub>16</sub>, and TS<sub>17</sub> due to their higher barriers, the accessible paths are describable as follows



Direct dissociation of phenol to form C<sub>6</sub>H<sub>5</sub>O + H, reaction 1a, requires 89.1 kcal mol<sup>-1</sup>. The H atom might migrate from the OH group to form *ortho*-cyclohexadienone (M1), followed by H elimination, reaction 1b. The CO elimination might proceed via several dissociative pathways; the most feasible pathway, reaction 2a, begins with migration of the H atom from the OH group to form M1, followed by further H-atom migration along the six-membered ring to form *meta*-cyclohexadienone (M3); M3 then isomerizes to a bicyclic isomer (M7) before decomposition into *cyclo*-C<sub>5</sub>H<sub>6</sub> + CO via TS<sub>14</sub>. Although this path includes three intermediates and four transition states, the largest barrier height is only 75.8 kcal mol<sup>-1</sup>. Reaction 2b proceeds similarly to reaction 2a except for the last step, in which M7 decomposes via TS<sub>15</sub> with a barrier height of 84.0 kcal mol<sup>-1</sup>. The third channel, reaction 2c, has a barrier height of 86.1 kcal mol<sup>-1</sup>. In principle, CO can also be produced from fragmentation of the internally excited C<sub>6</sub>H<sub>5</sub>O formed in reactions 1a and 1b. The theoretical barrier for the fragmentation of C<sub>6</sub>H<sub>5</sub>O to give C<sub>5</sub>H<sub>5</sub> + CO has been computed at the G2M level of theory to be 52 kcal mol<sup>-1</sup> with a very tight transition state. The total barrier for the formation of C<sub>5</sub>H<sub>5</sub> + H + CO is 141 kcal mol<sup>-1</sup>, which is almost twice that of TS<sub>14</sub>. Accordingly, the contribution of this route to CO should be negligible. The channel to eliminate H<sub>2</sub>O, reaction 3, proceeds via the four-center elimination via TS<sub>2</sub> with a barrier height of 86.4 kcal mol<sup>-1</sup>. Elimination of HCO is predicted to occur through TS<sub>16</sub> and M9 from M1 and through TS<sub>17</sub> and M10 from M6. The barriers for these two channels are 98.5 and 95.8 kcal mol<sup>-1</sup>, respectively, which are greater than that of the CO elimination pathway by about 20 kcal mol<sup>-1</sup>. In the isomerization and decomposition from M1, elimination of CO is hence most favorable. Although phenol can isomerize to a seven-membered ring



isomer (M6) with a barrier of only 83.4 kcal mol<sup>-1</sup>, our experiment on phenol-1-<sup>13</sup>C shows that this isomerization is unimportant in CO elimination under our experimental conditions.

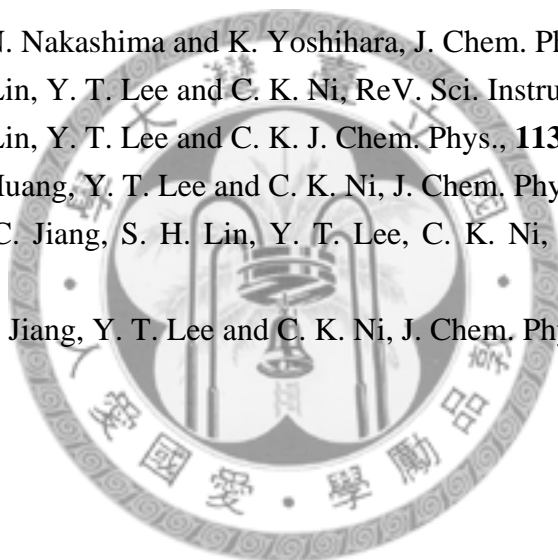
## Conclusions

The major dissociation channels for phenol at 193 nm include OH bond fission, CO elimination, and H<sub>2</sub>O elimination. Only the former two channels are observed at 248 nm. The translational energy distribution indicates that H-atom elimination occurs in both the electronically excited and the ground states, but elimination of CO or H<sub>2</sub>O occurs in the electronic ground state. Although phenol can isomerize to a seven-membered ring prior to dissociation in the ground, the experimental data reveals that this isomerization is unimportant in CO elimination. This character is different from the toluene, aniline and 4-methyl-pyridine described in chapter 4.

## References

- <sup>1</sup> R.Hermann, G. R. Mahalaxmi, T. Jochum, S. Naumov and O. Brede, *J. Phys. Chem. A*, **106**, 2379(2002)
- <sup>2</sup> A. Bussandri and H. Willigen, *J. Phys. Chem. A*, **106**, 1524(2002).
- <sup>3</sup> C. Solgadi, D. Jouvét and A. A. Tramer, *J. Phys. Chem.*, **92**, 3313(1988).
- <sup>4</sup> C. Jouvét, C. Dedonder-Lardeux, M. Richard-Viard, D. Solgadi and A. Tramer, *J. Phys. Chem.*, **94**, 5041(1990).
- <sup>5</sup> J. Steadman and J. A. Syage, *J. Phys. Chem.*, **92**, 4630(1990).
- <sup>6</sup> J. A. Syage and J. Steadman, *J. Chem. Phys.*, **95**, 2497(1991).
- <sup>7</sup> J. Steadman and J. A. Syage, *J. Am. Chem. Soc.*, **113**, 6786(1991).
- <sup>8</sup> J. A. Syage and J. Steadman, *J. Phys. Chem.*, **96**, 9606(1992).
- <sup>9</sup> J. A. Syage, *Chem. Phys. Lett.*, **202**, 227(1993).
- <sup>10</sup> M. F. Hineman, D. F. Kelley and E. R. Bernstein, *J. Chem. Phys.*, **99**, 4533(1993).
- <sup>11</sup> C. Jacoby, P. Hering, M. Schmitt, W. Roth and K. Kleinermanns, *Chem. Phys.*, **23**, 239(1998).
- <sup>12</sup> G. Pino, G. Grégoire, C. Dedonder-Lardeux, C. Jouvét, S. Martrenchard, D. Solgadi, *J. Chem. Phys.*, **111**, 10747(1999).
- <sup>13</sup> G. Pino, G. Grégoire, C. Dedonder-Lardeux, C. Jouvét, S. Martrenchard and D. Solgadi, *Phys. Chem. Chem. Phys.*, **2**, 893(2000).
- <sup>14</sup> S. Ishiuchi, M. Saeki and M. Fujii, *Chem. Phys. Lett.*, **322**, 27(2000).
- <sup>15</sup> S. Ishiuchi, M. Saeki, K. Daigoku, T. Ueda, T. Yamanaka, K. Hashimoto and M

- 
- Fujii, Chem. Phys. Lett., **347**, 87(2001).
- <sup>16</sup> A. L. Sobolewski and W. Domcke, J. Phys. Chem. A, **105**, 9275(2001).
- <sup>17</sup> A. L. Sobolewski, W. Domcke, C. Dedonder-Lardeux and C. Jouvet, Phys. Chem. Chem. Phys., **4**, 1093(2002).
- <sup>18</sup> K. Daigoku, S. Ishiuchi, M. Sakai, M. Fujii and K. Hashimoto J. Chem. Phys., **119**, 5149(2003).
- <sup>19</sup> C. M. Tseng, Y. T. Lee and C. K. Ni, J. Chem. Phys., **121**, 2459(2004).
- <sup>20</sup> M. G. D. Nix, A. L. Devine, B. Cronin, R. N. Dixon and M. N. R. Ashfold, J. Chem. Phys., **125**, 133318(2006).
- <sup>21</sup> S. Dellonte and G. Marconi, J. Photochem., **30**, 37(1985).
- <sup>22</sup> S. Dellonte, G. Marconi and S. Monti, J. Photochem., **39**, 33(1987).
- <sup>23</sup> C. P. Schick, S. D. Carpenter and P. M. Weber, J. Phys. Chem. A, **103**, 10470(1999).
- <sup>24</sup> Y. Kaji, K. Obi, N. Nakashima and K. Yoshihara, J. Chem. Phys., **87**, 5059(1987).
- <sup>25</sup> S. T. Tsai, C. K. Lin, Y. T. Lee and C. K. Ni, Rev. Sci. Instrum., **72**, 1963(2001).
- <sup>26</sup> S. T. Tsai, C. K. Lin, Y. T. Lee and C. K. Ni, J. Chem. Phys., **113**, 67(2000).
- <sup>27</sup> S. T. Tsai, C. L. Huang, Y. T. Lee and C. K. Ni, J. Chem. Phys., **115**, 2449(2001).
- <sup>28</sup> C. L. Huang, J. C. Jiang, S. H. Lin, Y. T. Lee, C. K. Ni, J. Chem. Phys., **116**, 7779(2002).
- <sup>29</sup> C. L. Huang, J. C. Jiang, Y. T. Lee and C. K. Ni, J. Chem. Phys., **117**, 7034(2002).



## Chapter 5. The experimental evidence of $\pi\sigma^*$ repulsive state in phenol and 1-naphthol

### Abstract

The photodissociation of phenol and 1-naphthol at 193 and 248nm was studied using multimass ion imaging techniques under collisionless conditions. Only one dissociation channel was observed, i.e. H atom elimination. The translational energy distributions show two components at both wavelengths. The slow component corresponds to the dissociation from the ground electronic state after internal conversion, and the fast component results from the dissociation on the electronic excited state. Comparison with the photodissociation of phenol was made.

### Introduction

The excited state proton transfer (ESPT) in clusters has been studied extensively by various kinds of techniques. These methods include the frequency-domain studies by nanosecond lasers and time-domains studies by sub-picosecond lasers<sup>1,2,3,4,5,6,7,8</sup>. By detecting the light emission or ion/electron signal with respect to the wavelength or the pump-probe delay time, the behavior of molecules immersed in solvent molecules can be elucidated in detail. In the last several decades there is a tremendous wave of interest in this topic. A dynamic model has been established to explain the data. It is the proton transfer on the excited potential. Phenol-ammonia clusters are one of the important systems of ESPT. The potential diagram is shown in the figure 1.

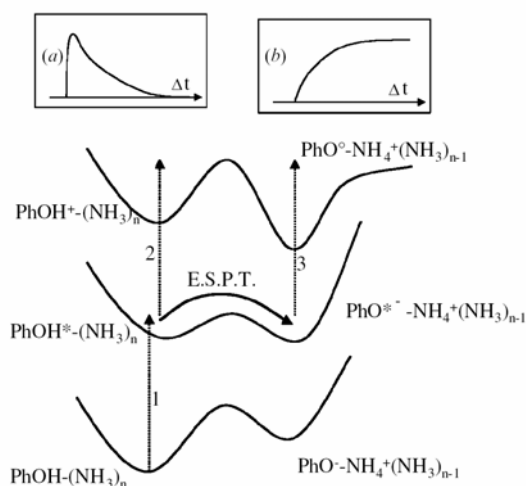


Figure 1. The schematic potential diagram of a PhO-(NH<sub>3</sub>)<sub>n</sub> cluster (e.g. *n* = 5). Arrow 1 represents the pump laser; excited clusters can be ionized before ESPT (arrow 2) to the non-proton-transferred part of the ionic potential, or after ESPT (arrow 3) to the proton-transferred part of the ionic potential. The ionic state has a high barrier between non-proton-transferred and proton-transferred structures to explain the observation of picosecond decays of the {PhOH-(NH<sub>3</sub>)<sub>n</sub>}<sup>+</sup> mass peaks and the rise times of the NH<sub>4</sub><sup>+</sup>(NH<sub>3</sub>)<sub>n-1</sub> mass peaks. Adapt from ref.9

According to Steadman and Syage<sup>3,4,5,6,7,8</sup>, the picosecond experiments can be understood with the following scheme. First of all, at time *t* = 0 the neutral cluster PhOH-(NH<sub>3</sub>)<sub>n</sub> in the ground state is excited to the electronic excited state by an UV photon (see Figure 1, arrow 1). After the excitation, the major process is the proton transfer from the excited PhOH\*(S1) to (NH<sub>3</sub>)<sub>n</sub> on a timescale of 60±70 ps. This process is detected by ionizing the excited PhOH\*-(NH<sub>3</sub>)<sub>n</sub> cluster with additional UV photon. Due to the ESPT process, the parent ion signal PhOH<sup>+</sup>(NH<sub>3</sub>)<sub>n</sub> will decay with respect to the pump-probe delay time (see Figure 1, arrow 2). It means that the population of the initially excited state is moving to the proton-transfer state (see Figure 1, arrow E.S.P.T.). Correspondently, the population of, PhO\*<sup>-</sup>-NH<sub>4</sub><sup>+</sup>(NH<sub>3</sub>)<sub>n-1</sub> which is generated from PhOH\*-(NH<sub>3</sub>)<sub>n</sub> through ESPT process, will increase as time goes by. The ionization from this proton-transfer state, PhOH\*-(NH<sub>3</sub>)<sub>n</sub>, to ionic state is dissociative. In the other words, once the ionization take place after ESPT (see Figure 1, arrow 3), it occurs on the PhO<sup>o</sup>-NH<sub>4</sub><sup>+</sup>(NH<sub>3</sub>)<sub>n-1</sub> part of ionic surface. Then the fragmentation PhO<sup>o</sup> + NH<sub>4</sub><sup>+</sup>(NH<sub>3</sub>)<sub>n-1</sub> occurs and only the NH<sub>4</sub><sup>+</sup>(NH<sub>3</sub>)<sub>n-1</sub> fragment ions are detected.

Consequently, the explanation has been made to account for the decay of {PhOH-(NH<sub>3</sub>)<sub>n</sub>}<sup>+</sup> parent ions, as shown in Figure 1(a), as well as the rising of NH<sub>4</sub><sup>+</sup>(NH<sub>3</sub>)<sub>n-1</sub> fragment ions, as illustrated in Figure 1(b).

The interpretation is self-consistent expect that the following assumptions have to be made. First, it needs to have a significant barrier in the ionic state between the excitation of non-proton-transferred and the proton-transferred forms has to be existed. This is necessary to ensure the selectivity of the ionization processes from the PhOH\*-(NH<sub>3</sub>)<sub>n</sub> state or PhO\*<sup>-</sup>-NH<sub>4</sub><sup>+</sup>(NH<sub>3</sub>)<sub>n-1</sub> state to the corresponding ionic states. Second, evaporation of the clusters after absorbing the UV photons should be less significant to prevent the contamination of the monitoring parent ion or fragment ion from the larger clusters. Usually, the evaporation process is not easy to avoid with simple means and the careful interpretation of experimental data should be considered. Nevertheless, these results show a successful marriage between the laser techniques

and molecular beam methods.

Recently, Jacoby and co-workers have shown that the REMPI spectra of  $\text{PhOH}-(\text{NH}_3)_3$  and  $\text{PhOH}-(\text{NH}_3)_4$  show well resolved vibronic structure when the  $(\text{NH}_3)_n\text{H}^+$  mass peaks are monitored, while excitation spectra of  $\text{PhOH}-(\text{NH}_3)_{n-1}$  mass peaks are structureless.<sup>10</sup> Pino *et al.* have reported that the  $(\text{NH}_3)_3\text{H}^+$  mass peaks can be observed even if the ionization laser delay is 200 ns from the ultraviolet laser for excitation to the  $S_1$  state.<sup>11,12</sup> The result indicates the product,  $(\text{NH}_3)_3\text{H}^+$ , is generated from the ionization of a long lived neutral species. Instead of the excited state proton transfer, these experimental data were interpreted as the H atom transfer in the  $S_1$  state. This hydrogen transfer mechanism is also supported by the infrared dip spectroscopy<sup>13</sup> and time-resolved infrared spectra<sup>14</sup> of the photochemical reaction products of phenol–ammonia cluster. Although the model of proton transfer in the excited state has been used to account for the transient signal that has been observed by ultra-fast laser techniques, the evidence of the detection of neutral  $\text{H}(\text{NH}_3)_n$  shift this paradigm to a new one.

*Ab initio* calculations have been performed for the electronic ground and the excited singlet states of phenol and the complexes of phenol with ammonia.<sup>15,16,17</sup> An excited singlet state of  $\pi\sigma^*$  character, which is repulsive with respect to the stretching of OH bond was found. The  $\pi\sigma^*$  potential energy function intersects the bound potential energy function of  $S_1(\pi\pi^*)$ . Hydrogen transfer reaction in the phenol–ammonia clusters was explained as the predissociation of the  $S_1(\pi\pi^*)$  state by this low lying  $\pi\sigma^*$  state.

Except for these calculations, the first experimental observation of the phenol  $\pi\sigma^*$  potential energy functions was reported by our group.<sup>18</sup> In this work, photodissociation of phenol at 248 nm<sup>18</sup> and 193 nm<sup>19</sup> was studied. Direct evidence of the H atom elimination from this repulsive potential surface was demonstrated.

In addition to the phenol–ammonia clusters, 1-naphthol–ammonia clusters have also been proposed as another model system of photo-induced ESPT<sup>20</sup>. The major features of the experiments on 1-naphthol-( $\text{NH}_3$ )<sub>n</sub> that have led to the suggestion that the ESPT mechanism is involved in these clusters include (1) the strong red-shifted emission from clusters larger than n=4. This red-shifted emission is similar to the ESPT in solution; (2) the similarity between fluorescence excitation spectrum of 1-naphthol and two photon excitation/ionization spectrum of 1-naphthol-( $\text{NH}_3$ )<sub>4</sub>; (3) a 60 ps decay observed only for cluster sizes n = 3 and 4; and (4) no sign of red-shifted emission observed when weaker bases such as methanol were used as solvents in the clusters. However, these experimental features are considered not to be good evidence to support the ESPT in 1-naphthol-( $\text{NH}_3$ )<sub>n</sub> clusters [25]. On the other hand, no long-

lived neutral species  $(\text{NH}_3)_n\text{H}$  has been observed from photoexcitation of 1-naphthol- $(\text{NH}_3)_n$ . The question arises as to whether the hydrogen transfer or proton transfer is present or not in 1-naphthol- $(\text{NH}_3)_n$  clusters. In this work, photodissociation dynamics of 1-naphthol was investigated. Experimental evidence for the H atom elimination from the repulsive excited state is given.

## Experimental

The experimental techniques have been described in chapter two and only a brief description is given here. Phenol vapor was prepared on flowing ultrapure He (or Ne) at a pressure of 400 Torr through a reservoir containing solid phenol at 323 K. The phenol/He mixture was then expanded through a pulsed nozzle (diameter 500  $\mu\text{m}$ ) maintained at 353 K to form a molecular beam. 1-naphthol vapour was formed by flowing ultrapure Ne at pressures of 600 Torr through a reservoir filled with sample at 373 K. The sample/Ne mixture was then expanded through an 800  $\mu\text{m}$  high temperature (383 K) pulsed nozzle to form the molecular beam. Molecules in that beam were photodissociated with a pulsed UV laser, followed by ionization with a pulsed VUV laser at 118 nm; a pulsed electric field served to extract the ions into a mass spectrometer. At the exit port of the mass spectrometer, a two dimensional ion detector was used to detect the ion positions and intensity distribution.

## Results

### I. The photodissociation of phenol at 248 nm and 193 nm

#### A. Photofragments and Translational Energy Distribution at 248 nm

Fragment ion of  $m/e = 93$  ( $\text{C}_6\text{H}_5\text{O}^+$ ) with large intensity was observed from the photodissociation of phenol at 248 nm. It corresponds to the H atom elimination. The images of  $m/e = 93$  obtained at various delay times between pump and probe laser pulses are shown in Figs. 2(a), 2(b) and 2(c).

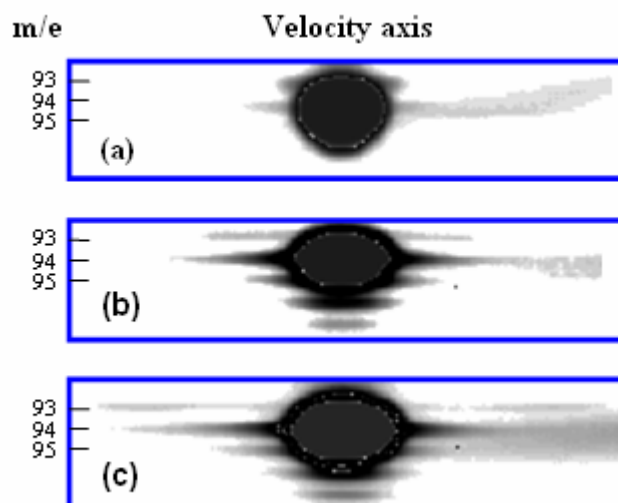


Fig 2. Images of fragment ion  $m/e = 93$  at delay time (a)  $13 \mu\text{s}$  (b)  $53 \mu\text{s}$  and (c)  $95 \mu\text{s}$ . Images of parent ion  $m/e = 94$  as well as the  $^{13}\text{C}$  parent ions were also shown.

As the delay time between pump and probe laser pulses increased, the length of the  $m/e = 93$  image increased rapidly. This corresponds to the  $\text{C}_6\text{H}_5\text{O}$  fragment with large recoil velocity. The photofragment translational energy distribution obtained from the image is shown in Fig. 3.

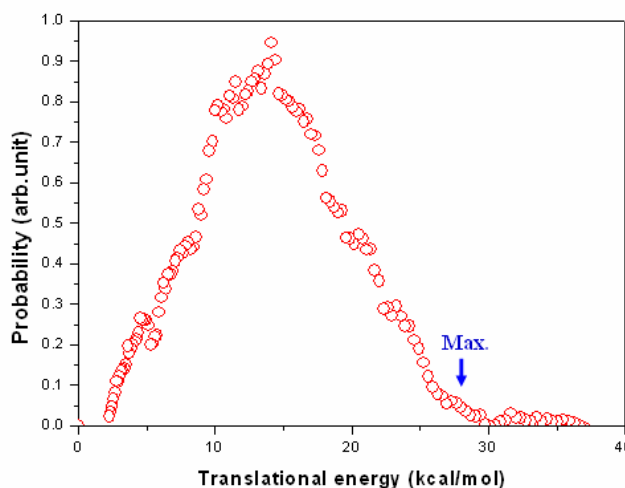


Fig. 3. Total translational energy distribution of reaction  $\text{C}_6\text{H}_5\text{OH} + h\nu (248 \text{ nm}) \rightarrow \text{C}_6\text{H}_5\text{O} + \text{H}$ . Arrow indicates the maximum available energy.

It shows that the average released translational energy is large, and the peak of

the distribution is located at 15 kcal/mol. It is interesting to note that the maximum translational energy reaches the maximum available energy of the reaction  $C_6H_5OH + h\nu$  (248 nm)  $\rightarrow C_6H_5O + H$ . In addition to  $m/e = 93$ , fragment ions of  $m/e = 76$ , 66, and 65 with small intensities were also observed. However, these signals are very small and they are not related to the H atom elimination. The detail description of these fragments was described in chapter 4.

## B. Photofragments and Translational Energy Distribution at 193 nm

Figure 4 depicts the photofragment ion images obtained upon photodissociation of phenol at 193 nm. The image for  $m/e = 93$  corresponds to the phenoxy radical. The images at two delay intervals between pump and probe laser pulses are shown in Figure 4a and 4b. As the interval between pump and probe laser pulses was increased, the length of the image increased rapidly. This observation indicates that phenoxy radicals are produced from the dissociation of excited phenol via elimination of a H atom.

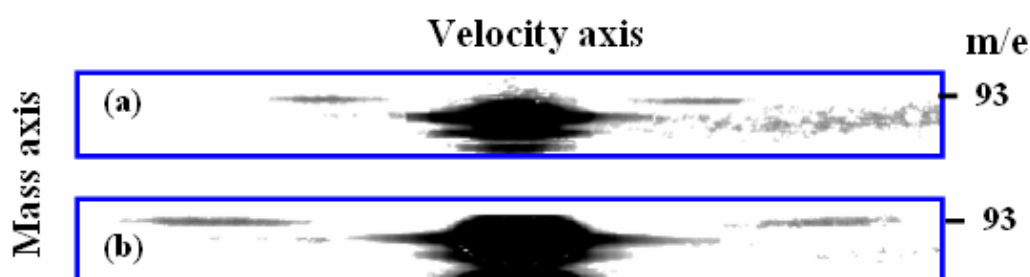


Fig. 4. Images of photofragment ions upon photodissociation of phenol at 193 nm. The delays between pump and probe laser pulses are (a) 49, and (b) 81  $\mu$ s.

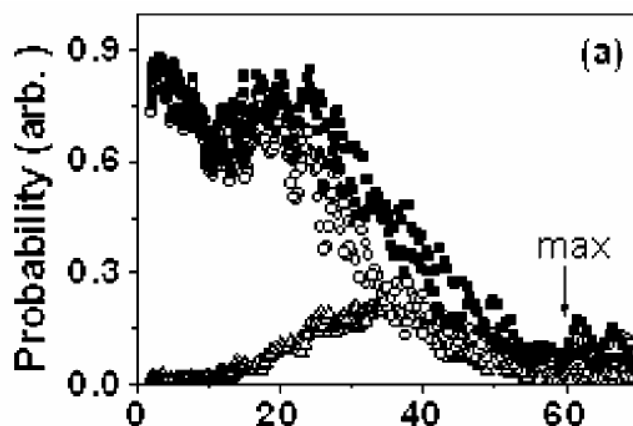




Figure 5. Distributions of translational energy for photofragments from  $C_6H_5OH + h\nu$  (193 nm)  $\rightarrow C_6H_5O + H$ . Open triangles show the contribution from ions with  $m/z = 93$ , open circles show the contribution from the disk-like image for ions with  $m/z = 65$ , and solid squares denote the sum of these two.

### C. Discussions

UV absorption of phenol at 248 nm corresponds to the excitation of the  $S_1$  state and 193 nm corresponds to the excitation of the  $S_2$  state. Since  $S_1$  and  $S_2$  are stable states, dissociation must occur through the coupling of this bound state with a repulsive state, or after the internal conversion or intersystem crossing to a lower electronic state.  $\pi \sigma^*$  is a repulsive state and  $S_0$ ,  $T_1$ , and  $T_2$  are the electronic states which have energies lower than that of  $S_1$ . Dissociation must occur on one of these states. The large translational energy release in the H atom elimination channel indicates that the dissociation must occur from an excited state of repulsive potential, or from an electronic state with a large exit barrier. This eliminates the dissociation probability on the  $S_0$  state. The potential energy surface of the triplet state that correlates to the dissociation products of two radicals in the ground state may have an exit barrier and the released translational energy can be large.<sup>21,22</sup> Therefore, it is possible that the large translational energy release results from the triplet state dissociation after intersystem crossing. However, photodissociation of phenol at 193 and 253 nm in the condensed phase studied by Fourier transform electron paramagnetic resonance and transient absorption spectroscopy shows that triplet state is not involved in the dissociation process.<sup>23,24</sup>

Recent *ab initio* calculation shows that the  $\pi \sigma^*$  state, which has repulsive potential-energy functions with respect to the stretching of OH bond, intersects not only the bound potential energy functions of the  $S_1(\pi \pi^*)$  excited state, but also that of the electronic ground state.<sup>15,16</sup> The minimum of the  $S_1(\pi \pi^*)$  state is located at 4.5 eV above  $S_0$ ,<sup>25</sup> and the  $\pi \pi^* - \pi \sigma^*$  conical intersection is at  $\sim 5$  eV. The internal conversion from  $S_1$  to  $S_0$  and intersystem crossing from  $S_1$  to  $T_1$  are the dominant decay channels for the phenol molecules after the excitation by 4.5 eV photons.<sup>26</sup> However, as the excitation photon energy increases to more than 5 eV, the  $\pi \pi^* - \pi \sigma^*$  conical intersection must greatly enhance the predissociation of the optical excited  $\pi \pi^*$  state by the optically dark  $\pi \sigma^*$  state, resulting in the H atom elimination on the repulsive  $\pi \sigma^*$  state. The conical intersection between  $\pi \sigma^*$  and  $S_0$  provides the other population transfer from  $\pi \sigma^*$  to  $S_0$  and the dissociation products are produced in the electronic ground state. The observation of large

translational energy release in our experimental measurement indicates that H atom elimination must be a dissociation process on the repulsive  $\pi \sigma^*$  surface. It provides a direct evidence of the  $\pi \pi^* - \pi \sigma^*$  predissociation mechanism of phenol at 248 nm. Similar argument can be made for the photodissociation of phenol at 193 nm.

## II The photodissociation of 1-naphthol at 248 nm and 193 nm

As we mention in the introduction, another model system of ESPT which has been studied during past decays is 1-naphthol clusters. In contrast to phenol case, little is known about the existence of the repulsive  $\pi \sigma^*$  surface of 1-naphthol. 1-naphthol-amonia clusters excited by femtosecond laser to the  $S_1$  state which is located at 3.86 eV ( $\sim 321$  nm in wavelength) has been studied, but the dynamical process of higher electronic states (i.e.  $S_2$  or  $S_3$ ) is still unknown. In the work photochemical processes in the  $S_2$  or  $S_3$  state by exciting at 248 nm ( $\sim 5$  eV) and 193 nm ( $\sim 6.4$  eV) photon excitation respectively were investigated.

### A. Photofragments and Translational Energy Distribution at 193 nm

The ion image of  $m/e = 143$  and  $115$  in the figure 5(a) and (b) was recoded at different UV-VUV pump-probe delay time. The length of ion image of  $m/e = 143$ , which correspond to the H-atom loss channel, changes rapidly as the pump-probe delay become longer. At pump-probe delay time of  $105 \mu s$ , the resolved translational energy distribution shows the bimodal distribution. The relative intensities between the fast and the slow components are about 1:0.81. The average released translational energy of the fast component is large, and the peak of the distribution is located at 45 kcal/mol. It is interesting to note that the maximum translational energy distribution reaches the maximum available energy, which is the photon energy minus bond energy. A disk-shape image at  $m/e = 115$  was observed when pumping by 193 nm and probing by 118 nm laser. The size of disk-shape image of  $m/e = 115$  become longer gradually when the pump-probe delay time is longer, as shown in the figure 6(a) and (b). But the disk-shape image disappeared when using 157 nm laser as a probe. The source of the disk-shape image is from dissociative ionization of hot  $C_{10}H_7O$  fragments by 118 nm photons.

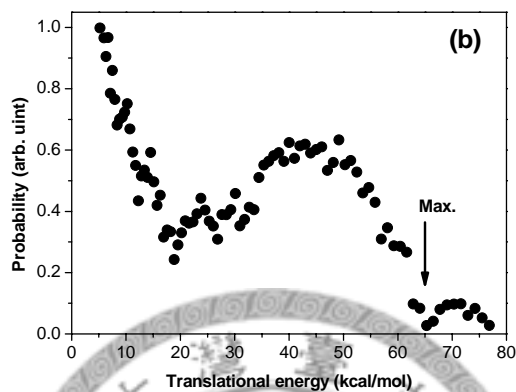
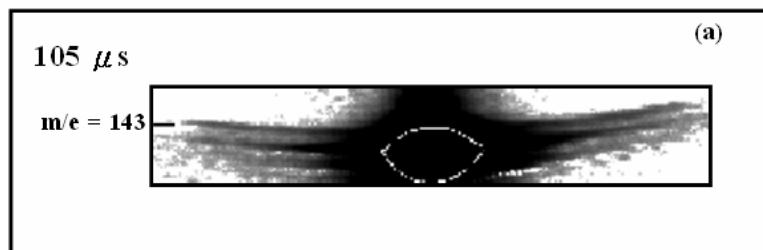


Fig.5(a) The ion image of  $m/e = 143$  at  $105 \mu s$  pump-probe delay time with 193 nm laser excitation. (b) Photofragment translational energy distribution  $C_{10}H_8O + h\nu_{193nm} \rightarrow C_{10}H_7O + H$ .

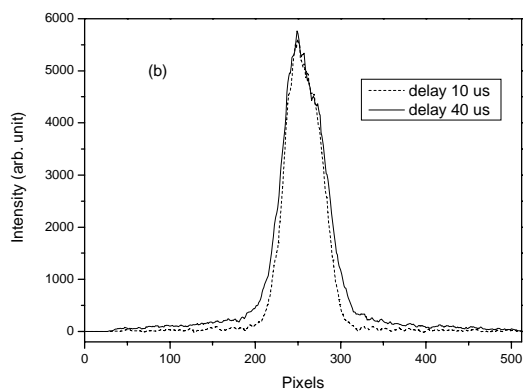
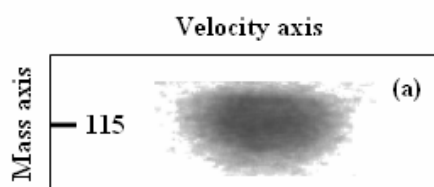
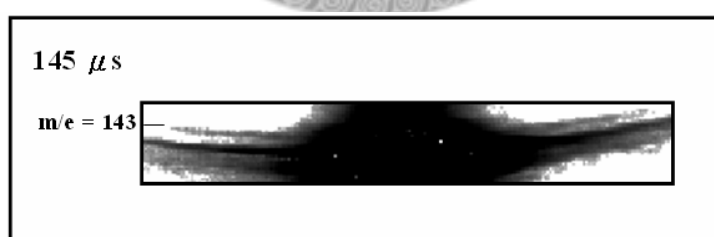


Fig 6. (a) Ion image of  $m/e = 115$ . (b) Image intensity profiles of  $m/e = 115$  at delay time  $10 \mu\text{s}$  (dash line) and  $40 \mu\text{s}$  (solid line). Pump = 193 nm, Probe = 118 nm

## B. Photofragments and Translational Energy Distribution at 248 nm

The ion image of  $m/e = 143$  was obtained at this wavelength as shown in Fig. 7(a). A line shape image indicates the H atom elimination channel of this molecule. Since the photon energy is much smaller at 248 nm, the length of the image at 248 nm is shorter than that at 193 nm. In order to separate the slow component from the interference of parent ion image, the longer delay time at 248 nm was used. Although the experimental delay time between pump and probe laser pulses is as long as  $145 \mu\text{s}$ , the length of the image of  $m/e=143$  is still very short due to the small available energy. The probability of the slow component shown in Fig. 7(b) includes the interference from parent molecules. The slow component was estimated to be  $\sim 60\%$  of the fast component. The peak of the fast component is located at 15 kcal/mol, and the translational energy as much as 30 kcal/mol can be released. It reaches the maximum available energy of the reaction  $\text{C}_{10}\text{H}_8\text{O} + h\nu (248 \text{ nm}) \rightarrow \text{C}_{10}\text{H}_7\text{O} + \text{H}$ . The distribution of the fast component indicates that it results from the electronically excited state. No disk shape image was observed by 248 nm laser pumping and 118 nm or 157 nm as a probe. The reason is that the fragments of  $m/e = 143$  do not have sufficient internal energy to cracking after the ionization.

For both wavelengths H atom loss is the only dissociation channel that we observed.



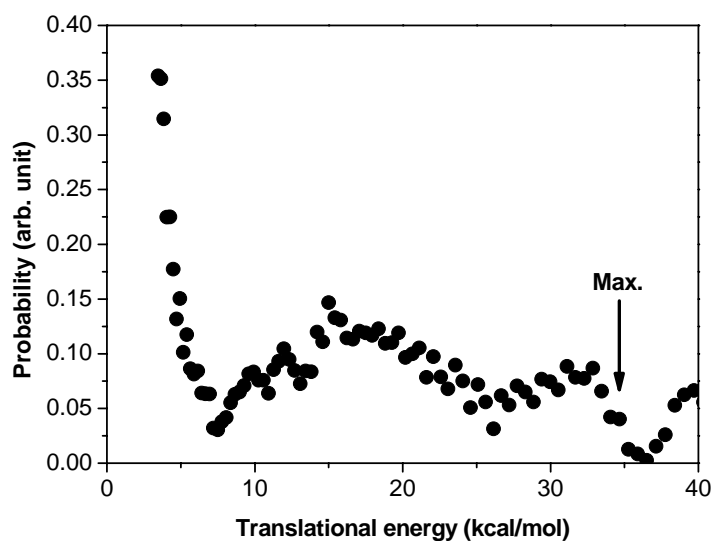


Fig.7 (a) The ion image of  $m/e = 143$  at  $145 \mu\text{s}$  pump-probe delay time with 248 nm laser excitation. (b) Photofragment translational energy distribution  $\text{C}_{10}\text{H}_8\text{O} + h\nu_{248\text{nm}} \rightarrow \text{C}_{10}\text{H}_7\text{O} + \text{H}$ .

### C. Discussions

The first absorption band of 1-naphthol is located in the region from 370 nm to 270 nm. The second absorption band starts from 270 nm, and the third absorption band begins at 230 nm. The absorption of 248 nm and 193 nm photons corresponds to the excitation to the  $S_2$  and  $S_3$  (or  $S_4$ ) states, respectively. The two components in the translational energy distribution suggest H atom elimination results from two mechanisms. The most likely interpretation is similar to the phenol dissociation mechanism: the slow component results from the ground state dissociation and the fast component results from predissociation of the repulsive state. However, dissociation from the other excited state, like triplet state, cannot be totally excluded due to the lack of the potential energy surface at this moment. On the other hand, differences between phenol and 1-naphthol also exist. The percentages of the slow components at both 248 nm and 193 nm are much larger than those of phenol, indicating the more important internal conversion in 1-naphthol. In addition, due to the relatively low O–H bond dissociation threshold (3.56 eV, compared to 3.86 eV of phenol), H atom elimination becomes the only dissociation channel on the ground state and CO and  $\text{H}_2\text{O}$  eliminations were not found in 1-naphthol.

The photoionization cross section of hot fragments was nearly identical for

different internal energized fragment when the ionization photon energy is more than 0.5 eV above the adiabatic ionization potential of fragments<sup>27</sup>. This argument was confirmed by the momentum match measurements of corresponding fragments in the photodissociation experiments which the VUV laser<sup>33</sup> or synchrotron radiation<sup>28</sup> are used to ionize fragments. Moreover, the experiments by tuning the VUV laser slightly above the ionization potential of the fragments are also support the arguments.<sup>29</sup> Due to the non-linear polarized pump laser and the isotropic distribution of ground state dissociative products, the ratio of ion intensity of slow and fast component is equal to the branching ratio of ground and excited state dissociation.

If the residual energy of the ion, which is equal to the photon energy of VUV laser minus the ionization potential of neutral parent molecule, is large enough, then the cracking of parent ion will occur. This is the so called “dissociative ionization”. Similar to the hot parent molecules, the hot fragment will crack if the residual energy in the hot fragment ion is large enough. When photoionization wavelength is 118 nm, the disk-like ion image of  $m/e = 115$  was observed, as shown in the Fig. 4(a). Since the disk shape image becomes slightly longer in the velocity axis as the pump-probe delay time increases as shown in the Fig. 4(b), it is from the dissociative ionization of the hot naphthoxyl radical. The reason for the slight changes in image length is due to the small kinetic energy of the hot naphthoxyl radical. But no disk image of  $m/e = 115$  was observed when 118 nm is replaced by 157 nm. So the ion intensity ratio of slow and fast component of  $m/e = 143$  can be determined from the data which 157 nm laser was used as a probe. From the experimental data, the ratio of slow component and fast component is 0.81:1 at 193 nm. There are the branching ratios of bifurcation pathways on the excited state potential surface. The ion ratio of slow and fast component is 0.61:1 at 248 nm.

In the phenol case<sup>7,9</sup>, the  $S_1$  state is located at  $\sim 4.5$  eV vertically above the ground state and the threshold of the conical intersection from  $\pi \pi^*$  to  $\pi \sigma^*$  state is  $\sim 5$  eV. The portion of the slow component that increases as the excitation varies from 248 nm to 193 nm indicates the importance of H atom elimination from the ground state at shorter UV wavelength. It is likely that the rate of internal conversion becomes very large at short UV wavelength. The similar results have been obtained in the 1-naphthol case. About 20% increase of ground state dissociation is observed at short UV wavelength.

The major dissociation channels for phenol with 6.4 eV (193 nm) include the OH bond fission, CO elimination, and H<sub>2</sub>O elimination. Even the photon energy reduces to 5 eV (248 nm), the former two channels are still observed. Only single dissociation channel, H atom release, occurs in the 1-naphthol. This is similar to

indole. Both molecules are larger than phenol in terms of numbers of atoms. These large molecules with more internal degree of freedom redistribute the photon energy in the ground state prior to the dissociation. The result is only one dissociation channel was recorded in the experimental time window, which is as long as one hundred microsecond.

The high resolution photofragment translation spectroscopy of H-atom loss of pyrrole and phenol has been studied by velocity map ion imaging technique<sup>15</sup> and H-atom Rydberg tagging time-of-flight (TOF) methods<sup>6</sup>. These measurements detect the light fragment, H-atom, which has larger recoil velocity compared to the corresponding heavy fragment naphthoxyl radical. These high resolution techniques reveal the detail dissociation mechanism by resolving the internal energy distribution of co-fragment. In order to detect the high velocity H-atom, the delay time between pump and probe laser is set to be less than 10 ns. Otherwise, the fast H-atom will fly out the probe region. Depending on the size of molecules, the ground state dissociative lifetime of the aromatic molecules is in the range of hundreds nanosecond and tens of microsecond after absorbing UV photons. In the other words, these high resolution techniques can detect the fast excited state dissociation, but they are unfavorable to detect the ground state dissociation products. The multimass technique we used provides complementary information to the high resolution techniques.

## Conclusions

We present data on the photodissociation of phenol and 1-naphthol using multi-mass technique. The major dissociation channel of at 193 nm and 248 nm is OH bond fission in the ground state and excited state. The ratio of the ground and excited state dissociation was determined by resolved bimodal photofragment translational energy distribution.

## References

- <sup>1</sup> D. Solgadi, C. Juvet, and A. Tramer, *J. Phys. Chem.* **92**, 3313 (1988)
- <sup>2</sup> C. Juvet, C. Dedonder-Lardeux, M. Richard-Viard, D. Solgadi, and A. Tramer, *J. Phys. Chem.* **94**, 5041 (1990).
- <sup>3</sup> J. Steadman and J. A. Syage, *J. Phys. Chem.* **92**, 4630 (1990)
- <sup>4</sup> J. A. Syage and J. Steadman, *J. Chem. Phys.* **95**, 2497 (1991)
- <sup>5</sup> J. Steadman and J. A. Syage, *J. Am. Chem. Soc.* **113**, 6786 (1991)
- <sup>6</sup> J. A. Syage and J. Steadman, *J. Phys. Chem.* **96**, 9606 (1992).

- 
- <sup>7</sup> J. A. Syage, *Chem. Phys. Lett.* **202**, 227 (1993).
- <sup>8</sup> M. F. Hineman, D. F. Kelley, and E. R. Bernstein, *J. Chem. Phys.* **99**, 4533 (1993).
- <sup>9</sup> O. David, C. Dedonder-Lardeux and C. Jouvet, *Int. Rev. in Phys. Chem.*, **21**, 499 (2002)
- <sup>10</sup> C. Jacoby, P. Hering, M. Schmitt, W. Roth, and K. Kleinermanns, *Chem. Phys.* **23**, 239 (1998).
- <sup>11</sup> G. Pino, G. Gre'goire, C. Dedonder-Lardeux, C. Jouvet, S. Martrenchard, and D. Solgadi, *J. Chem. Phys.* **111**, 10747 (1999).
- <sup>12</sup> G. Pino, G. Gre'goire, C. Dedonder-Lardeux, C. Jouvet, S. Martrenchard, and D. Solgadi, *Phys. Chem. Chem. Phys.* **2**, 893 (2000).
- <sup>13</sup> S. Ishiuchi, M. Saeki, M. Sakai, and M. Fujii, *Chem. Phys. Lett.* **322**, 27 (2000).
- <sup>14</sup> S. Ishiuchi, M. Saeki, M. Sakai, K. Daigoku, T. Ueda, T. Yamanaka, K. Hashimoto, and M. Fujii, *Chem. Phys. Lett.* **347**, 87 (2001).
- <sup>15</sup> A. L. Sobolewski and W. Domcke, *J. Phys. Chem. A* **105**, 9275 (2001).
- <sup>16</sup> A. L. Sobolewski, W. Domcke, C. Dedonder-Lardeux, and C. Jouvet, *Phys. Chem. Chem. Phys.* **4**, 1093 (2002).
- <sup>17</sup> K. Daigoku, S. Ishiuchi, M. Sakai, M. Fujii, and K. Hashimoto, *J. Chem. Phys.* **119**, 5149 (2003).
- <sup>18</sup> C. M. Tseng; Lee, Y. T.; Ni, C. K. *J. Chem. Phys.* **2004**, *121*, 2459
- <sup>19</sup> Tseng, C. M.; Y. T. Lee; M. F. Lin; C. K. Ni; S. Y. Liu; Y. P. Lee; Z. F. Xu; M. C. Lin, *J. Phys. Chem. A*, **111**, 9463(2007)
- <sup>20</sup> (a)O. Cheshnovsky and S. Leutwyler, *Chem. Phys. Lett.* **121**, 1 (1985). (b)O. Cheshnovsky and S. Leutwyler, *J. Chem. Phys.* **88**, 4127 (1985). (c) E.R. Bernstein, in *Chemical Reactions in Clusters*, edited by E.R. Bernstein (Oxford University Press, New York, 1996). (d) C. Jouvet and D. Solgadi, in *Chemical Reactions in Clusters*, edited by E.R. Bernstein (Oxford University Press, New York, 1996). (e) Q. Zhong and A.W.J. Castleman, *Chem. Rev.* **100**, 1049 (2000).
- <sup>21</sup> C. L. Huang, J. C. Jiang, S. H. Lin, Y. T. Lee, and C. K. Ni, *J. Chem. Phys.* **116**, 7779 (2002).
- <sup>22</sup> C. L. Huang, J. C. Jiang, Y. T. Lee, and C. K. Ni, *J. Chem. Phys.* **117**, 7034 (2002).
- <sup>23</sup> A. Bussandri and H. van Willigen, *J. Phys. Chem. A* **106**, 1524 (2002).
- <sup>24</sup> R. Hermann, G. R. Mahalaxmi, T. Jochum, S. Naumov, and O. Brede, *J. Phys. Chem. A* **106**, 2379 (2002).
- <sup>25</sup> H. D. Bist, J. C. D. Brand, and D. R. Williams, *J. Mol. Spectrosc.* **24**, 413 (1967).
- <sup>26</sup> A. Sur and P. M. Johnson, *J. Chem. Phys.* **84**, 1206 (1986).
- <sup>27</sup> Aguirre F. and Pratt S.T., *J. Chem. Phys.* **122**, 234303 (2005)
- <sup>28</sup> Shih-Huang Lee, Yuan T. Lee and Xueming Yang, *J. Chem. Phys.* **120**, 10983 (2004)



---

<sup>29</sup> I. Hünig, C. Plützer, K. A. Seefeld, D. Löwenich, M. Nispel, and K. Kleinermanns, *ChemPhysChem* **5**, 1427 (2004).



## Chapter 6. The photodissociation of *p*-methylphenol, *p*-ethylphenol, phenylethylamine and *p*-(2-aminoethyl)phenol, chromophores of the amino acid tyrosine

### Abstract

The photodissociation of *p*-methylphenol, *p*-ethylphenol, phenylethylamine and *p*-(2-aminoethyl)phenol, chromophores of the amino acid tyrosine, was studied separately for each compound in a molecular beam at 248 nm using multimass ion imaging techniques. They show interesting side-chain size-dependent dissociation properties. Only one dissociation channel, that is, H atom elimination, was observed for both *p*-methylphenol and *p*-ethylphenol. The photofragment translational energy distributions and potential energy surfaces from ab initio calculation suggest that H atom elimination occurs from a repulsive excited state. On the other hand, the H atom elimination channel is quenched completely by internal conversion and/or intersystem crossing in *p*-(2-aminoethyl)phenol. Only C-C bond cleavage was observed from phenylethylamine and *p*-(2-aminoethyl)phenol. The photofragment translational energy distribution shows a slow component and a fast component. The fast component results from dissociation on an electronic excited state, but the slow component occurs only after the internal conversion to the ground electronic state. Comparison with the photodissociation of phenol and ethylbenzene is made.

### Introduction

The amino acids are some of the most important biomolecules. Aromatic amino acids like tyrosine, tryptophan, and phenylalanine have very large UV absorption cross sections. However, the fluorescence quantum yields of these molecules are very small. They indicate the existence of fast nonradiative processes, which efficiently quench the fluorescence.<sup>1,2,3,4</sup> The nonradiative process was assumed to be the ultrafast internal conversion.<sup>2-5</sup> As soon as the electronic energy becomes vibrational energy after internal conversion, the highly vibrationally excited molecules quickly dissipate the vibrational energy to the surrounding molecules through intermolecular energy transfer before chemical reactions take place. This so-called photostability prevents the unnecessary photochemical reactions of these molecules upon UV irradiation.

Phenol is a chromophore of the amino acid tyrosine. Recent ab initio calculation

suggests that the low fluorescence quantum yield of phenol is due to the dissociative character of the electronic excited-state potential energy surface, instead of fast internal conversion to the electronic ground state.<sup>6,7,8</sup> The calculation shows that absorption of UV photons in the range 290-240 nm corresponds to the photoexcitation of phenol to the S1  $\pi \sigma^*$  excited state. The second excited state has a significant antibonding  $\sigma^*$  character with respect to the OH bond distance. The population of the bright state, S<sub>1</sub>, can be transferred to the dark state, S<sub>2</sub>, through a conical intersection. As a result, instead of internal conversion to the ground electronic state, predissociation through  $\pi \sigma^*$  and  $\pi \sigma^*$  coupling results in rapid quenching of the fluorescence. Indeed, the H atom elimination from the repulsive electronic excited state of phenol has been verified in a recent molecular beam experiment.<sup>9</sup> A similar dissociation channel was also observed from indole, a chromophore of the amino acid tryptophan.<sup>10</sup>

Since phenol is different from tyrosines-it lacks a side chain of the functional group  $\text{CH}_2\text{CH}(\text{NH}_2)\text{COOH}$ , it would be very interesting to determine the photodissociation properties when the chemical functional group is added to phenol. In this work, we reported the photodissociation of *p*-methylphenol, *p*-ethylphenol, phenylethylamine and *p*-(2-aminoethyl)phenol. We demonstrate that the dissociation properties could change dramatically as the side chain is added to phenol.

## Experimental

The multimass ion imaging techniques have been described in detail in our previous chapter and only a brief account is given here. *p*-Methylphenol (or *p*-ethylphenol) vapor was formed by flowing ultrapure Ne at a pressure of 600 Torr through a reservoir filled with a *p*-methylphenol (or *p*-ethylphenol) sample at 80 °C. The *p*-methylphenol (or *p*-ethylphenol)/ Ne mixture was transferred through a 90 °C flexible stainless steel tube to a pulsed valve and then expanded through a 500  $\mu\text{m}$  high-temperature (100 °C) nozzle to form the molecular beam. The method to generate a *p*-(2-aminoethyl)phenol molecular beam is different from that of *p*-methylphenol. A glass container which contains a phenylethylamine or *p*-(2-aminoethyl)phenol solid sample located inside a stainless steel oven (100 °C) was attached to the front of a pulsed valve. The plunger of the pulsed valve extended to the exit hole (diameter: 500  $\mu\text{m}$ ) of the oven. The molecular beam was formed by expanding the *p*-(2-aminoethyl)-phenol/Ne mixture at a pressure of 600 Torr through the exit hole of the oven.

## Computational

The computation studies briefly described here was performed by Pro. Chang in the Department of Science Application and Dissemination, National Taichung University. The geometries of the ground states and some low-lying conformers of *p*-methylphenol, *p*-ethylphenol, and *p*-(2-aminoethyl) phenol were optimized at the B3LYP/6-311++G(d, p) level. Harmonic vibrational frequencies were calculated to confirm that the obtained geometries correspond to the equilibrium structures. In order to interpret the experimental observations, we computed the potential energy curves for the ground and excited states of these molecules as functions of the O-H distance, in intervals of 12 pm, while fixing the other geometrical parameters at their equilibrium values. The potential energy curves were calculated by using the state-averaged complete active space self-consistent field (CASSCF) method with the 6-311++G(d, p) basis set. The active space adopted in the CASSCF calculations was ten electrons distributed in ten orbitals, denoted as (10, 10). All the calculations were performed using the MOLPRO 2006.1 package.

## Results

### A. *p*-Methylphenol.

The only fragment ion we observe from the photodissociation of *p*-methylphenol at 248 nm using the 118 nm photoionization laser beam is  $m/e = 107$ , corresponding to the heavy fragment from the H atom elimination channel. The photofragment ion images are shown in Figure 1a, and the corresponding translational energy distribution is shown in Figure 2. The probability distribution in the region less than 5 kcal/mol is obscured by the strong interference from parent molecules. Only the distribution larger than 5 kcal/mol is illustrated. It shows that the average released translational energy is large, and the peak of the distribution is located at 18 kcal/mol. It is interesting to note that the maximum translational energy almost reaches the maximum available energy of the reaction. These are the characteristics of the dissociation from an excited state of a repulsive potential or from an electronic state with a large exit barrier height.

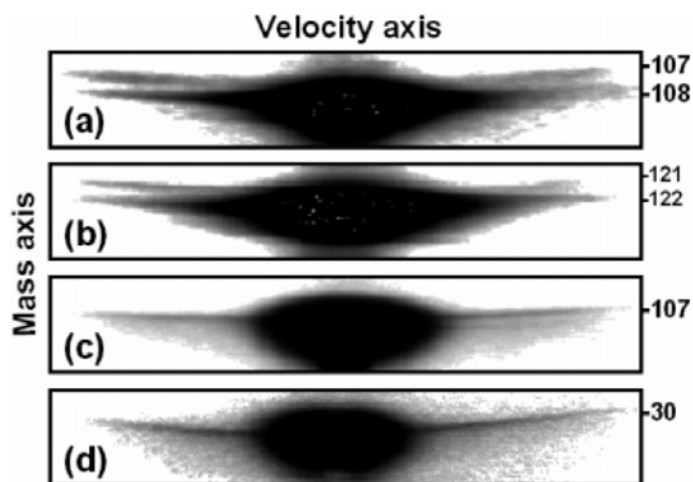


Figure 1. Photofragment ion images from (a) methylphenol, (b) ethylphenol, (c) and (d) *p*-(2-aminoethyl)phenol.

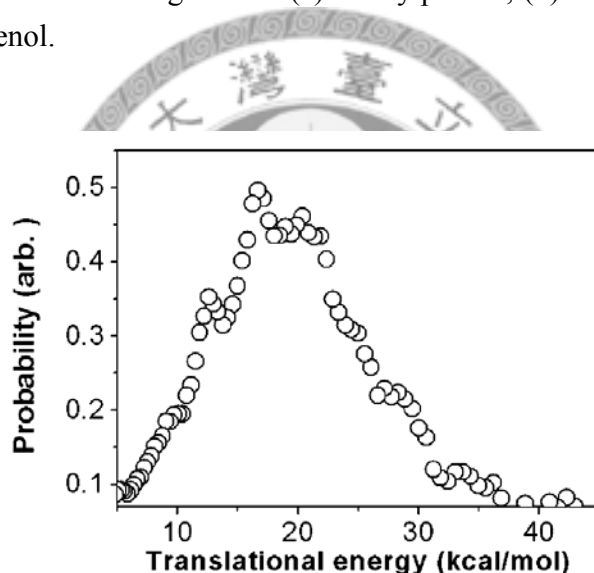


Figure 2. Photofragment translational energy distribution of the reaction  $\text{CH}_3\text{C}_6\text{H}_4\text{OH} \rightarrow \text{CH}_3\text{C}_6\text{H}_4\text{O} + \text{H}$ .

The translational energy distribution is very similar to that of H atom elimination from photodissociation of phenol at 248 nm. The large translational energy release in the H atom elimination channel of phenol at 248 nm was explained as the dissociation from a repulsive potential energy surface.<sup>9</sup> Indeed, a similar repulsive potential energy surface along the O-H bond distance of *p*-methylphenol was also found from our calculation. Figure 3 shows potential energy curves of the first four singlet electronic states along the O-H bond distance. The ground state is a stable state with respect to the O-H bond

distance. The first electronic excited state,  $\pi\sigma^*$ , shows a potential well at a short O-H bond distance. It crosses with a repulsive potential,  $\pi\sigma^*$ , at a large O-H bond distance. This calculation suggests that methylphenol can dissociate through the repulsive potential energy surface as long as the excitation energy is large enough to overcome the barrier height at the crossing point.

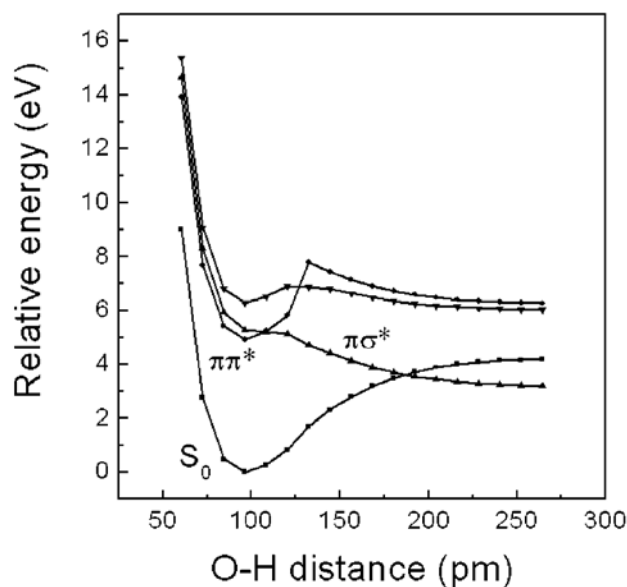


Figure 3. Potential energy curves of *p*-methylphenol as functions of the O-H distance calculated at the CASSCF(10,10)/6-311++G(d, p) level.

The fragment translational energy distribution and potential energy surfaces suggest that the H atom elimination occurs from the repulsive potential surface along the O-H bond (eq 1):



The potential energy curves in Figure 3 were calculated at the ground-state geometry of the most stable conformer. The structure is shown in Figure 4a. The ground-state structure of the other stable conformer is shown in Figure 4b. For this conformer, we calculated the three lowest-lying states at two structures, one at the equilibrium structure of the ground state and the other at O-H = 210 pm. It was found that while the  $\pi\sigma^*$  state lies higher than the ground state and the  $\pi\sigma^*$  state at the structure of the ground

state, it becomes the lowest one at O-H = 210 pm. Accordingly, the potential energy curve of the  $\pi \sigma^*$  state must intersect somewhere with that of the  $\pi \sigma^*$  state and that of the ground state, respectively, similar to those in Figure 3.

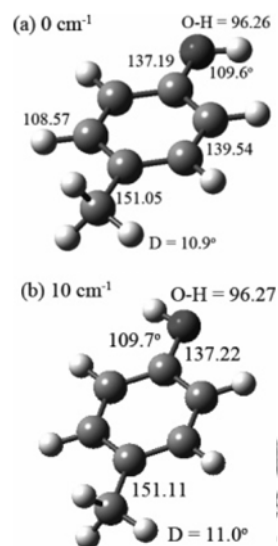
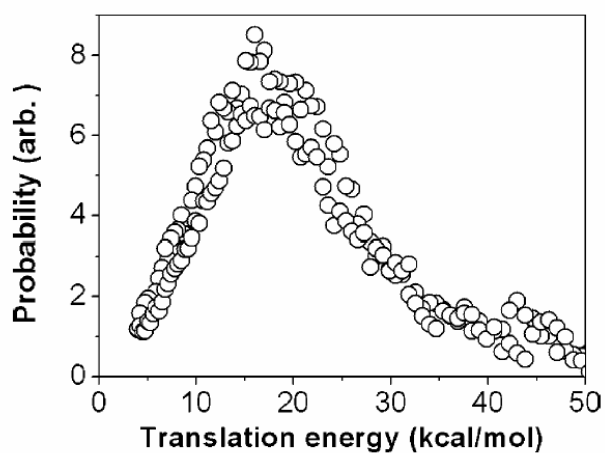


Figure 4. B3LYP/6-311G++(d, p) optimized equilibrium structures of the ground state *p*-methylphenol and relative energies of two conformers with selected bond lengths (in pm) and bending angles. D is the dihedral angle between the methyl group and the benzene ring (nearly parallel).

### B. *p*-Ethylphenol.

Similar dissociation dynamics was found from the photodissociation of *p*-ethylphenol at 248 nm. Only the fragment ion of  $m/e = 121$  was observed, as illustrated in Figure 1b. This corresponds to the heavy fragment resulting from H atom elimination. The photofragment translational energy distribution is shown in Figure 5. It shows that the average translational energy is large, and the peak of the distribution is located at 18 kcal/mol. The electronic potential energy curves along the O-H bond distance are illustrated in Figure 6. A similar repulsive potential along the O-H bond distance was found. The experimental data and potential energy surface calculation suggest that H atom elimination occurs through the following reaction (eq 2):





**Figure 5.** Photofragment translational energy distribution of the reaction  $\text{C}_2\text{H}_5\text{C}_6\text{H}_4\text{OH} \rightarrow \text{C}_2\text{H}_5\text{C}_6\text{H}_4\text{O} + \text{H}$ .

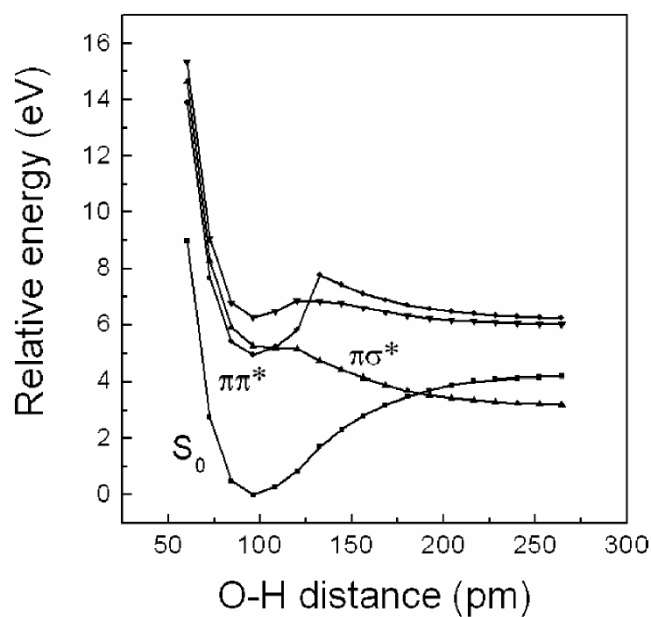


**Figure 6.** Potential energy curves of *p*-ethylphenol as functions of the O-H distance calculated at the CASSCF(10,10)/6-311++G(d, p) level.

The potential energy curves in Figure 6 were calculated at the ground-state geometry for the most stable conformer. The corresponding structure is shown in Figure 7a. The ground state structure of the other stable conformer is shown in Figure 7b. From



the calculation of the three lowest states at the equilibrium structure of the ground state and in the vicinity of 200 pm, we confirmed the existence of a repulsive potential,  $\pi\sigma^*$ , along the O-H coordinate for the other conformer.

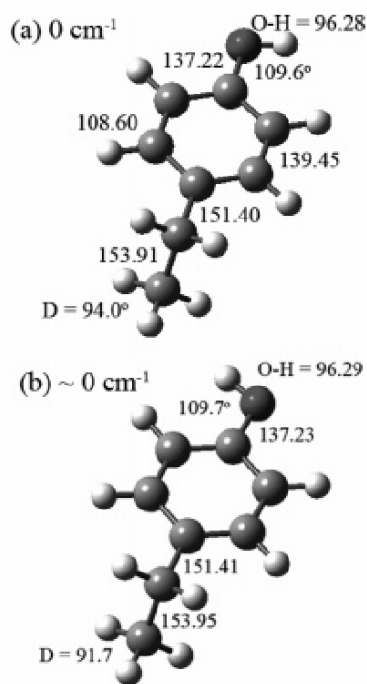


**Figure 7.** B3LYP/6-311G++(d, p) optimized equilibrium structures and relative energies of the ground-state *p*-ethylphenol of two conformers with selected bond lengths (in pm) and bending angles. D is the dihedral angle between the ethyl backbone and the benzene ring (nearly perpendicular).

### C. phenylethylamine

Interesting photodissociation properties were found from the photodissociation of phenylethylamine. No fragments corresponding to H atom elimination were observed. The fragment ions  $m/e = 91$  was found at 248 nm using the 118 nm photoionization laser beam. The ion images of  $m/e = 91$  elimination at different pump-probe delay time are illustrated in Fig. 8.



Figure 8. The ion image for  $m/e = 91$  at (a)  $12 \mu\text{s}$  and (b)  $15 \mu\text{s}$  pump-probe delay time, respectively, with 248 nm laser excitation

The translational energy distributions at 248 nm show two components, as shown in Fig. 10.

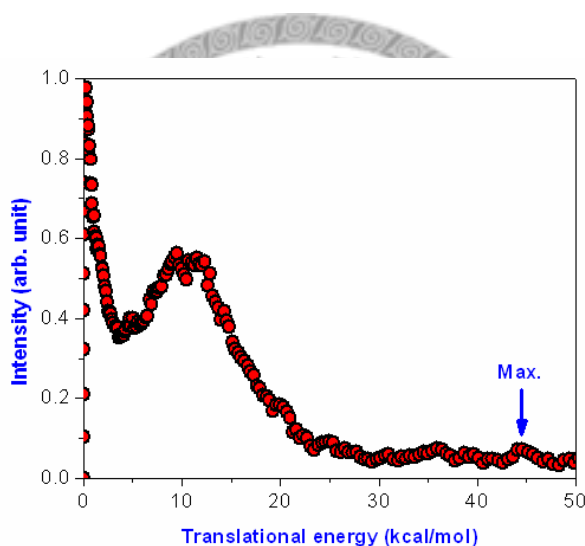
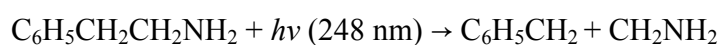


Figure 10. Photofragment translational energy distribution of reaction



The ion images of  $\text{CH}_3$  elimination at 248 nm are illustrated in Fig. 11. In contrast to the photodissociation at 248 nm, the translational energy distributions at 193 nm show only one component, as shown in Fig. 12.

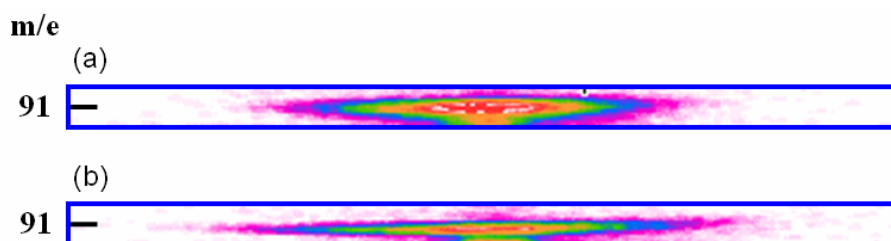


Figure 11. The ion image for  $m/e = 91$  at (a)  $10 \mu\text{s}$  and (b)  $17 \mu\text{s}$  pump-probe delay time, respectively, with 193 nm laser excitation

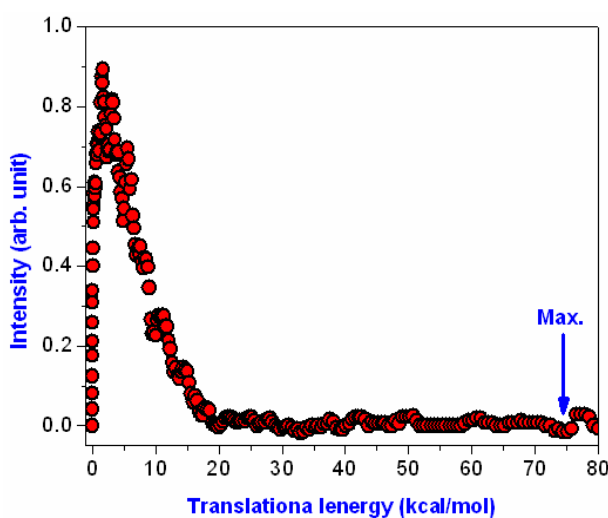
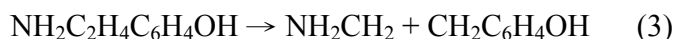


Figure 12. Photofragment translational energy distribution of reaction  
 $\text{C}_6\text{H}_5\text{CH}_2\text{CH}_2\text{NH}_2 + h\nu (193 \text{ nm}) \rightarrow \text{C}_6\text{H}_5\text{CH}_2 + \text{CH}_2\text{NH}_2$

#### D. *p*-(2-Aminoethyl)phenol.

Significantly different photodissociation properties were found from the photodissociation of *p*-(2-aminoethyl)phenol. No fragments corresponding to H atom elimination were observed. Only the fragment ions  $m/e = 30$ , 106, and 107 were found at 248 nm using the 118 nm photoionization laser beam. Fragment ions  $m/e = 106$  and 107 have similar intensity distributions along the velocity axis. It suggests fragment ion  $m/e = 106$  results from fragment cracking of  $m/e = 107$  due to the excess VUV photon energy. This can be confirmed from the fact that only fragment ions  $m/e = 107$  and 30 were observed as the VUV wavelength was changed from 118 to 157 nm. The dissociation can be described by the following reaction (eq 3):



The photofragment translational energy distribution of the reaction shown in eq 3 is illustrated in Figure 13. It is obvious that there are two components in the distribution. The two components in the distribution indicate that there are at least two mechanisms involved in the dissociation of *p*-(2-aminoethyl) phenol at 248 nm. For the slow component, the average translational energy release is small and the fragment translational energy distribution decreases monotonically with the translational energy. These are typical characteristics of a dissociation from hot molecules. On the other hand, the average released translational energy for the fast component is large, and the peak of the distribution is located far away from zero. These are the characteristics of dissociation from an excited state with a repulsive potential energy surface, or from an electronic state with a large exit barrier height.

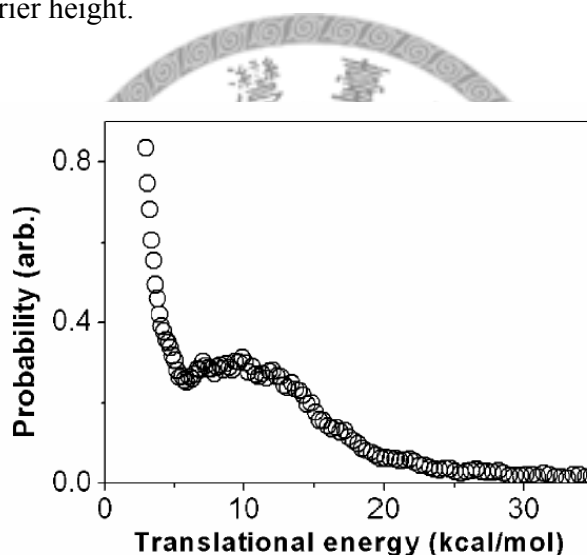


**Figure 13.** Photofragment translational energy distribution of the reaction  $\text{NH}_2\text{C}_2\text{H}_4\text{C}_6\text{H}_4\text{OH} \rightarrow \text{NH}_2\text{CH}_2 + \text{CH}_2\text{C}_6\text{H}_4\text{OH}$ .

Similar translational energy distributions have also been found in the photodissociation of ethylbenzene, propylbenzene, and ethyltoluene at 248 nm.<sup>11,12,13</sup> For ethylbenzene, propylbenzene, and ethyltoluene, the alkyl group C-C bond cleavage is the major dissociation channel. The photofragment translational energy distributions of these molecules show a slow component and a fast component. Since the alkyl group is not an electronic chromophore at 248 nm, an electronic excited state with a repulsive potential along the C-C bond is not expected to play a role in this photon energy region. The

dissociation mechanism was interpreted as the slow component in the translational energy distribution resulting from the ground-state dissociation and the fast component resulting from the triplet-state dissociation. The fast component resulting from the triplet state was confirmed from the ab initio calculation that a large barrier does exist in the exit channel. An analogous dissociation mechanism can also be applied here to explain the photodissociation of phenylethylamine and *p*-(2-aminoethyl)phenol at 248 nm.

We also performed similar calculations for *p*-(2-aminoethyl)-phenol. Figure 14 shows the electronic potential energy curves along the O-H bond distance of the most stable conformer of *p*-(2-aminoethyl)phenol. The repulsive characteristic of the potential energy surface along the O-H bond distance of *p*-(2-aminoethyl)phenol was observed. The structures of the most stable conformer and the other conformers are illustrated in Figure 10. For the other conformers, we calculated the three lowest electronic states at the equilibrium structure of the ground state and in the vicinity of 200 pm. We confirmed the existence of a repulsive potential,  $\pi\sigma^*$ , along the O-H coordinate for all the other conformers.

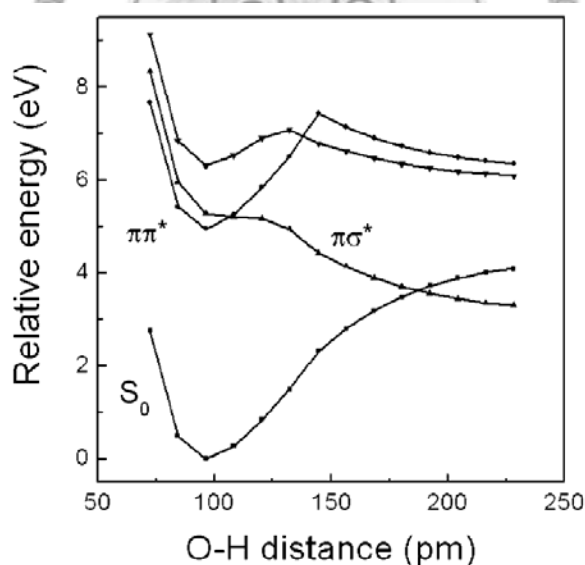


**Figure 14.** Potential energy curves of *p*-(2-aminoethyl)phenol as functions of the O-H distance calculated at the CASSCF(10,10)/6-311++G(d, p) level.

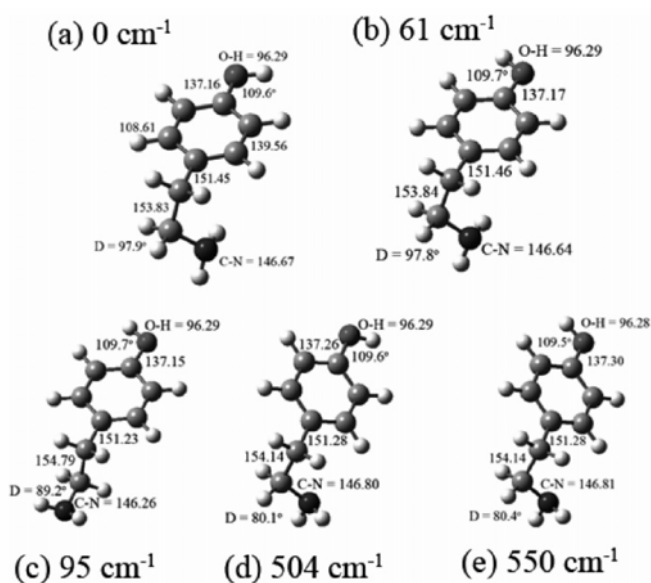


**Figure 10.** B3LYP/6-311G++(d, p) optimized equilibrium structures and relative energies of the ground-state *p*-(2-aminoethyl)phenol of several conformers with selected bond lengths (in pm) and bending angles. D is the dihedral angle between the ethyl backbone and the benzene ring (nearly perpendicular).

## Discussion

The results of these three amino acid chromophores reveal interesting side-chain size-dependent dissociation properties. Since the alkyl group and amino group are not the absorption chromophores at 248 nm, photoexcitation of *p*-methylphenol, *p*-ethylphenol, phenylethylamine and *p*-(2-aminoethyl)phenol at 248 nm photons all correspond to the excitation of the phenyl ring. However, the decay of the excited phenyl ring is very different between these three molecules. For both *p*-methylphenol and *p*-ethylphenol, the major relaxation of the excited phenyl ring is through the coupling between the  $\pi\pi^*$  and  $\pi\sigma^*$  states. As a result, H atom elimination from a repulsive state is the major dissociation channel. These observations demonstrate that the dissociation from the repulsive excited state plays an important role in small tyrosine chromophores, including phenol, *p*-methylphenol, and *p* ethylphenol. As the side chain changes from H, CH<sub>3</sub>, or C<sub>2</sub>H<sub>5</sub> to C<sub>2</sub>H<sub>4</sub>NH<sub>2</sub>, the dissociation properties change dramatically. The change could be due to two effects from the side chain. First, the change of the location of the repulsive potential energy surface could render it inaccessible under current photoexcitation conditions. However, our calculations show that the repulsive characteristic of the potential energy surface along the O-H bond distance exists in all three molecules. In addition, the energy

of the repulsive potential energy surface remains in the same region that the energy from the absorption of 248 nm photon is enough to reach the repulsive part of the potential energy surface, although it does not necessarily indicate that the absorption spectra and coupling strength between the  $\pi\pi^*$  and  $\pi\sigma^*$  states remains the same. An explanation of the similar electronic potentials of these chromophores is that these states correspond to the transitions from the  $\pi$  orbitals of the benzene ring to the  $\sigma^*(\text{OH})$  and  $\pi^*$  orbitals, while the methyl, ethyl, and aminoethyl groups do not significantly change the electronic structures of these low-lying states.

The other effect of the side-chain is the increase in the  $S_1$ - $S_0$  internal conversion rate and/or  $S_1$ - $T_1$  intersystem crossing rate which competes with the predissociation from the repulsive potential energy surface. Since the internal conversion and intersystem crossing rates are proportional to the density of states, the replacement of a H atom by a side chain increases the density of states substantially due to the low vibrational frequency modes, like torsion, in the side chain. Obviously, the increase of the internal conversion/intersystem crossing rate is not large enough in *p*-methylphenol and *p*-ethylphenol to compete with the predissociation from the repulsive potential energy surface. However, the internal conversion rate or intersystem crossing rate in *p*-(2-aminoethyl)phenol is large enough that the predissociation from the repulsive state is quenched completely.

Internal conversion to the ground state also can occur through the other channel, that is, from the  $\pi\sigma^*$  state to the ground state through the second conical intersection in the vicinity of 200 pm. In addition, intersystem crossing can occur via a similar mechanism if a conical intersection between the triple state and the  $S_2$  state exists. Nevertheless, the results of these alternatives in *p*-(2-aminoethyl)phenol are the same, that is, they quench the population of the  $S_2$  state and make the H atom elimination from the repulsive state impossible.

Since the energies of different conformers are very close, more than one conformer existed in the molecular beam. In addition, the rotational barriers for the methyl, ethyl, and 2-aminoethyl groups are about 10-20  $\text{cm}^{-1}$  for these molecules calculated at the B3LYP/6-311++G(d, p) level, indicating that they can rotate freely. The results therefore are the averages according to the populations of each conformer in the molecular beam. Although we cannot determine the relative contributions of these conformers, the experimental results show that all of the conformers of methylphenol and ethylphenol existing in the molecular beam only dissociate along the O-H bond on the repulsive potential energy surface. On the other hand, none of the conformers of *p*-(2-

aminoethyl)phenol that existed in the molecular beam dissociate on the repulsive potential energy surface. They only dissociate through C-C bond cleavage on the ground state and/or the triplet state.

Comparison of these four chromophores reveals an interesting side-chain effect on the dissociation dynamics. A future challenge is to find out the dissociation dynamics of the conformers that currently do not exist in the molecular beam, the larger chromophores, or tyrosine itself.

## References

---

- <sup>1</sup> M. B. Robin, *Higher Excited States of Polyatomic Molecules*(Academic: New York, 1972).
- <sup>2</sup> C. Crespo-Hernandez, E. B. Cohen, P. M. Hare and Kohler, B. Chem. Rev.**104**, 1977(2004).
- <sup>3</sup> R. Callis, Annu. Rev. Phys. Chem, **34**, 329(1983).
- <sup>4</sup> D. Creed, Photochem. Photobiol., **39**, 537(1984).
- <sup>5</sup> A. Reuther, H. Iglev, R. Laenen and A. Laubereau, Chem. Phys. Lett., **325**, 360(2000).
- <sup>6</sup> A. L. Sobolewski, W. Domcke, C. Dedonder-Lardeux, and C. Jouvet, Phys. Chem. Chem. Phys., **4**, 1093(2002) .
- <sup>7</sup> Z. Lan, W. Domcke, V. Vallet, A. L. Sobolewski, and S. Mahapatra, S. J. Chem. Phys., **122**, 224315(2005).
- <sup>8</sup> A. L. Sobolewski and W. Domcke, J. Phys. Chem. A, **105**, 9275(2001).
- <sup>9</sup> C. M. Tseng, Y. T. Lee and C. K. Ni, J. Chem. Phys., **121**, 2459(2004)
- <sup>10</sup> M. F. Lin, C. M. Tseng, Y. T. Lee and C. K. Ni, J. Chem. Phys., **123**, 124303(2005).
- <sup>11</sup> C. L. Huang, J. C. Jiang, S. H. Lin, Y. T. Lee and C. K. Ni, J. Chem. Phys., **116**, 7779(2002)
- <sup>12</sup> C. L. Huang, J. C. Jiang, S. H. Lin, Y. T. Lee and C. K. Ni, J. Chem. Phys., **117**, 7034(2002).
- <sup>13</sup> C. L. Huang, Y. A. Dyakov, S. H. Lin, Y. T. Lee and C. K. Ni, J. Phys. Chem. A, **109**, 4995(2005).



## Chapter 7. The photodissociation of indole, 3-methyl-indole, tryptamine and tryptophan

### Abstract

Photodissociation dynamics for various tryptophan chromophores was studied at 193 or 248 nm using multimass ion imaging techniques. The competition between internal conversion to the ground electronic state and dissociation from the repulsive excited state reveals size-dependent photostability for these amino acid chromophores. As the size of chromophore increases, internal conversion to the ground state becomes the major nonradiative process.

### Introduction

One important photophysical characteristic of amino acids is their low fluorescence quantum yields upon excitation by ultraviolet (UV) light.<sup>1,2,3,4</sup> Such behavior indicates the presence of fast nonradiative channel that efficiently quench the fluorescence. This nonradiative process is assumed to be the ultrafast internal conversions to the ground electronic state. The so-called “photostability” for these molecules can prevent undesirable photochemical reactions from initiating after UV irradiation.<sup>2,3</sup> However, recent theoretical calculations<sup>5,6,7,8,9</sup> suggest that the low fluorescence quantum yields for phenol, imidazole, and indole (the respective chromophores for the amino acids tyrosine, histidine, and tryptophan) are due to the dissociative characteristics of the excited electronic state potential energy surface, rather than the direct fast internal conversion to the ground electronic state.

Figure 1, taken from Ref. 7, shows a section through multidimensional diabatic potential energy surfaces for the ground and first excited  $\pi\sigma^*$  and  $\pi\pi^*$  states of indole molecules as plotted against N–H bond distances. The first excited  $\pi\pi^*$  state is bound with respect to N–H bond distance, but the  $\pi\sigma^*$  state is repulsive. The diabatic  $\pi\sigma^*$  potential correlates with the ground state products, C<sub>8</sub>NH<sub>6</sub> +H. Although the absorption of UV photons corresponds to excitation to the  $\pi\pi^*$  excited state, population of the  $\pi\pi^*$  state can be transferred to the  $\pi\sigma^*$  potential through a conical intersection. As a consequence, instead of direct internal conversion to the ground electronic state, dissociation from  $\pi\sigma^*$  provides an alternate explanation for the rapid fluorescence quenching. Similar repulsive potential energy surfaces (PESs) such as that of  $\pi\sigma^*$  were found for phenol along O–H bond and imidazole along N–H bond. The  $\pi\pi^*$  potential minima in both indole and phenol lie below that of the  $\pi\sigma^*$  PES (in the area near equilibrium geometry at the ground electronic state), whereas in

imidazole the  $\pi\sigma^*$  state is lowest in energy and can be accessed optically. Dissociation from these repulsive excited states has been verified in recent molecular beam experiments.<sup>10,11,12,13,14</sup> Because dissociation from an excited state having a repulsive potential energy surface is swift, quenching is incomplete even in the condensed phase. As a result, dissociation from the repulsive state and the reactions following generation of radicals from dissociation become a potential problem in amino acid photostability.

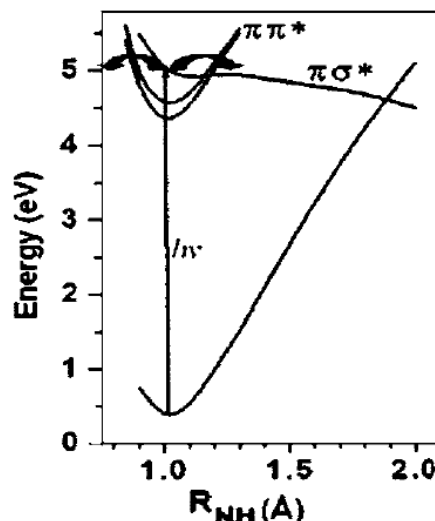


Fig. 1. Potential energy profiles for the ground and first excited  $\pi\pi^*$  and  $\pi\sigma^*$  states of indole plotted against the N-H bond distance (adapted from Ref. 7).

Tryptophan is the most photochemically active amino acid. Tryptophan has a greater capacity for absorbing UV photons than that for other aromatic amino acids, along with an ultraviolet spectrum, which extends to longer wavelengths. In this work, the photodissociation dynamics for various tryptophan chromophores, including indole, 3-methylindole, tryptamine, and tryptophan was investigated. We report the competition between internal conversion to the ground electronic state and dissociation from the repulsive excited state in these chromophores and provide an explanation for the amino acid photostability.

## Experimental

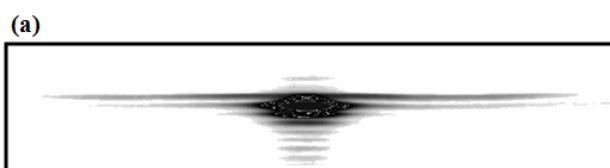
The experimental techniques have been described in chapter 2 and only a brief description is given here. Basically molecules in a molecular beam were photodissociated by a pulsed UV laser beam at 193 or 248 nm, then photofragments were ionized by vacuum UV (VUV) laser at 157 nm (and 118 nm for indole, 3-methylindole, and tryptamine). The masses of fragments were identified along with

their translational energy distributions using multimass ion imaging techniques. A homemade high temperature nozzle was used in this experiment. For 3-methylindole and tryptamine, a stainless steel oven maintained at 383 K was attached to the front port of a pulse valve. The inner surface of the oven was covered with glass and the plunger of the pulsed valve was extended to the exit port of the oven to control the opening of the oven. Compounds dissolved in methanol were sprayed on glass wool and dried by hot nitrogen gas before putting into the oven. For tryptophan, it was mixed with graphite powder and the oven was coated with graphite. Ultrapure He (or Ne) at a pressure of 400 Torr flowed through the oven and the sample/rare gas mixture was expanded through the exit port of the oven to form molecular beam. VUV photoionization and time-of-flight mass spectra were used to check the content of the molecular beam before the photodissociation experiment was performed. Molecules in that beam were photodissociated with a pulsed UV laser, followed by ionization with a pulsed VUV laser at 118 nm; a pulsed electric field served to extract the ions into a mass spectrometer. At the exit port of the mass spectrometer, a two dimensional ion detector was used to detect the ion positions and intensity distribution.

## Results

### I. The photodissociation of indole at 248 nm and 193 nm

Hydrogen atom elimination is the only dissociation channel for indole, both at 193 and 248 nm.<sup>11(a)</sup> Figure 2(a) and (b) show the multi-mass image and the photofragment translational energy distribution at 193 nm and reveals fast and slow components. The average translational energy released by the fast component is large. The distribution for the fast component indicates that the dissociation occurs either through a repulsive potential or from an electronic state having a large exit barrier. Because there is no significant exit barrier for the H atom elimination in the ground electronic state, the fast component in the translational energy distribution must result from dissociation in the electronically excited state. On the other hand, the average translational energy release for the slow component is small and the photofragment translational energy probability decreases monotonically with energy. These are the typical characteristics for statistical dissociation from a molecule undergoing internal conversion to the ground electronic state having no exit barrier.



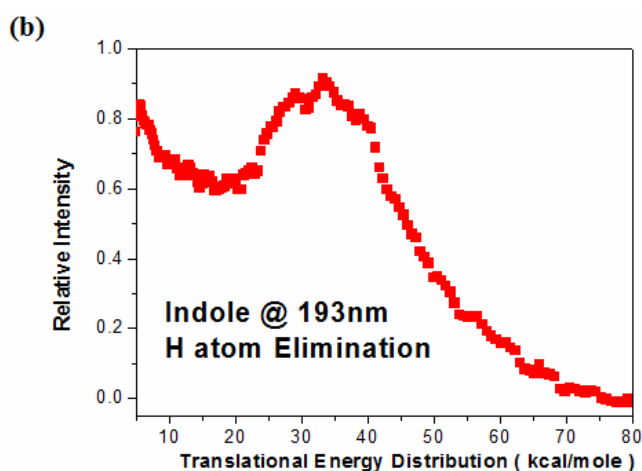


Fig. 2 The multimass image (a) and photofragment translational energy distribution (b) of  $C_8NH_7 \rightarrow C_8NH_7 + H$  at 193 nm.

A similar two-component translational energy distribution was observed for the photodissociation of indole at 248 nm, as illustrated in Fig. 3. Although molecules in the  $\pi\sigma^*$  can go through the second conical intersection and produce fragments in the ground state, as shown in Fig. 1, the dissociation properties from a repulsive state, i.e., large kinetic energy release, may remain as long as molecules dissociate into fragments quickly and directly without going into the potential well of the ground state. The observation of H atom elimination from the excited state supports predictions derived from *ab initio* calculations. For the photolysis wavelength at 193 nm, the dissociation from the ground state can produce fragment in the excited state, or in the ground state after undergoing the conical intersection at long distance (1.8 Å). However, the 248 nm photon energy is only large enough to produce the fragment in the ground state. As we will show in the text below, fragment that ended in the excited state or the ground state is not important in the photostability of amino acids.

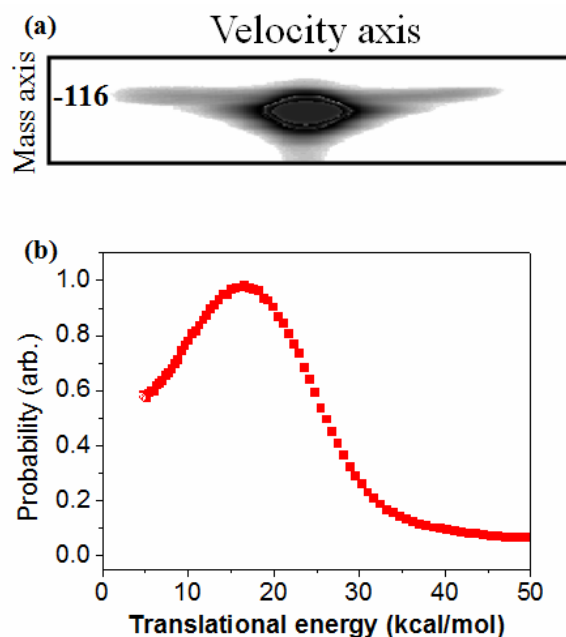


Fig. 3 The multimass image (a) and photofragment translational energy distribution (b) of  $C_8NH_7 \rightarrow C_8NH_7 + H$  at 248 nm.

## II. The photodissociation of 3-methylindole at 248 nm and 193 nm

In the study of 3-methylindole, 3-methylindole ions ( $m/e=131$ ) and a trace amount of dimer and 3-methylindole-H<sub>2</sub>O cluster ions were observed in the molecular beam. When the molecular beam was irradiated by 193 nm photons, fragment ions with  $m/e=130$  and 116 were observed by 157 nm photoionization and  $m/e=130$ , 116, and 15 were observed by 118 nm photoionization. They correspond to the fragments of H atom and CH<sub>3</sub> elimination channels. The ion intensity ratio between  $m/e=130$  and 116 is 60:1, indicating that the H atom elimination is the major channel. However, only H atom elimination was observed at 248 nm. The translational energy distributions are shown in Figs. 3(c). Because the methyl group is not the absorption chromophore in this UV region, photoexcitation of 3-methylindole only correlates to the excitation of the indole ring  $\pi\pi^*$ . However, the decay mechanism for the excited indole ring is different from indole. For 3-methylindole photodissociation at 193 nm, the relative intensity of the fast component decreases and that of the slow component increases, indicating that the cleavage of N–H or C–H (from CH<sub>3</sub>) bonds from the ground state becomes more important. In addition, CH<sub>3</sub> elimination from the ground state was observed.

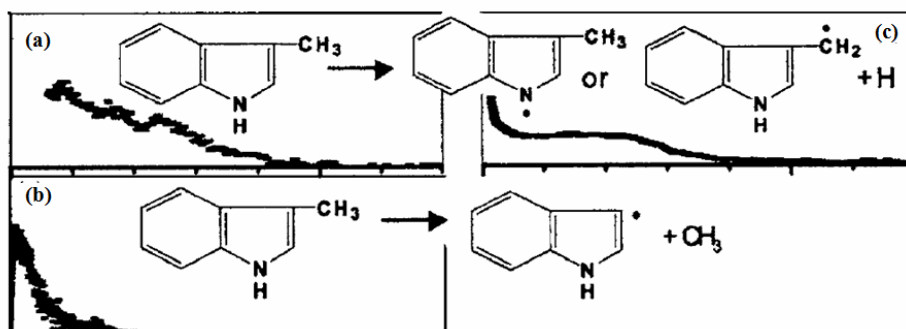


Fig. 3 The photofragment translational energy distribution (a)  $C_8NH_6CH_3 + hv$  (248 nm)  $\rightarrow C_8NH_5CH_3 + H$  or  $C_8NH_6CH_2 + H$  (b)  $C_8NH_6CH_3 + hv$  (248 nm)  $\rightarrow C_8NH_6 + CH_3$  (c)  $C_8NH_6CH_3 + hv$  (193 nm)  $\rightarrow C_8NH_5CH_3 + H$  or  $C_8NH_6CH_2 + H$

### III. The photodissociation of tryptamine at 248 nm and 193 nm

The content of tryptamine in the molecular beam checked by mass spectra shows tryptamine ion ( $m/e=160$ ) and a small amount (10%) of indole ions ( $m/e=117$ ). The existence of indole is due to the thermal decomposition of tryptamine in the oven. Since we know the dissociation channels and fragment translational energy distributions of indole, we can subtract the interference from indole easily. The result shows that the photofragment ions of tryptamine include  $m/e=130$  and 30. The momentum of line shape component of  $m/e=130$  matches with the momentum of  $m/e=30$ , indicating the C–C bond cleavage:  $C_8NH_6C_2H_4NH_2 \rightarrow C_8NH_6CH_2 + CH_2NH_2$ . Because dissociation through a C–C bond generates two radicals, this type of dissociation on the ground electronic state does not feature an exit barrier. The small translational energy release, as shown in Figs. 4(a) and 4(c), indicates that this channel must occur from the ground electronic state after internal conversion. The other component of  $m/e=130$  is a disk-like image. The size of the disk changes with the pump-probe delay time, indicating that it is from heavy fragment cracking due to excess VUV photon energy. The most likely fragment is  $m/e=159$ , corresponding to H atom elimination. The photofragment translational energy distributions, as shown in Figs. 4(b) and 4(d), suggest that the dissociation occurs from the repulsive excited state. Since the amino group ( $NH_2$ ) is also an absorption chromophore in this UV region,<sup>15,16,17</sup> a large translational energy release can occur from amino group or NH group of the indole ring. The relative ion intensities of the disklike image and line shape image of  $m/e=130$  are 3:1 and 1:1 at 248 and 193 nm, respectively. It suggests that the internal conversion to the ground state prior to dissociation is important in tryptamine.

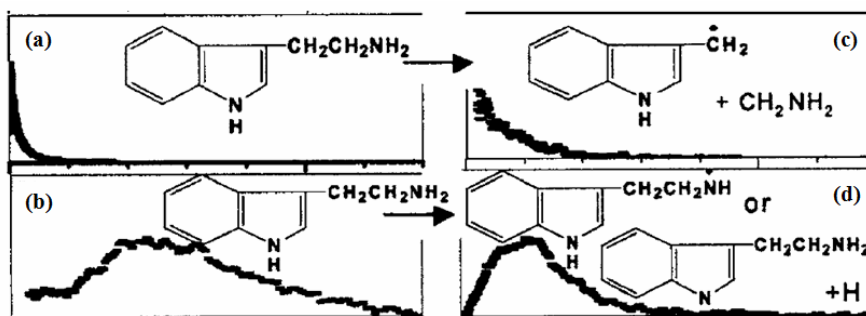


Fig. 4 The photofragment translational energy distribution (a)  $C_8NH_6CH_2CH_2NH_2 + hv (248 \text{ nm}) \rightarrow C_8NH_6CH_2 + CH_2NH_2$  (b)  $C_8NH_6CH_2CH_2NH_2 + hv (248 \text{ nm}) \rightarrow C_8NH_6CH_2CH_2NH + H$  or  $C_8NH_5CH_2CH_2NH_2 + H$  (c)  $C_8NH_6CH_2CH_2NH_2 + hv (193 \text{ nm}) \rightarrow C_8NH_6CH_2 + CH_2NH_2$  (d)  $C_8NH_6CH_2CH_2NH_2 + hv (193 \text{ nm}) \rightarrow C_8NH_6CH_2CH_2NH + H$  or  $C_8NH_5CH_2CH_2NH_2 + H$

#### IV. The photodissociation of tryptophan at 248 nm and 193 nm

Tryptamine (50%) was found in tryptophan molecular beam due to the thermal decomposition of tryptophan in the oven. Fragment ions with  $m/e=130$ , 74, and 30 were found at both 193 and 248 nm. Fragment ions with  $m/e=30$  and part of  $m/e=130$  were from dissociation of tryptamine. Fragment ions with  $m/e=74$  and part of  $m/e=130$  result from dissociation of tryptophan, corresponding to the reaction  $C_8NH_6CH_2CHNH_2COOH \rightarrow C_8NH_6CH_2 + CHNH_2COOH$ .

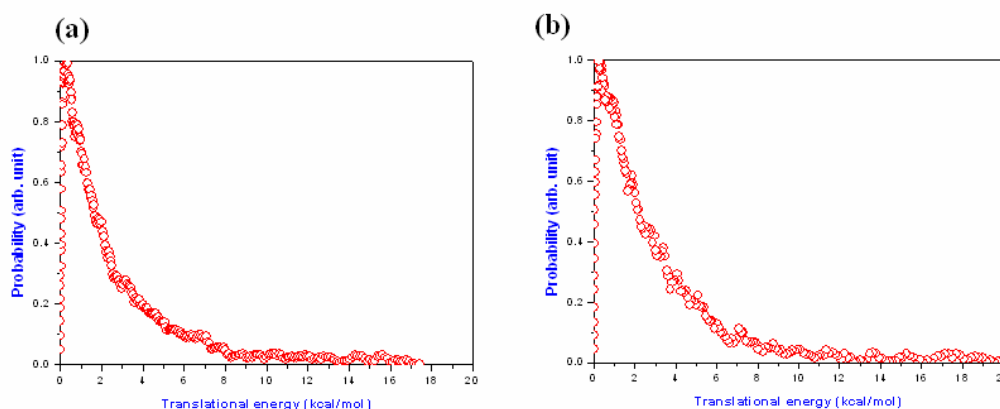


Fig. 5 The photofragment translational energy distribution (a)  $C_8NH_6CH_2CHCOOHNH_2 + hv (248 \text{ nm}) \rightarrow C_8NH_6CH_2 + CHCOOHNH_2$  (b)  $C_8NH_6CH_2CHCOOHNH_2 + hv (193 \text{ nm}) \rightarrow C_8NH_6CH_2 + CHCOOHNH_2$

#### Discussions

Comparison of these four amino acid chromophores reveals unique side chain

size-dependent dissociation properties. UV photoexcitation of the indole ring results in an excited state that is stable with respect to dissociation. Dissociation must occur indirectly, either through coupling of the stable state with the repulsive state ( $\pi\sigma^*$ ) or after internal conversion from an excited electronic state to the ground electronic state. Branching ratios between dissociation on the repulsive potential and dissociation on the ground electronic state depend on the competition between the two nonradiative transitions, the transition from  $\pi\sigma^*$  to  $\pi\pi^*$  and from  $\pi\pi^*$  to the ground state. The rate constant  $k$  for radiationless transition between a pair of states depends on two factors. One is the overlap of wavefunctions and energy mismatch, which can be described by Fermi's golden rule,

$$k_{i \rightarrow f} = \frac{2\pi}{\hbar} \langle \Psi_f | H | \Psi_i \rangle^2 \rho_e.$$

$H$  is the perturbation operator,  $\Psi_i$  and  $\Psi_f$  are the respective wave functions for the initial and final states, and  $\rho_e$  is the density of states and is given by the number of energy levels per energy unit in the final state at the energy of the initial state. The other factor is the accessibility of conical intersections. As the chromophores in our study vary from indole to tryptophan, the respective side chains for these molecules increase. Because floppy side chains contain a large number of low vibrational frequency modes, the density of states increases rapidly. The estimation of the density of states shows that the increase in the density of states for the ground state is larger than that for the repulsive state at the photoexcitation energy level.<sup>18</sup> This is due to the large energy separation between the ground and repulsive states. As a consequence, the increase in the radiationless transition rate between  $\pi\pi^*$  and ground electronic state due to the overlap of wave functions and energy mismatch is far greater than that between  $\pi\pi^*$  and  $\pi\sigma^*$ . Meanwhile, internal conversion is very efficient through conical intersections. As the size of floppy side chain increases, it may introduce more conical intersections. These conical intersections not only increase both  $\pi\pi^*$  to  $S_0$  and  $\pi\pi^*$  to  $\pi\sigma^*$  radiationless transitions, but also increase the  $\pi\sigma^*$  to  $S_0$  radiationless transition if molecules are in the  $\pi\sigma^*$  state. If molecules go to the potential well of the ground state through some conical intersections between  $\pi\pi^*$  and  $S_0$ , energy is randomized prior to dissociation. The dissociation rate or kinetic energy release are the same as those from direct internal conversion or through conical intersection from  $\pi\pi^*$  to  $S_0$ . As a result, large amino acid chromophores are much easier to end up in the ground state through various internal conversion pathways and energy is randomized prior to dissociation. Dissociation from the excited state for these large chromophores is completely quenched. Similar side chain size-dependent dissociation properties have been found in the other smaller amino



acid chromophores.<sup>19</sup> Although under collisionless conditions, molecules upon absorbing UV photons eventually dissociate into fragments, either from an excited state or the ground state, dissociation on the ground state is slow and therefore it can be easily quenched in the condensed phase due to rapid intermolecular energy transfer. Our results show that large chromophores only dissociate on the ground state. This provides a mechanism for the photostability of amino acids in the condensed phase.

## References

- <sup>1</sup> M. B. Robin, *Higher Excited States of Polyatomic Molecules* \_Academic, New York(1972).
- <sup>2</sup> P. R. Callis, *Annu. Rev. Phys. Chem.* **34**, 329 (1983).
- <sup>3</sup> D. Creed, *Photochem. Photobiol.* **39**, 537 (1984).
- <sup>4</sup> C. E. Crespo-Hernandez, B. Cohen, P. M. Hare, and B. Kohler, *Chem. Rev. (Washington, D.C.)* **104**, 1977(2004).
- <sup>5</sup> A. L. Sobolewski and W. Domcke, *Chem. Phys.* **259**, 181 (2000).
- <sup>6</sup> A. L. Sobolewski and W. Domcke, *J. Phys. Chem. A* **105**, 9275 (2001).
- <sup>7</sup> A. L. Sobolewski, W. Domcke, C. Dedonder-Lardeux, and C. Jouvet, *Phys. Chem. Chem. Phys.* **4**, 1093 (2002).
- <sup>8</sup> B. O. Roos, P. A. Malmqvist, V. Molina, L. Serrano-Andres, and M. Merchan, *J. Chem. Phys.* **116**, 7526 (2002).
- <sup>9</sup> Z. G. Lan, W. Domcke, V. Vallet, A. L. Sobolewski, and S. Mahapatra, *J. Chem. Phys.* **122**, 224315 (2005).
- <sup>10</sup> C. M. Tseng, Y. T. Lee, and C. K. Ni, *J. Chem. Phys.* **121**, 2459 (2004).
- <sup>11</sup> (a)M. F. Lin, C. M. Tseng, Y. T. Lee, and C. K. Ni, *J. Chem. Phys.* **123**, 124303 (2005); (b)M. G. D. Nix, A. L. Devine, A. L. B. Cronin, and M. N. Rashfold, *Phys. Chem. Chem. Phys.* **8**, 2610 (2006).
- <sup>12</sup> M. N. R. Ashfold, B. Cronin, A. L. Devine, R. N. Dixon, and M. G. D. Nix, *Science* **312**, 1637 (2006).
- <sup>13</sup> M. G. D. Nix, A. L. Devine, B. Cronin, R. N. Dixon, and M. N. R. Ashfold, *J. Chem. Phys.* **125**, 133318 (2006).
- <sup>14</sup> A. L. Devine, B. Cronin, M. G. D. Nix, and M. N. R. Ashfold, *J. Chem. Phys.* **125**, 184302 (2006).
- <sup>15</sup> J. Biesner, L. Schnieder, G. Ahlers, X. Xie, K. H. Welge, M. N. R. Ashfold, and R. N. Dixon, *J. Chem. Phys.* **91**, 2901 (1989).
- <sup>16</sup> G. C. G. Waschewsky, D. C. Kitchen, P. W. Browning, and L. J. Butler, *J. Phys. Chem.* **99**, 2635 (1995).
- <sup>17</sup> C. M. Tseng, Y. A. Dyakov, C. L. Huang, A. M. Mebel, S. H. Lin, Y. T. Lee, and C. K. Ni, *J. Am. Chem. Soc.* **126**, 8760 (2004)

- 
- <sup>18</sup> P. J. Robinson and K. A. Holbrook, *Unimolecular Reaction* \_Wiley, New York(1972).
- <sup>19</sup> C. M. Tseng, Y. T. Lee, C. K. Ni, and J. L. Chang, *J. Phys. Chem. A.*, **111**, 6674(2007).



## Chapter 8. The relevance of tryptophan photodissociation in a molecular beam and the origin of life on earth

### Abstract

Photodissociation dynamics of L-tryptophan was studied at 193 or 213 nm using multimass ion imaging techniques. The competition between internal conversion to the ground electronic state and dissociation from the repulsive excited state was investigated. The ground state dissociation at both wavelengths is the only one channel and the dissociation rate has been measured. The suggestion of the importance of L-tryptophan in condensed phase has been made.

### Introduction

It is a long-standing and still an open problem to determine the origin of biomolecular homochirality, that is, to explain why essentially all amino acids in proteins are L, while all sugars (riboses and deoxy-riboses) in RNA and DNA are D. Many scenarios have been envisaged to explain this homochirality. All scenarios involve at least two steps: the first step is the creation of an enantiomeric excess (e.e.) from a racemic mixture of the considered chiral molecule. This step is the most debated one. The e.e. might stem from an asymmetric adsorption on chiral mineral surfaces like quartz or clays<sup>1</sup>, from the consequences at the molecular level of the violation of parity in the weak interaction<sup>2,3</sup> (the so-called Vester-Ulbricht hypothesis), from a spontaneous resolution<sup>4,5</sup>, or from asymmetric photoreactions<sup>6,7</sup>. In all these cases, the e.e. generated among chiral molecules is very low (from 0.001% to about 10% in the best cases). For this reason, a second step is needed, namely the amplification of the e.e. from low values to high values (up to 99.5%, see Ref. 8. Soai *et al.*<sup>8</sup>). Interestingly, it seems that the chiral initiator may be the molecule itself but also another chiral molecule<sup>9</sup>. A recent review of these processes is provided by Podlech<sup>10</sup>.

Numerous asymmetric mechanisms have been suggested and tested experimentally, including the influence of circularly polarized light (CPL) as an external chiral force.<sup>11,12,13</sup> Astronomical sources of CPL,<sup>14,15</sup> which might produce enantiomeric selection in interstellar organic molecules, were observed in the IR range.<sup>16</sup> Moreover, gas chromatographic–mass spectral analyses of the four stereoisomers of 2-amino-2,3-dimethylpentanoic acid (DL- $\alpha$ -methylisoleucine and

DL-a-methylalloisoleucine) obtained from the Murchison meteorite show that the L enantiomer occurs in excess (7.0 and 9.1%, respectively) in both of the enantiomeric pairs.<sup>17</sup>

It is found that the circular dichroism (CD) band of tryptophan centered at 210 nm (stemming from the carboxyl chromophore) is concealed by bands with opposite sign at 193 nm (stemming from other chromophores, i.e. benzene ring, in the case of tryptophan).<sup>18</sup> It suggests L tryptophan has larger absorption coefficient at 193 nm for right circular polarized light and D tryptophan has larger absorption coefficient at 213 nm for the same circular polarized light. The speculation has risen: if there two electronic states have different dissociation efficiency, they may result in an enantiomeric excess (e.e.) from a racemic mixture. Since the new design of non-metallic oven is able to produce a sufficient concentration of tryptophan in molecular beam. The photodissociation experiment of tryptophan at 193 nm and 213 nm has been carried out in this chapter. The relevance to the origin of homochirality of amino acid has been discussed.

## Experimental

The experimental techniques have been described in chapter 2 and only a brief description is given here. Basically molecules in a molecular beam were photodissociated by a pulsed UV laser beam at 193 or 213 nm, then photofragments were ionized by vacuum UV (VUV) laser at 118nm or 157 nm. The masses of fragments were identified along with their translational energy distributions using multimass ion imaging techniques. A homemade high temperature nozzle was used in this experiment. It is the non-metallic oven as described in chapter 2. Ultrapure He (or Ne) at a pressure of 400 Torr flowed through the oven and the sample/rare gas mixture was expanded through the exit port of the oven to form molecular beam. VUV photoionization and time-of-flight mass spectra were used to check the content of the molecular beam before the photodissociation experiment was performed. In order to generate 212.8 nm laser, the mixing of the 355 nm and 512 nm from single Nd:YAG laser in BBO crystal has been used, as shown in Fig. 1.

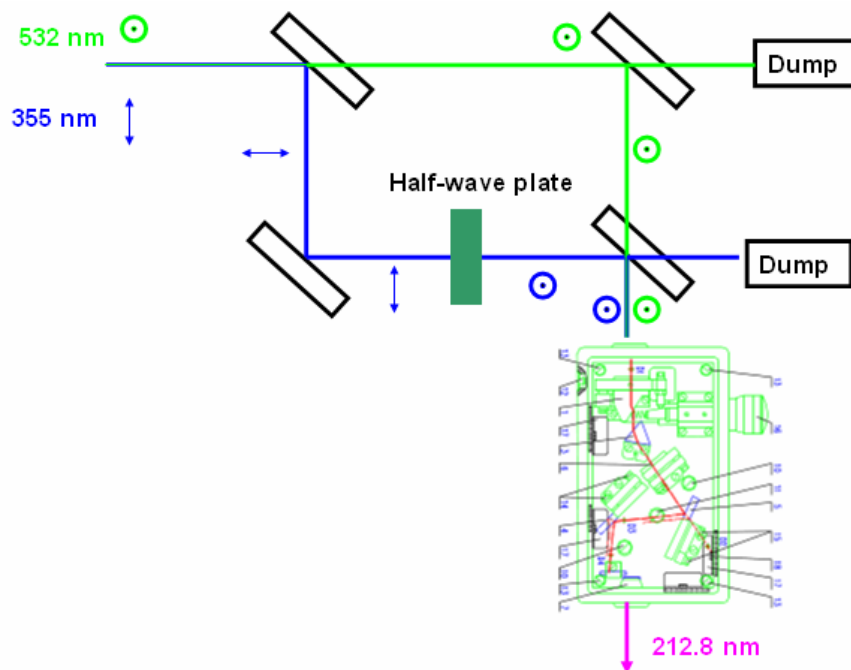


Fig. 1. The generation of 212.8 nm laser---fifth harmonic generation of Nd: YAG laser. ↔ or ↑ means that the laser polarization is parallel to the plane. ⊙ means that the laser polarization is perpendicular to the plane. A half wave plate was used to rotate the polarization of 355 nm laser.

## Results and discussions

Figure 2 depicts the photofragment ion images obtained from the photodissociation of tryptophan at 193 nm. Fragments of  $m/e = 130$ , 74 were observed. Fragments of  $m/e = 130$  and 74 correspond to  $C_8NH_6CH_2$  and  $CHCOOHNH_2$  radicals from C-C bond cleavage,  $C_8NH_6CH_2CHCOOHNH_2 \rightarrow C_8NH_6CH_2 + CHCOOHNH_2$ . The images of fragment  $m/e= 130$  and 74 are mainly line-shape. Comparison of the momentum distributions between  $m/e=130$  and the sum of  $m/e=74$  confirms this dissociation channel.

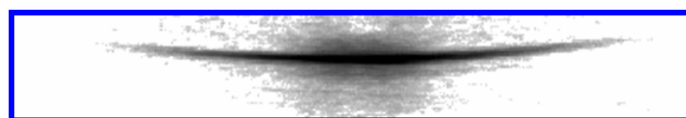


Figure 2. The ion image for  $m/e = 74$  at 20  $\mu s$  pump-probe delay time with 193 nm laser excitation

The translational energy distribution of C-C bond cleavage,  $\text{C}_8\text{NH}_6\text{CH}_2\text{CHCOOHNH}_2 \rightarrow \text{C}_8\text{NH}_6\text{CH}_2 + \text{CHCOOHNH}_2$ , is illustrated in Fig. 3.

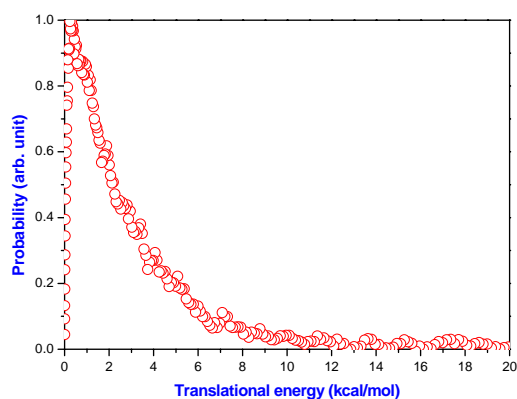
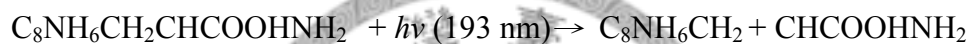


Fig. 3. The photofragment translational energy distribution



The ion images of C-C bond cleavage at 212.8 nm are illustrated in Fig. 4. Photodissociation of tryptophan at 212.8 nm shows similar dissociation channel. The translational energy distributions at 212.8 nm show one components, as shown in Fig. 5.



Figure 4. The ion image for  $m/e = 74$  at 20  $\mu\text{s}$  pump-probe delay time with 212.8 nm laser excitation

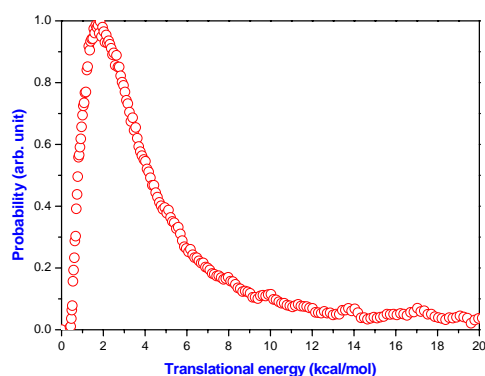
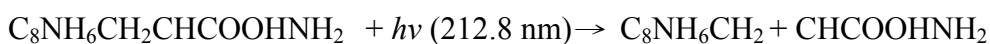


Fig. 5 The photofragment translational energy distribution



The photofragment translational energy distribution indicates the ground dissociation mechanism at both wavelengths. No fast component was observed, which suggests the internal conversion in tryptophan at both wavelengths is major deactivation channel after UV irradiation. The product build-up curve has been measured at both wavelengths, as shown in Fig. 6.

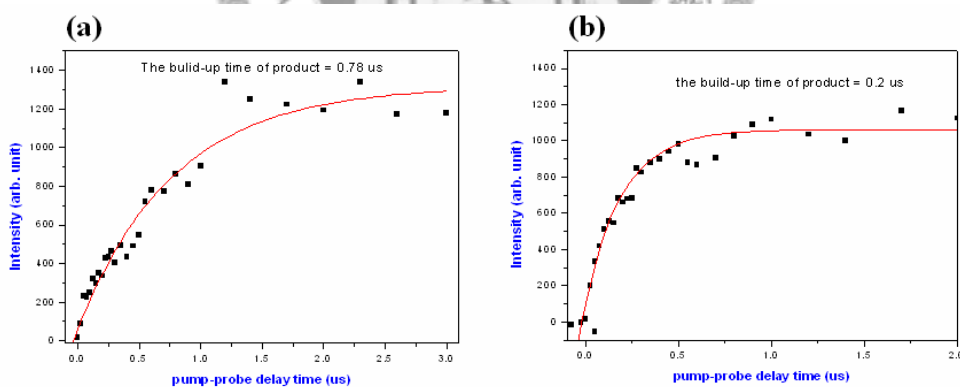


Fig. 6 The product build-up curve by changing the pump-probe delay time at different pump wavelength (a) 212.8 nm and (b) 193 nm.

The curves are fitted a single exponential growth: the dissociation rates obtained from these curve are  $5 \times 10^6 \text{ s}^{-1}$  and  $1.28 \times 10^6 \text{ s}^{-1}$  at 193 nm and 212.8 nm, respectively. The difference is only about a factor of four. Compared with the available energy (78 kcal/mol and 64 kcal/mol at 193 nm and 212.8 nm, respectively),

the difference is only about a factor of four.

The results show there is no significant difference in dissociation mechanism at these two wavelengths. The four times difference of dissociation rate is not enormous, but it is still a possible origin of the homochirality of life on earth in the billion years of evolution. Amino acids have been synthesized in simulated interstellar ice in the laboratory.<sup>19</sup> Dissociation could occur in the interstellar ice grain or comets. A future challenge is to find out the dissociation dynamics of amino acid in the simulated condition by measuring the dissociation yield and identification of photoproducts.

## References

---

- <sup>1</sup> Hazen, R. M., *Scientific American* **284**, 77(2001).
- <sup>2</sup> Bonner, W. A. *Origins Life Evol. Biosph.* **21**, 59(1991).
- <sup>3</sup> Bonner, W. A.: 2000, *Chirality*, **12**, 114(2000).
- <sup>4</sup> Avalos, M., Babiano, R., Cintas, P., Jiménez, J. L. and Palacios, J. C., *Chem. Commun.* **11**, 887(2000).
- <sup>5</sup> saghatelian, A., Yokobayashi, Y., Soltani, K. and Ghadiri, M. R., *Nature* **409**, 797(2001).
- <sup>6</sup> Buchardt, O., *Angew. Chem. Internat.Edit.*, **13**, 179(1974).
- <sup>7</sup> Rau, H., *Chem. Rev.*, **83**, 535(1983).
- <sup>8</sup> Soai, K., Shibata, T. and Sato, I., *Acc. Chem. Res.* **33**, 382(2000).
- <sup>9</sup> Shibata, T., Yamamoto, J., Matsumoto, N., Yonekubo, S., Osanai, S. and Soai, J. *Am. Chem. Soc.* **120**, 12157(1998).
- <sup>10</sup> Podlech, J.: 2001, *Cell. Mol. Life Sci.* **58**, 44(2001).
- <sup>11</sup> O . Burchardt, *Angew. Chem.*, **86**, 222 (1974).
- <sup>12</sup> A. G. Griesbeck, U. J. Meierhenrich, *Angew. Chem.*, **114**, 3279(2002).
- <sup>13</sup> U . J. Meierhenrich, W. H.-P. Thiemann, *Origins Life Evol. Biosphere*, **34**, 111(2004).
- <sup>14</sup> S . F. Mason, *Nature*, **389**, 804(1997).
- <sup>15</sup> C . Cerf, A. Jorissen, *Space Sci. Rev.*, **92**, 603(2000).
- <sup>16</sup> J . Bailey, A. Chrysostomou, J. H. Hough, T. M. Gledhill, A. McCall, S. Clark, F. MNnard, M. Tamura, *Science*, **281**, 672 (1998).
- <sup>17</sup> John R. Cronin and Sandra Pizzarello, *Science*, **275**, 951(1997).
- <sup>18</sup> Yash P. Myer, Lawrence H. MacDonald, *J. Am. Chem. Soc.* **89**, 7142(1967).
- <sup>19</sup> (a)G . M. MuKoz Caro, U. J. Meierhenrich, W. A. Schutte, B. Barbier, A. Arcones Segovia, H. Rosenbauer, W. H.-P. Thiemann, A. Brack, J. M. Greenberg, *Nature*, **416**, 403(2002). (b)M. P. Bernstein, J. P. Dworkin, S. A. Sandford, G.W. Cooper, L.



---

J. Allamandola, Nature, **416**, 401(2002).



## Chapter 9. The photodissociation of N-methylindole, N-methylpyrrole, and anisole

### Abstract

Photodissociation of N-methylindole, N-methylpyrrole, and anisole at 193 and 248 nm in a molecular beam has been studied in separate experiments using multimag ion imaging techniques. CH<sub>3</sub> elimination was found to be the only dissociation channel for these molecules at both wavelengths. The photofragment translational energy distribution of anisole contains a fast and a slow component at both wavelengths, corresponding to the dissociation from the repulsive excited state and the ground electronic state, respectively. On the other hand, fast component is dominant for N-methylindole at 248 nm, and only the slow component was observed at 193 nm. The absorption coefficient of N-methylpyrrole is too weak to study at 248 nm, but the photofragment translational energy distribution at 193 nm includes a large portion of slow component and a small portion of fast component. A comparison with the photodissociation dynamics of phenol, pyrrole, and indole has been made.

### Introduction

One important photophysical characteristic of aromatic biomolecules is their low fluorescence quantum yields upon excitation by ultraviolet (UV) light<sup>1,2,3,4</sup>. Such behavior indicates the presence of fast nonradiative channel that efficiently quenches the fluorescence. This nonradiative process is assumed to be the ultrafast internal conversions (IC) to the ground electronic state. The so-called “photostability” for these molecules can prevent undesirable photochemical reactions from initiating after UV irradiation<sup>2-3</sup>. However, recent theoretical calculations have pointed out that excited electronic states of  $1\pi\sigma^*$  play an important role in the photochemistry of aromatic biomolecules, in particular those containing hydroxy and azine groups like phenol, indole and pyrrole.<sup>5</sup> For indole, the first excited  $1\pi\pi^*$  state is bound with respect to N-H bond distance, but the  $1\pi\sigma^*$  state is repulsive. The diabatic  $1\pi\sigma^*$  potential correlates with the ground state products, C<sub>8</sub>NH<sub>6</sub> + H. Although the absorption of UV photons corresponds to excitation to the  $1\pi\pi^*$  excited state, population of the  $1\pi\pi^*$  state can be transferred to the  $1\pi\sigma^*$  potential through a conical intersection. As a consequence, instead of direct internal conversion to the ground electronic state, dissociation from  $1\pi\sigma^*$  provides an alternate explanation for the rapid fluorescence quenching. Similar repulsive potential energy surfaces of  $1\pi\sigma^*$  were found for phenol along O-H bond and pyrrole along N-H bond. The only difference is that the  $1\pi\pi^*$

potential minima in both indole and phenol lie below that of the  $1\pi\sigma^*$  PES (in the area near equilibrium geometry at the ground electronic state), whereas in pyrrole the  $1\pi\sigma^*$  state is lowest in energy.

Evidences to support the theoretical calculation were found in early and recent experimental results. Photofragment translational spectroscopy was used to study the photodissociation of pyrrole at 193 and 248 nm under collision-free conditions. In addition to some ring opening dissociation channels, cleavage of the N-H bond on the repulsive electronically excited state of pyrrole was observed before the theoretical prediction.<sup>6</sup> Recent H atom photofragment velocity map ion imaging and H Rydberg atom high resolution translational spectroscopy disclosure more detail information of the H atom elimination channel and supports the theoretical calculation.<sup>7</sup> H atom elimination on the repulsive excited state of phenol and indole was first observed using multimass ion imaging/molecular beam experiment.<sup>8,9</sup> Recent H Rydberg atom high resolution translational spectroscopy further reveals the detail dissociation mechanism and vibrational mode dependence.<sup>10</sup>

The dissociation mechanism may change as the H atom is replaced by a methyl group. For example, difference of delayed luminescence between N-methylindole and indole in the gas phase with the laser irradiation wavelengths of 266 nm and 230-250 nm has been reported.<sup>11</sup> Delayed annihilation fluorescence which spectrally matches fast fluorescence was observed for N-methylindole. However, there is no similar fluorescence for indole. Instead, a delayed luminescence band with wavelength at the maximum 535 nm was observed, which was interpreted as luminescence of free radicals formed as a result of dissociation of the N-H bond of indole. No free radical from the dissociation of the N-C bond of N-methylindole was observed.

On the other hand, anisole seems to have the same dissociation mechanism as that of phenol. Photodissociation of anisole has been studied at 193 nm in the gas phase.<sup>12</sup> Transient absorption spectra in the range of 210-300 nm shows two broad bands and which were assigned to phenoxy radical. The phenoxy radicals are produced in the time range of shorter than 1 ns on irradiation with the ArF laser light. The photodissociation mechanism was proposed to be predissociation. On the other hand, both phenoxy radicals and phenoxyethyl radical were observed from the transient absorption spectrum of anisole in acetonitrile at 248-nm laser photolysis.<sup>13</sup>

The photophysics of jet-cooled N-methylpyrrole molecules following excitation to their first excited singlet state (242.7~237 nm) has been investigated by resonance enhanced multiphoton ionization spectroscopy/velocity map imaging of  $\text{CH}_3$  photoproducts.<sup>14</sup> Direct dissociation on repulsive excited potential energy surface

yields fast CH<sub>3</sub> fragments, but this product channel is only observed in a narrow wavelength range near the absorption band origin. Slow CH<sub>3</sub> fragments were observed at all the photolysis wavelengths. These slow products are attributed to dissociation of highly vibrationally excited ground state molecules formed by radiationless transfer from the excited state.

In this work, we study the photodissociation of N-methylindole, N-methylpyrrole, and anisole using multimass ion imaging techniques. Comparison to previous studies was made.

## Experimental

The experimental techniques have been described in chapter 2 and only a brief description is given here. Vapor of each compound was formed by flowing ultrapure He at pressure of 400 Torr through a reservoir filled with liquid or solid sample at 50 °C. The compound/He mixture was then expanded through an 800 μm high temperature (70°C) pulsed nozzle to form the molecular beam. Molecules in the molecular beam were photodissociated by an UV photolysis laser pulse (Lambda Physik Compex 205; pulse duration: ~20 ns). Basically molecules in a molecular beam were photodissociated by a pulsed UV laser beam at 193 or 248 nm, then photofragments were ionized by vacuum UV (VUV) laser at 118 nm. The masses of fragments were identified along with their translational energy distributions using multimass ion imaging techniques.

## Results and discussions

### I. Anisole

Figure 1 depicts the photofragment ion images obtained from the photodissociation of anisole at 193 nm. Fragments of  $m/e = 93$ , 65, and 15 were observed. The study of photolysis laser power dependence in the region of  $0.15\text{mJ/cm}^2 \sim 0.87\text{ mJ/cm}^2$  showed that they were from one-photon dissociation. Fragments of  $m/e = 93$  and 15 correspond to C<sub>6</sub>H<sub>5</sub>O and CH<sub>3</sub> radicals from C-O bond cleavage  $\text{C}_6\text{H}_5\text{OCH}_3 \rightarrow \text{C}_6\text{H}_5\text{O} + \text{CH}_3$ . The image of fragment  $m/e=65$  is mainly a disk-like image and superimposed with a line shape image. It is from the dissociative ionization of phenoxy radical by VUV photoionization due to the excess VUV photon energy  $\text{C}_6\text{H}_5\text{O} + h\nu(118\text{nm}) \rightarrow \text{C}_5\text{H}_5^+ + \text{CO}$ . This cracking pattern has been observed from the photoionization of phenoxy radical generated from the photodissociation of phenol.<sup>15</sup> Comparison of the momentum distributions between

m/e=15 and the sum of m/e=93 and 65 confirms this dissociation channel.

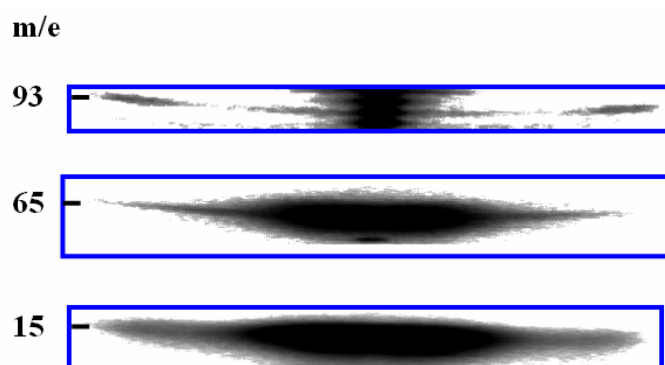


Figure 1. The ion image for m/e = 93, 65 and 15 at 15  $\mu$ s, 15 $\mu$ s and 0.7 $\mu$ s pump–probe delay time, respectively, with 193 nm laser excitation

The translational energy distribution of CH<sub>3</sub> elimination is illustrated in Fig. 2.

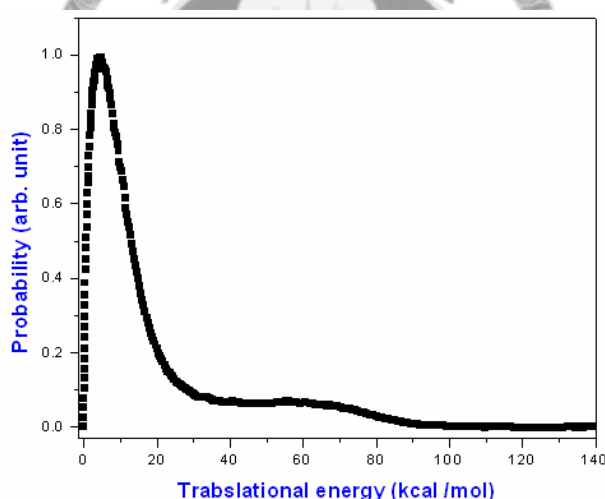
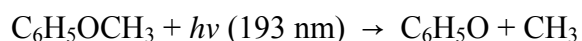


Figure 2. Photofragment translational energy distribution of reaction



The ion images of CH<sub>3</sub> elimination at 248 nm are illustrated in Fig. 3. Photodissociation of anisole at 248 nm shows similar dissociation channel and fragment cracking pattern. The translational energy distributions at 248nm show two components, as shown in Fig. 4. These components are the fragments that resulted from the dissociation of anisole with large recoil velocity and small recoil velocity,

respectively.

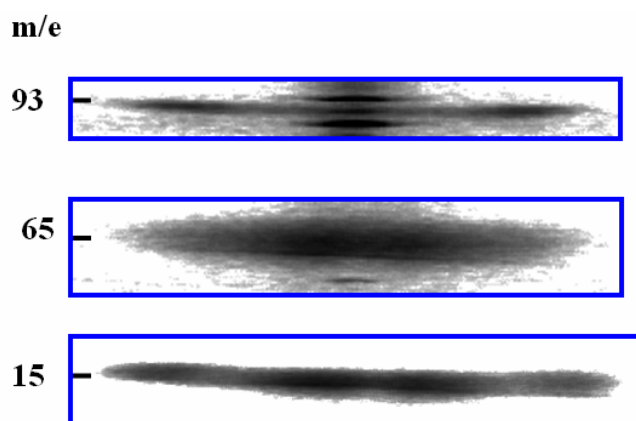


Figure 3. The ion image for  $m/e = 93$ , 65 and 15 at 14  $\mu\text{s}$ , 14 $\mu\text{s}$  and 2  $\mu\text{s}$  pump–probe delay time, respectively, with 248 nm laser excitation

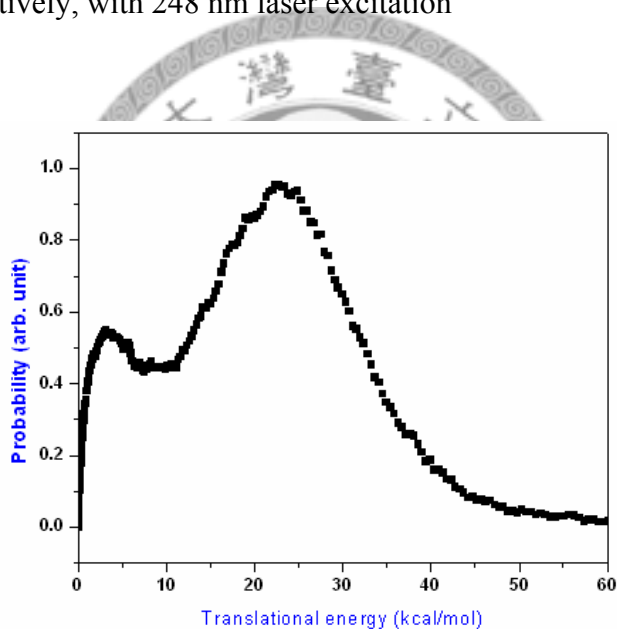
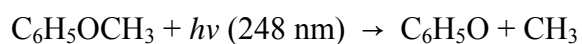


Figure 4. Photofragment translational energy distribution of reaction



For the slow component, the monotonic decrease of the probability with the increasing translational energy is the typical characteristic of dissociation from a molecule undergoes internal conversion to the ground electronic state with small or no exit barrier. On the other hand, the fast component is the characteristic of dissociation from a repulsive excited state, or dissociation from an electronic state with an exit barrier.

The photodissociation of phenol at 193 and 248 nm has been studied using multimass ion-imaging techniques and step-scan time-resolved Fourier-transform spectroscopy.<sup>15</sup> The major dissociation channels at 193 nm include cleavage of the O-H bond, elimination of CO, and elimination of H<sub>2</sub>O. Only the former two channels are observed at 248 nm. The translational energy distribution shows that H-atom elimination occurs in both the electronically excited and ground states, but elimination of CO or H<sub>2</sub>O only occurs in the electronic ground state.

Comparison between anisole and phenol shows similarities and differences. First, dissociation on the repulsive excited state is observed from both molecules. It indicates the properties of the repulsive excited  $\pi\sigma^*$  state and the coupling between the bound state and the  $\pi\sigma^*$  state do not change very much as H atom in hydroxy group is replaced by the CH<sub>3</sub> group. Dissociation from the repulsive state still remains. Second, the only dissociation of anisole on the ground state is CH<sub>3</sub> elimination. On the other hand, phenol shows various dissociation channels on the ground state. C<sub>6</sub>H<sub>5</sub>O-CH<sub>3</sub> bond energy (64 kcal/mol) smaller than C<sub>6</sub>H<sub>5</sub>O-H bond energy (88 kcal/mol) is one reason that O-C bond cleavage is the dominant channel for anisole. The other reason is that the migration of H atom from hydroxy group to aromatic ring is the first step for CO elimination channel in phenol. The corresponding step for anisole becomes the CH<sub>3</sub> migration. This step becomes impossible due to the large barrier height. As a result, CH<sub>3</sub> elimination becomes the only dissociation channel for anisole.

## II. N-methylpyrrole

The first electronic excited state is located at  $\sim 241$  nm. Transitions to and from this state were shown to give rise to the structured bands observed around 240 nm.<sup>16</sup> The absorption coefficient of N-methylpyrrole at 248 nm is too small to study. Therefore, we only study the photodissociation at 193 nm.

Figure 5 depicts the photofragment ion images obtained from the photodissociation of N-methylpyrrole at 193 nm. Fragments of  $m/e = 66$  and 15 were observed. The study of photolysis laser power dependence in the region of  $0.08 \text{ mJ/cm}^2 \sim 0.67 \text{ mJ/cm}^2$  showed that they were from one-photon dissociation. Fragments of  $m/e = 66$  and 15 correspond to C<sub>4</sub>NH<sub>4</sub> and CH<sub>3</sub> radicals from N-C bond cleavage  $\text{C}_4\text{NH}_4\text{CH}_3 \rightarrow \text{C}_4\text{NH}_4 + \text{CH}_3$ . The translational energy distribution of this channel is shown in Fig. 6. It includes a large portion of slow component and a small portion of fast component.

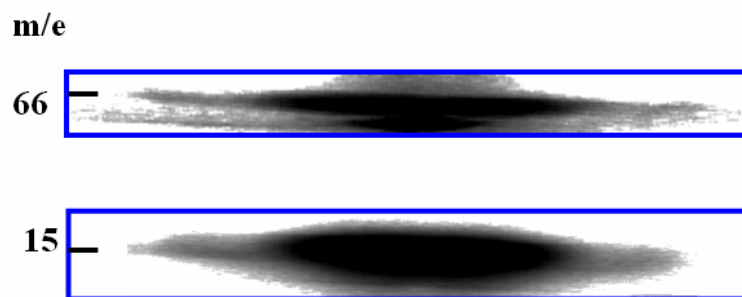


Figure 5. The ion image for  $m/e = 66$  and  $15$  at  $8\mu\text{s}$  and  $0.3\mu\text{s}$  pump–probe delay time, respectively, with  $193\text{ nm}$  laser excitation

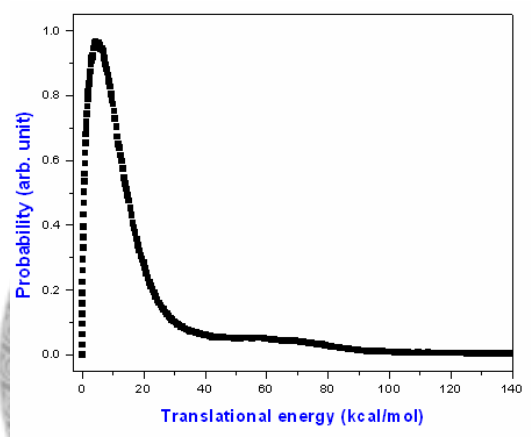
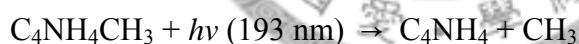


Figure 6. Photofragment translational energy distribution of reaction



Photofragment translational energy spectroscopy has been used to study the photodissociation of pyrrole at  $193\text{ nm}$  and  $248\text{ nm}$  under collision free conditions.<sup>6</sup> Five primary dissociation channels were observed at  $193\text{ nm}$ . Two channels resulted from the cleavage of N-H bond with one channel following the internal conversion to the ground state and the other originating from electronically excited pyrrole. Another two dissociation channels involved HCN elimination producing vinylmethylene and cyclopropene, respectively. The last channel involved IC to the ground state followed by ring opening and N-C bond cleavage to form  $\text{NH} + \text{CCHCCH}_2$ .

Unlike the observation of ring opening dissociation in pyrrole, no similar dissociation channel was observed in N-methylpyrrole. Only the cleavage of N-C bond with the majority from the internal conversion to the ground state and the



minority from electronically excited state. The reason that there are no analogous ring opening dissociation channels is similar to that of phenol and anisole, i.e., the ring opening dissociation in pyrrole requires the migration of H atom from N-H group to start the process. Replacement of H atom by CH<sub>3</sub> group simply hinder the ring opening dissociation channels. Previous study in the region of 242.7~237 nm shows that dissociation from the excited state was only observed in a narrow wavelength range near the absorption band origin. Our results show that dissociation from excited state still can be observed at 193 nm, although it is a minor channel.

### III. N-methylindole

Fragments of  $m/e = 116$  and  $15$  were observed from photodissociation of N-methylindole at 193 nm. Figure 7 illustrates the photofragment ion images. The study of photolysis laser power dependence in the region of  $0.1 \text{ mJ/cm}^2 \sim 0.67 \text{ mJ/cm}^2$  showed that they were from one-photon dissociation. The match of the momentum distribution between these two fragments suggests they come from the same dissociation channel:  $\text{C}_8\text{NH}_6\text{CH}_3 \rightarrow \text{C}_8\text{NH}_6 + \text{CH}_3$ .

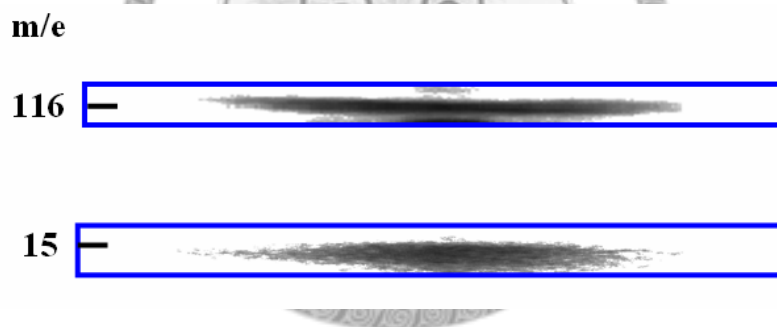


Figure 7. The ion image for  $m/e = 116$  and  $15$  at  $19 \mu\text{s}$  and  $3 \mu\text{s}$  pump-probe delay time, respectively, with 193 nm laser excitation

The photofragment translational energy distribution of this channel is illustrated in Fig. [8](#).

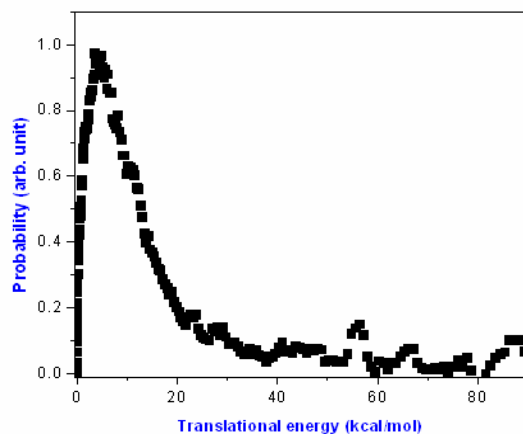
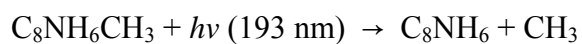


Figure 8. Photofragment translational energy distribution of reaction



Photodissociation of N-methylindole at 248 nm shows the same dissociation channel. Figure 9 illustrates the photofragment ion images. The translational energy distribution obtained at 248 nm is shown in Fig. 10.

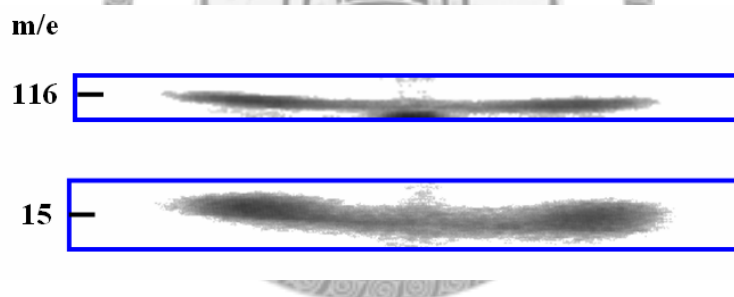


Figure 9. The ion image for  $m/e = 116$  and  $15$  at  $20 \mu\text{s}$  and  $2 \mu\text{s}$  pump-probe delay time, respectively, with 248 nm laser excitation

The translational energy distributions at both wavelengths show only fast component, indicating the dissociation from the repulsive excited state.

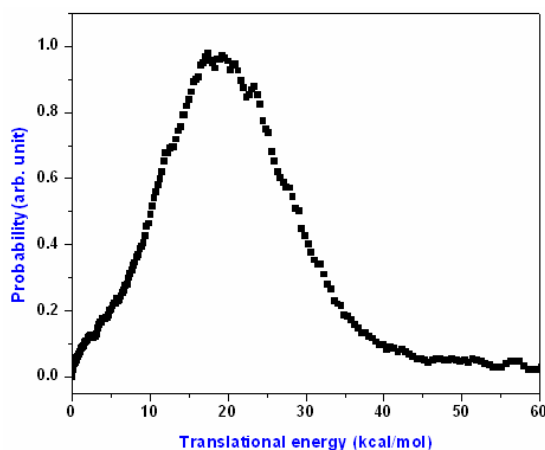
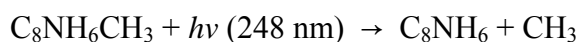


Figure 10. Photofragment translational energy distribution of reaction



Photodissociation of indole at 193 and 248 nm under collision-free conditions has been studied using the same techniques. H atom elimination was found to be the only dissociation channel at both wavelengths. The photofragment translational energy distribution obtained at 193 nm contains a fast and a slow component. 54 % of indole following the 193 nm photoexcitation dissociate from electronically excited state, resulting in the fast component. The rest of 46% indole dissociate through the ground electronic state, giving rise to the slow component. Similar two-component translational energy distribution was observed at 248 nm. However, more than 80% of indole dissociate from electronically excited state after the absorption of 248 nm photons.

Comparison of indole and N-methylindole shows the similar wavelength dependence of the competition between the dissociation on the ground state and the repulsive excited state. As the pump photon energy decreases, internal conversion to the ground state and eventually dissociate into fragments becomes less important. Population transfer from the excited bound state to the repulsive excited state becomes the dominant channels. Our result is in contrast to the conclusion from the delayed luminescence study of N-methylindole and indole.<sup>11</sup>

## References

---

<sup>1</sup> M. B. Robin, *Higher Excited States of Polyatomic Molecules* (Academic, New York,

---

1972).

<sup>2</sup> P. R. Callis, *Annu. Rev. Phys. Chem.* **34**, 329 (1983).

<sup>3</sup> D. Creed, *Photochem. Photobiol.* **39**, 537 (1984).

<sup>4</sup> C. E. Crespo-Hernandez, B. Cohen, P. M. Hare, and B. Kohler, *Chem. Rev.* (Washington, D.C.) **104**, 2004 (1977).

<sup>5</sup> (a) A. L. Sobolewski and W. Domcke, *Chem. Phys.* **259**, 181 (2000). (b) A. L. Sobolewski and W. Domcke, *J. Phys. Chem. A* **105**, 9275 (2001). (c) A. L. Sobolewski, W. Domcke, C. Dedonder-Lardeux, and C. Jouvet, *Phys. Chem. Chem. Phys.* **4**, 1093 (2002). (d) B. O. Roos, P. A. Malmqvist, V. Molina, L. Serrano-Andres, and M. Merchan, *J. Chem. Phys.* **116**, 7526 (2002). (e) V. Vallet, Z. G. Lan, S. Mahapatra, A. L. Sobolewski, and W. Domcke, *Faraday Discuss.* **127**, 283 (2004). (f) Z. G. Lan, W. Domcke, V. Vallet, A. L. Sobolewski, and S. Mahapatra, *J. Chem. Phys.* **122**, 224315 (2005). (g) V. Vallet, Z. G. Lan, S. Mahapatra, A. L. Sobolewski, and W. Domcke, *J. Chem. Phys.* **123**, 144307 (2005). (h) M. Barbatti, M. Vazdar, A. J. A. Aquino, M. Eckert-Maksic, and H. Lischka, *J. Chem. Phys.* **125**, 164323 (2006). (i) I. Frank, and K. Damianos, *J. Chem. Phys.* **126**, 125105 (2007).

<sup>6</sup> D. A. Blank, S. W. North, Y. T. Lee, *Chem. Phys.* **187**, 35 (1994).

<sup>7</sup> (a) J. Wei, y J. Riedel, A. Kuczmann, F. Renth, and F. Temps, *Chem. Chem. Phys.* **5**, 315 (2003). (b) J. Wei, y J. Riedel, A. Kuczmann, F. Renth, and F. Temps, *Faraday Discuss.* **127**, 267 (2004). (c) B. Cronin, M. G. D. Nix, R. H. Q. and M. N. R. Ashfold, *Phys. Chem. Chem. Phys.* **6**, 5031 (2004). (d) B. Cronin, A. L. Devine, M. G. D. Nix and M. N. R. Ashfold, *Phys. Chem. Chem. Phys.* **8**, 3440 (2006). (e) B. Cronin, M. G. D. Nix, A. L. Devine, R. N. Dixon, and M. N. R. Ashfold, *Phys. Chem. Chem. Phys.* **8**, 599 (2006). (f) V. Poterya, V. Profant, M. Farnik, P. Slavicek, and U. Buck, *J. Chem. Phys.* **127**, 064307 (2007).

<sup>8</sup> C. M. Tseng, Y. T. Lee, and C. K. Ni, *J. Chem. Phys.* **121**, 2459 (2004).

<sup>9</sup> M. F. Lin, C. M. Tseng, Y. T. Lee, and C. K. Ni, *J. Chem. Phys.* **123**, 124303 (2005).

<sup>10</sup> (a) M. G. D. Nix, A. L. Devine, B. Cronin, *J. Chem. Phys.* **125**, 133318 (2006). (b) M. G. D. Nix, A. L. Devine, B. Cronin, and M. N. R. Ashfold, *Phys. Chem. Chem. Phys.* **8**, 2610 (2006).

<sup>11</sup> N. A. Borisevich, A. A. Sukhodola, and G. B. Tolstorozhev, *J. Applied Spectrosc.* **74**, 379 (2007).

- 
- <sup>12</sup> Y. Kajii, K. Obi, N. Nkashima, and K. Yoshihara, *J. Chem. Phys.* **87**, 5059 (1987).
- <sup>13</sup> M. Ando, S. Yoshiike, T. Suzuki, T. Ichimura, T. Okutsu, M. Ueda, H. Horiuchi, H. Hiratsuka, A. Kawai, K. Shibuya, *J. of Photochemistry and Photobiology A: Chemistry* **174**, 194 (2005)
- <sup>14</sup> (a) S. T. Tsai, C. K. Lin, Y. T. Lee, and C. K. Ni, *Rev. Sci. Instrum.* **72**, 1963 (2001).  
(b) C. L. Huang, Y. T. Lee, and C. K. Ni, in *Modern Chemical Reaction dynamics: Experiment and Theory*. Edited by K. Liu, and X. Yang, (World Scientific Publisher, Singapore 2004). (c) C. K. Ni and Y. T. Lee, *Int. Rev. Phys. Chem.* **23**, 2187 (2004).
- <sup>15</sup> C. M. Tseng; Y. T. Lee; M. F. Lin; C. K. Ni; S. Y. Liu; Y. P. Lee; Z. F. Xu; M. C. Lin, *J. Phys. Chem. A.* **111**, 9463 (2007).
- <sup>16</sup> R. McDiarmid and X. Xing, *J. Chem. Phys.* **105**, 867 (1996).



## Chapter 10. Photodissociation of DNA base model compounds---7-azaindole, 2-aminopyridine and 8-Hydroxyquinoline

### Abstract

The photodissociation of 7-azaindole, 2-aminopyridine and 8-hydroxyquinoline at 193 and 248nm was studied using multimass ion imaging techniques under collisionless conditions. Only one dissociation channel was observed, i.e. H atom elimination. The translational energy distributions show two components at both wavelengths. The slow component corresponds to the dissociation from the ground electronic state after internal conversion, and the fast component results from the dissociation on the electronic excited state.

### Introduction

More than half century ago the double-helix structure of DNA molecules was proposed by Watson and Crick. They pointed out that the rare tautomers of DNA bases might disturb the genetic code.<sup>1</sup> In 1963, Löwdin proposed the proton tunneling model of the origin of spontaneous mutations in the DNA base pairs.<sup>2</sup> Since then, the proton-transfer reaction has been extensively investigated with double hydrogen-bonded model molecules. The 7-azaindole dimer (7-AI<sub>2</sub>) has been considered as a model DNA base pair, and it is one of the most widely studied double hydrogen-bonded dimers.<sup>3,4,5,6,7,8,9,10,11,12</sup> Taylor, El-Bayoumi, and Kasha<sup>13</sup> were the first to observe the excited-state double-proton transfer (ESDPT) reaction in 7-AI<sub>2</sub> by measuring the fluorescence spectrum in solution. Numerous studies have focused on the mechanisms of ESDPT in 7-AI<sub>2</sub> in solution, matrix, and in the gas phase using various spectroscopic techniques. Theoretical studies have been carried out to investigate the hydrogen-bonded structures, potential energy surface, and molecular dynamics of 7AI<sub>2</sub>. It has been proposed that ESDPT is the main concept to explain the dynamical process.

Although numerous attempts have been made to clarify the mechanism, the conclusion is still controversial. Two mechanisms have been proposed for ESDPT in 7-AI<sub>2</sub>. Zewail and co-workers carried out the femtosecond time-resolved experiments by detecting the transient ions in a molecular beam.<sup>5</sup> They obtained decay profiles of the normal dimer (base pair) and its isotopomers by varying the excess energy in the S<sub>1</sub>-S<sub>0</sub> region. Each decay profile was fitted to a bi-exponential function. Two time constants 650 fs and 3.3 ps were obtained when the excess energy is near zero. The short and long decay components were ascribed to a single-proton transfer from the

normal dimer to a zwitterionic state (intermediate state?) and from the intermediate state to the tautomer, respectively (Fig. 1). They proposed a “stepwise mechanism” (or sequential mechanism).

The other mechanism of ESDPT is “concerted mechanism” (Fig. 1), which was proposed by Kasha and co-workers from a quantum mechanical intuition and steady-state electronic spectra in solution. They consider that the excitation is delocalized on the two monomer units in the lowest excited state of 7-AI<sub>2</sub> due to a strong exciton resonance interaction. According to Kasha, Catala'n, and co-workers's work, the geometry of 7-AI<sub>2</sub> in the lowest excited state is C<sub>2h</sub> since the two monomer units are equivalent, therefore, the two protons should move simultaneously on a potential energy surface that has no potential minimum between the geometry of initially excited and the tautomer.

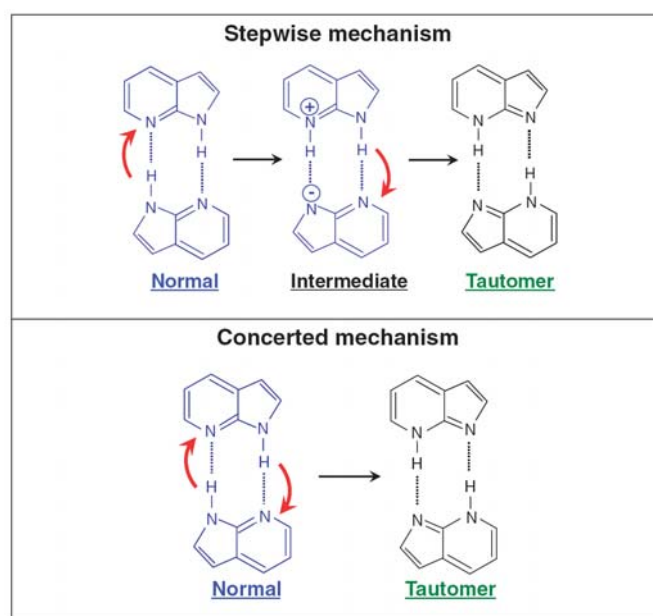


Fig. 1. Two mechanisms of ESDPT in 7-AI<sub>2</sub>. The normal dimer undergoes single-proton transfer by photoexcitation to produce a stable zwitterionic state followed by second proton transfer to generate the tautomer in stepwise mechanism. Two protons simultaneously transfer by photoexcitation of the normal dimer in the concerted mechanism, where no stable intermediate state exists. (Adopted from ref. 12)

The mechanism of ESDPT in 7-AI<sub>2</sub> in solution was extensively studied by two groups. Takeuchi and Tahara carried out femtosecond fluorescence up-conversion measurement in solution. They examined the decay profiles by varying the excitation energy. When the pump photon provided excess energies, each decay profile was fitted to a bi-exponential function. However, a single exponential decay was observed

when the red-edge of the  $S_1$ – $S_0$  absorption was excited. The single exponential decay was ascribed to the concerted mechanism. Zewail and co-workers also investigated ESDPT in solution with femtosecond fluorescence up-conversion and the transient absorption measurements. They obtained similar time constants to those of Takeuchi and Tahara. The long decay component (1–1.1 ps) was assigned to ESDPT in both research groups. However, the interpretation of the short decay component is different between these two groups. The short time constant 200 fs was ascribed to the  $S_2$ – $S_1$  electronic relaxation by Takeuchi and Tahara, but it was assigned by Fiebig et al. to the single-proton transfer occurring within 250 fs from the normal dimer to an intermediate state.

Recently, 2-aminopyridine (2-AP) dimer offers alternative interest to investigate the excited-state dynamics of H-transfer reaction. Ab initio calculations characterized the potential energy surface for the locally excited  $^1\pi\pi^*$  (LE) and charge transfer  $^1\pi\pi^*$  (CT) states of the planar AP dimer along the intermolecular hydrogen transfer coordinate, as shown in Fig. 2.<sup>14</sup> According to the calculations, an electron transfer from one aminopyridine molecule to the other (LE  $\rightarrow$  CT transition) should be followed by a proton transfer along the N-H coordinate, leading to a net hydrogen transfer. The electron-proton transfer thus creates a pathway for rapid excited-state relaxation of optically bright electronic states.

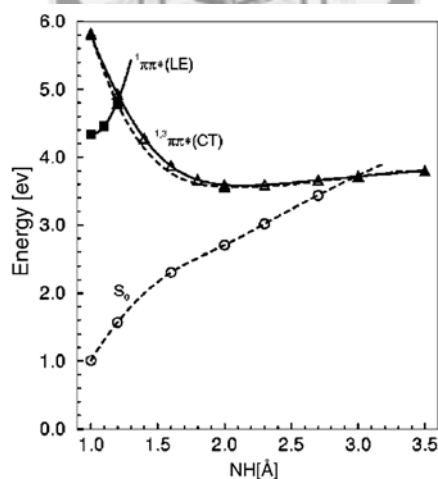


Fig. 2. MRMP2 minimum-energy profiles of the lowest  $^1\pi\pi^*$  (LE) state (solid squares) and the lowest  $^3\pi\pi^*$  (CT) state (triangles) of the 2-AP dimer, calculated as a function of the NH-stretch reaction coordinate. The energies of the  $^1\pi\pi^*$  (CT) state (solid triangles) and the ground state (circles) were calculated at the geometry of the  $^3\pi\pi^*$  (CT) state. (Adopted from ref. 13)

Femtosecond pump-probe spectroscopy<sup>15</sup> of  $(2\text{-AP})_n$  clusters confirmed the theoretical prediction of fast excited-state relaxation mediated by H-transfer. Upon

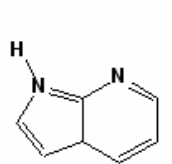


excitation by 274 nm photons, the monomer ( $n = 1$ ) and larger clusters  $n \geq 4$  show a lifetime of  $\tau_1 = 1.5$  ns, equal to the radiative lifetime estimated from high-resolution spectra of the monomer.<sup>16</sup> The dimer displayed a much shorter lifetime of  $\tau_2 = 65$  ps, which was assigned to the H-transfer relaxation channel in the near-planar, doubly hydrogen-bonded structure. For the trimer, both the long-lived  $\tau_1$  and the short-lived  $\tau_2$  contributions were observed and assigned to different cluster geometries.

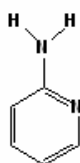
Compared with 7-AI<sub>2</sub>, 2-AP<sub>2</sub> was also verified as a net H-atom transfer (electro-coupled-proton transfer) instead of proton (H<sup>+</sup>) transfer. The new model of non-radiative decay of this aromatic biomolecules includes the repulsive  $\pi \sigma^*$  state. The H-atom transfer on the excited state could be recognized as  $\langle i \rangle$  the deactivation from the optical bright state ( $\pi \pi^*$  state) to the dark state ( repulsive  $\pi \sigma^*$  state or  $^1\pi\pi^*$  charge-transfer states ) through conical intersection,  $\langle ii \rangle$  then, a repulsive potential along with the N-H/O-H stretch reaction coordinate resulted a fast release of a H-atom.

Another model molecule of DNA base, 8-hydroxyquinoline (8-HQ), has also been discussed.<sup>17,18,19</sup> The proximity of the two functional groups in 8-HQ is similar to that observed in 7-azaindole. Therefore, the similar ESPT mechanisms are expected. Besides, the reactivities of both functional groups already exhibited in a cooperative way in the ground state, especially when 8-HQ forms a complex with metal ions. 8-HQ is an outstanding complexing agent, a bidentate ligand, considered as the second chelating agent in importance after EDTA.<sup>20</sup> Besides its chelating properties, 8-HQ is a fluorogenic ligand; i.e., it shows a very low quantum yield in aqueous and organic solutions. Fluorescence arises from cation binding with most metal ions. It is then used for fluorimetric determination of metals.<sup>21</sup> However, this fluorogenic character is not yet fully understood. In particular, the very low fluorescence emission in most media has never been really explained.

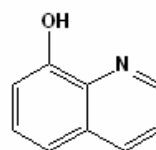
In this chapter, we provide the experimental evidence to prove the existence of repulsive potential on the 7-azaindole and 2-aminopyridine for the first time. Together with these studies, the 8-hydroxyquinoline has also been examined to get a further understanding of the behaviors in the excited state.



**7-azaindole**



**2-aminopyridine**



**8-hydroxyquinoline**

Fig. 3. Molecular structure of 7-azaindole, 2-aminopyridine and 8-hydroxyquinoline

## Experimental

The experimental techniques have been described in chapter 2 and only a brief description is given here. 7-azaindole, 2-aminopyridine and 8-Hydroxyquinoline vapor was formed by flowing He (or Ne) at pressures of 500 Torr through a reservoir filled with solid sample at 363 K. The mixture was then expanded through a pulsed nozzle (diameter 800  $\mu\text{m}$ ) maintained at 393 K to form a molecular beam. Molecules in that beam were photodissociated with a pulsed UV laser, followed by ionization with a pulsed VUV laser at 118 nm; a pulsed electric field served to extract the ions into a mass spectrometer. At the exit port of the mass spectrometer, a two dimensional ion detector was used to detect the ion positions and intensity distribution.

## Results

### I. Photodissociation of 7-azaindole at 248 nm and 193 nm

No signal of  $m/e = 117$  ( $\text{C}_7\text{H}_5\text{N}_2^+$ ) was detected after 7-azaindole absorbed the 248 nm UV photons. Here, we only present the data of the photodissociation of 7-azaindole at 193 nm.

#### A. Photofragments and Translational Energy Distribution at 193 nm

Fragment ion of  $m/e = 117$  ( $\text{C}_7\text{H}_5\text{N}_2^+$ ) with large intensity was observed from the photodissociation of 7-azaindole at 193 nm. It corresponds to the H atom elimination. The images of  $m/e = 117$  obtained at 79  $\mu\text{s}$  delay time between pump and probe laser pulses is shown in Fig. 4. The line shape image of  $m/e = 118$  is from the residual parent molecules in the vacuum chamber. The intensity of  $m/e = 117$  is very small compared to the intensity of  $m/e = 118$ . The forward convolution in the data analysis shows that the contribution from these residual parent molecules is not important.

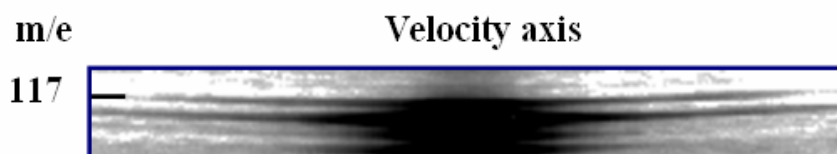


Figure 4. The ion image for  $m/e = 117$  at 79  $\mu\text{s}$  pump-probe delay time with 193 nm laser excitation

This corresponds to the  $C_7H_5N_2$  fragment with large recoil velocity. The photofragment translational energy distribution obtained from the image is shown in Fig. 5.

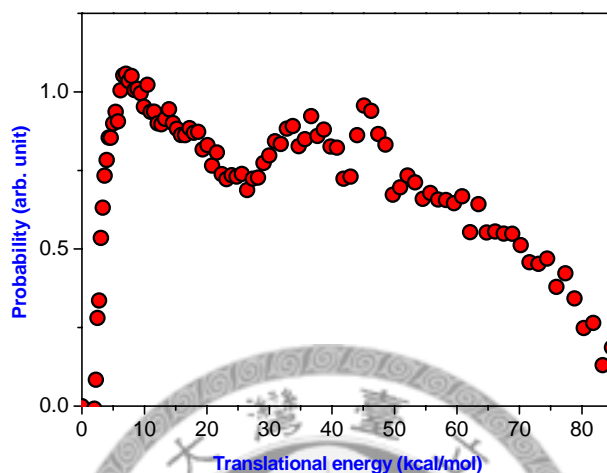
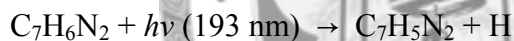


Figure 5. Photofragment translational energy distribution of reaction



It shows two components. The relative intensities between the fast and the slow components are about 1: 0.87. The average released translational energy of the fast component is large, and the peak of the distribution is located at 45 kcal/mol.

## II. Photodissociation of 2-aminopyridine at 248 nm and 193 nm

### A. Photofragments and Translational Energy Distribution at 248 nm

Fragment ion of  $m/e = 93$  ( $C_5H_5N_2^+$ ) with large intensity was observed from the photodissociation of 2-aminopyridine at 248 nm. It corresponds to the H atom elimination. The images of  $m/e = 93$  obtained at 93  $\mu\text{s}$  delay time between pump and probe laser pulses is shown in Fig. 6.

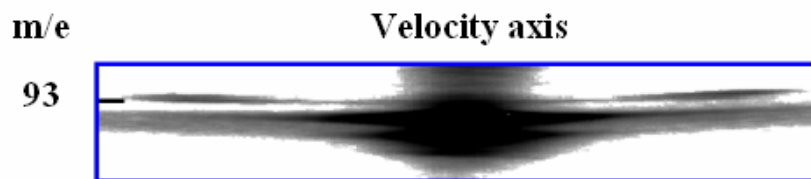


Figure 6. The ion image for  $m/e = 93$  at  $93 \mu\text{s}$  pump-probe delay time with 248 nm laser excitation

The photofragment translational energy distribution is shown in Figure 7. It also contains two components. However, the intensity of the slow component is relatively small compared to the intensity of the fast component. The slow component was estimated to be  $\sim 10\%$  of the fast component. The peak of the fast component is located at 18 kcal/mol. The translational energy as much as 30 kcal/mol can be released. It almost reaches the maximum available energy of the reaction  $\text{C}_5\text{H}_6\text{N}_2 + h\nu(248 \text{ nm}) \rightarrow \text{C}_5\text{H}_5\text{N}_2 + \text{H}$ .

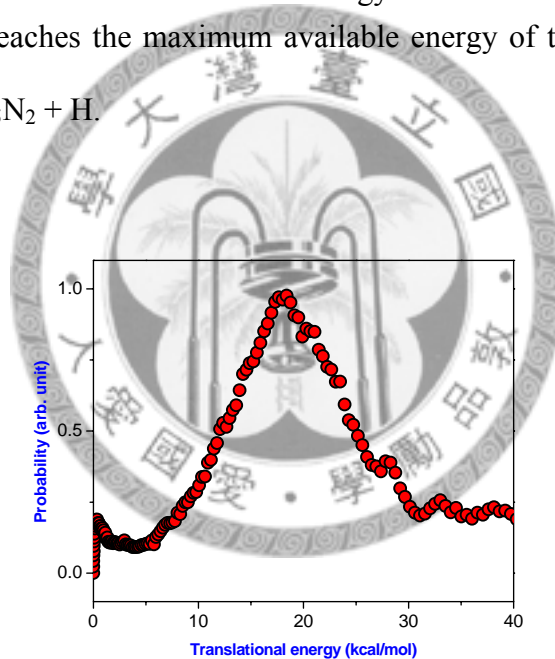
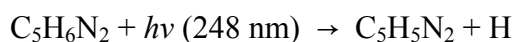


Figure 7. Photofragment translational energy distribution of reaction



### B. Photofragments and Translational Energy Distribution at 193 nm

Fragment ion of  $m/e = 93$  ( $\text{C}_5\text{H}_5\text{N}_2^+$ ) was observed from the photodissociation of 2-aminopyridine at 193 nm. It corresponds to the H atom elimination. The images of  $m/e = 93$  obtained at  $61 \mu\text{s}$  delay time between pump and probe laser pulses is shown in Fig. 8. Another line image of  $m/e = 92$  had been observed. Due to the slow recoil

velocity, it was assigned as the cracking of slow component (small translational energy, large internal energy) of  $m/e = 93$  ( $C_5H_5N_2$ ) after ionizing by 118 nm laser.

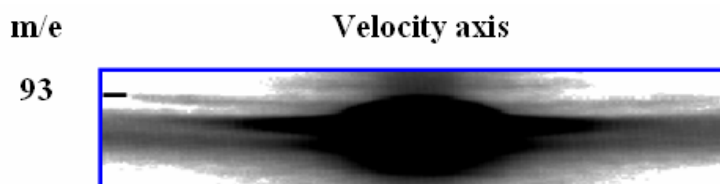


Figure 8. The ion image for  $m/e = 93$  at 61  $\mu s$  pump–probe delay time with 193 nm laser excitation. The  $m/e = 92$  line image is from the dissociative ionization of  $m/e = 93$ .

Since the cracking of  $m/e = 93$  ( $C_5H_5N_2$ ) into  $m/e = 92$  is the H loss, the image intensity profile of  $m/e = 92$  would not change significantly. It can be directly added onto the image intensity profile of  $m/e = 93$  without any correction. The reason is that the mass ratio of  $m/e = 92$  and H is enormous. Even though there is a recoil-kick from H to  $m/e = 92$ , it will not cause huge change on the velocity of  $m/e = 92$ . In other words,  $m/e = 92$  will stay in the same velocity distribution as  $m/e = 93$  before cracking. The photofragment translational energy distribution was taken into account the distribution of  $m/e = 92$ , as shown in Figure 9. It also contains two components. The slow component was estimated to be  $\sim 30\%$  of the fast component.

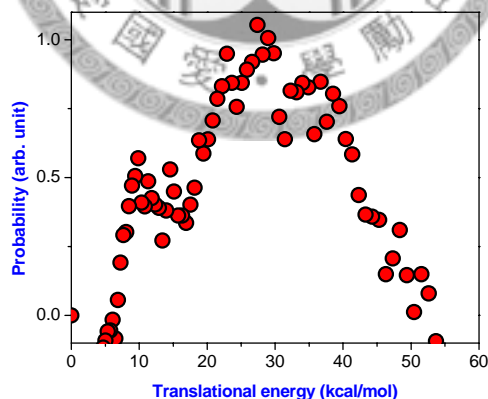
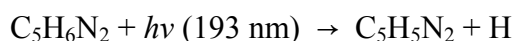


Figure 9. Photofragment translational energy distribution of reaction



### III. The photodissociation of 8-Hydroxyquinoline at 248 nm and 193 nm

## A. Photofragments and Translational Energy Distribution at 248 nm

Fragment ion of  $m/e = 144$  ( $C_9H_6NO^+$ ) was observed from the photodissociation of 8-Hydroxyquinoline at 248 nm. It corresponds to the H atom elimination. The images of  $m/e = 144$  obtained at 120  $\mu s$  delay time between pump and probe laser pulses is shown in Fig. 10.

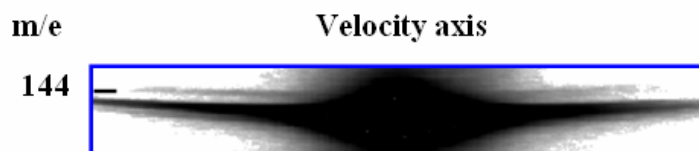


Figure 10. The ion image for  $m/e = 144$  at 120  $\mu s$  pump-probe delay time with 248 nm laser excitation

The line shape image of  $m/e = 145$  is from the residual parent molecules in the vacuum chamber. The intensity is very small compared to the intensity of the molecular beam. The forward convolution in the data analysis shows that the contribution from these residual parent molecules is not important, as stated above.

Since the available energy (equal to the photon energy minus the bond energy) at 248nm is small, the length of the image at 248nm is very short. Although the experimental delay time between pump and probe laser pulses increases to 120  $\mu s$ , the length of the image of  $m/e = 144$  is still not very long due to the small available energy. The center part of the image is therefore interfered by the image of parent molecules. The photofragment translational energy is shown in Figure 11. The slow and fast components are not separated clearly. The uncertainty of the slow component is relatively large due the large background from parent molecules. The slow component was estimated to be 1.6 times of the fast component. The peak of the fast component is located at 25 kcal/mol. The translational energy as much as 47 kcal/mol can be released. It almost reaches the maximum available energy of the reaction

$$C_9H_7NO + h\nu (248 \text{ nm}) \rightarrow C_9H_6NO + H.$$

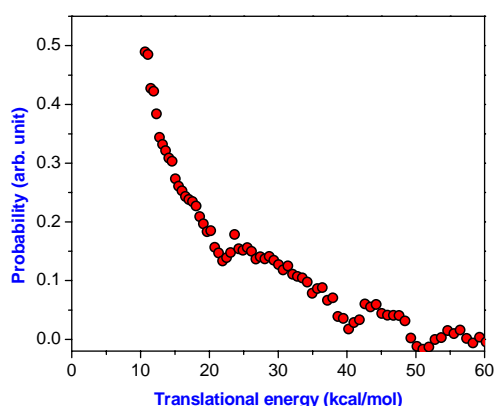


Figure 11. Photofragment translational energy distribution of reaction  $C_9H_7NO + h\nu$  (248 nm)  $\rightarrow C_9H_6NO + H$ . The data with energy less than 10 kcal/mol which is interfered with the parent molecules is not shown in the figure.

### B. Photofragments and Translational Energy Distribution at 193 nm

Fragment ion of  $m/e = 144$  ( $C_9H_6NO^+$ ) with large intensity was observed from the photodissociation of 8-hydroxyquinoline at 193 nm. It corresponds to the H atom elimination. The images of  $m/e = 144$  obtained at 80  $\mu s$  delay time between pump and probe laser pulses is shown in Fig. 12.

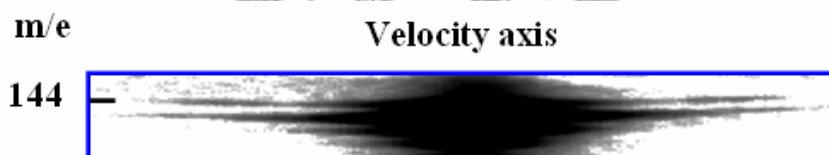


Figure 12. The ion image for  $m/e = 144$  at 80  $\mu s$  pump–probe delay time with 193 nm laser excitation

The photofragment translational energy is shown in Figure 13. It also contains two components. The slow component was estimated to be 2.5 times of the fast component. The peak of the fast component is located at 55 kcal/mol. The translational energy as much as 80 kcal/mol can be released. It almost reaches the maximum available energy of the reaction  $C_9H_7NO + h\nu$  (193 nm)  $\rightarrow C_9H_6NO + H$ .

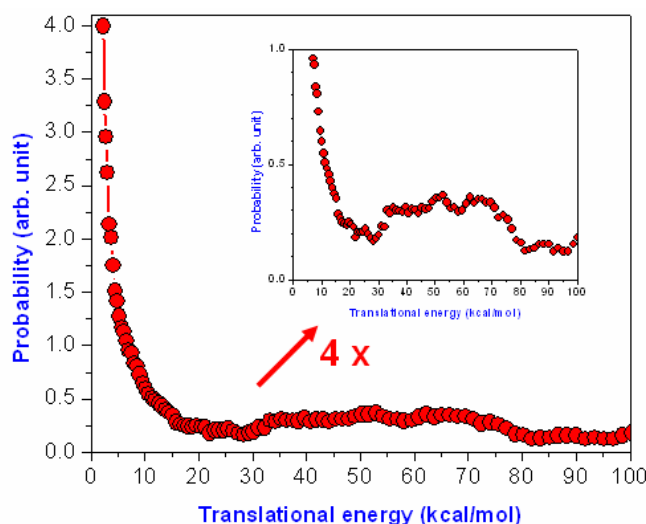


Figure 13. Photofragment translational energy distribution of reaction  $C_9H_7NO + h\nu$  (193 nm)  $\rightarrow C_9H_6NO + H$ . The data with energy less than 2 kcal/mol which is interfered with the parent molecules is not shown in the figure.

## Discussion

One of the important characteristics of the heteroaromatic molecules is the low quantum yields of fluorescence. The existence of fast nonradiative process was assumed to account for the efficient quenching of the excited state. The internal conversion through  $n\pi^*$  and  $\pi\pi^*$  in the DNA base, e.g. adenine, has been suggested to explain the “photostability” of genetic code<sup>22,23</sup>. The DNA bases relax to the ground state by internal conversion. They dissipate the photon energy to the surrounding molecules and prevent the breaking of chemical bond. Along with these studies, the ultrafast conical intersection from the initial excited state (bright state) to the  $\pi\sigma^*$  state (dark state) has also been suggested<sup>24,25</sup>. This dynamic pathway on the  $\pi\sigma^*$  state provides a fast dissociation which can compete with the intermolecular energy transfer. Here, we study this issue by measuring the photofragment translational energy distribution to understand the photodynamic behavior of these important molecules.

7-AI<sub>2</sub> dimer has long been considered as a DNA model of ESDPT process. Both the gas and condense phase studies are recognized a fast relaxation of 7AI<sub>2</sub>. The controversial explanations for this lie in the “concerted” or “sequential” double proton transfer in a 7-AI<sub>2</sub>. Little research has been focused on monomer. The answer that we describe here is the existence of the  $\pi\sigma^*$  state.

The first absorption band of 7-AI monomer is located in the region  $\sim 290$ nm. The second absorption band starts from 277 nm. The absorption of 248 nm and 193



nm photons corresponds to the excitation to the  $S_2$  and  $S_3$  (or  $S_4$ ) states, respectively. No obvious signal correspondent to H-atom loss channel was detected at 248 nm. Compare with the conical intersection (CI) point of adenine ( $\sim 5.5$  eV) and indole ( $\sim 4.5$  eV), it seems that the CI point of 7-AI also lie above 5eV, the photon energy of 248 nm. The two components in the translational energy distribution suggest that H atom elimination at 193 nm results from two mechanisms. The most likely interpretation is similar to the phenol dissociation mechanism: the slow component results from the ground state dissociation and the fast component results from predissociation of the repulsive state. However, dissociation from the other excited state, like triplet state, cannot be totally excluded due to the lack of the potential energy surface at this moment. From the measured translation energy distribution, the fast-component and slow-component provides an evidence of dissociation on different potential energy surfaces. The ratio of fast and slow component is equal to the branching ratio of the excited and ground state pathway. The probability of the excited state dissociation is 13 % more than that of the ground state channel. According to the experimental data, it is suggested this intrinsic molecular dynamics of 7-AI monomer could provide another aspect to realize the ESDPT mechanism of 7AI<sub>2</sub> dimer.

2-AP dimer and its isotopomer have been characterized by femtosecond time-resolved mass spectroscopy. Considerable isotope effects for the partially deuterated clusters indicate that H-atom transfer is the rate-limiting step<sup>26</sup>. Ab initio calculations of the potential energy profiles identify the mechanism: conical intersections connect the locally excited  $^1\pi\pi^*$  state and the electronic ground state with a charge-transfer  $^1\pi\pi^*$  state<sup>14</sup>. The experimental data shows that an obvious fast-component in translational energy distribution at both 248 nm and 193 nm. The observation of translational energy distribution of 2-AP monomer under UV irradiation indicates the dissociation occurs on a repulsive surface. This finding leads to consider the possibility of H-atom transfer in 2-AP dimer. Moreover, the probability of the slow component changes from  $\sim 10\%$  (at 248 nm) to  $\sim 30\%$  (at 193 nm). It indicates the internal conversion may play a more important role on the higher electronic excited states than the lower the lower ones.

Fast and slow component have also been observed in the study of 8-HQ at 248 nm and 193 nm. Again, the fast component and the slow one are the distinctive feature of the excited-state and the ground-state dissociation channels, respectively. Unlike 7-AI, 2-AP, the branching ratio of the excited state dissociation in 8-HQ is small. However, it still remains as an alternative pathway for the relaxation of the excited 8-HQ.

Nevertheless, the studies of 7-AI, 2-AP and 8-HQ investigate the possibility of

excited state dissociation by measuring the photofragment translation energy. This finding provides useful information in ab initio calculation of the excited potential surface in theoretical approach. Even though the measurement of translational energy is a time-integral technique, it has been recognized as a valid approach to investigate the ultrafast molecular dynamics. By using VUV laser and innovative multi-mass imaging technique, one can avoid the complicated interference from UV multiphoton pump/probe and the overlapping signals from the dissociative ionization and real probe-after-dissociation events. A future challenge is to find out the dissociation dynamics of the dimmers by measuring the possible recoil velocity in a molecular beam.

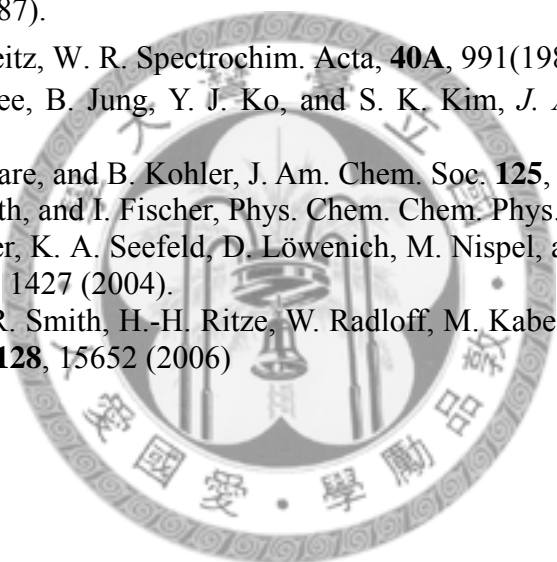
## Conclusions

The major dissociation channel for 7-azaindole, 2-aminopyridine and 8-hydroxyquinoline is the H-atom loss channel. The translational energy distribution indicates that H-atom elimination occurs in both the electronically excited and ground states. The branching ratio can be directly determined by velocity distribution. It provides the information of the bifurcation on the excited state.

## References

- <sup>1</sup> J. D. Watson, F. H. C. Crick, *Nature*, **171**, 737 (1953).
- <sup>2</sup> P.O. Löwdin, *Rev. Mol. Phys.*, **35**, 724 (1963).
- <sup>3</sup> S. Takeuchi, T. Tahara, *Chem. Phys. Lett.*, **347**, 108(2001).
- <sup>4</sup> T. Fiebig, M. Chachisvilis, M. Manger, A. H. Zewail, A. Douhal, I. Garcia-Ochoa, A. de La Hoz Ayuso, *J. Phys. Chem. A*, **103**, 7419(1999).
- <sup>5</sup> A. Douhal, S. K. Kim, A. H. Zewail, *Nature*, **378**, 260(1995).
- <sup>6</sup> R. Lopez-Martens, P. Long, D. Solgadi, B. Soep, J. Syage, P. Millie, *Chem. Phys. Lett.*, **273**, 219(1997).
- <sup>7</sup> D. E. Folmer, E. S. Wisniewski, A. W. Castleman, Jr., *Chem. Phys. Lett.*, **318**, 637(2000).
- <sup>8</sup> K. Sakota, C. Okabe, N. Nishi, H. Sekiya, *J. Phys. Chem. A*, **109**, 5245(2005).
- <sup>9</sup> J. Catala'n, J. C. del Valle, M. Kasha, *Proc. Natl. Acad. Sci. U.S.A.*, **96**, 8338(1999).
- <sup>10</sup> J. Catala'n, J. C. del Valle, M. Kasha, *Proc. Natl. Acad. Sci. U.S.A.*, **99**, 5799(2002).
- <sup>11</sup> Chou, P. T.; Wei, C. Y.; Chang, C. P.; Kuo, M. S. *J. Phys. Chem.*, **99**, 11994(1995).
- <sup>12</sup> Pi-Tai Chou, Marty L. Martinez, William C. Cooper, Dale McMorrow, Susan T.

- 
- Collins, and Michael Kasha, *J. Phys. Chem.*, **96**, 5203(1992)
- <sup>13</sup> C. A. Taylor, M. A. El-Bayoumi, M. Kasha, *Proc. Natl. Acad. Sci. U.S.A.*, **63**, 253(1969).
- <sup>14</sup> Sobolewski, A. L.; Domcke, W. *Chem. Phys.*, **294**, 73(2003).
- <sup>15</sup> Schultz, T.; Samoylova, E.; Radloff, W.; Hertel, I. V.; Sobolewski, A. L.; Domcke, W. *Science*, **306**, 1765(2004).
- <sup>16</sup> Borst, D. R.; Roscioli, J. R.; Pratt, D. W. *J. Phys. Chem. A*, **106**, 4022(2002).
- <sup>17</sup> Elisabeth Bardez, Isabelle Devol, Bernadette Larrey, and Bernard Valeur, *J. Phys. Chem. B*, **101**, 7786(1997)
- <sup>18</sup> Quan-Song Li and Wei-Hai Fang, *Chem. Phys. Lett.*, **367**, 637(2003).
- <sup>19</sup> Christopher M. Cheatum<sup>1</sup>, Max M. Heckscher and F. Fleming Crim, *Chem. Phys. Lett.*, **349**, 37(2001)
- <sup>20</sup> Soroka, K.; Vithanage, R. S.; Phillips, D. A.; Walker, B.; Dasgupta, P. K., *Anal. Chem.*, **59**, 629(1987).
- <sup>21</sup> Dowling, S. D.; Seitz, W. R. *Spectrochim. Acta*, **40A**, 991(1984).
- <sup>22</sup> H. Kang, K. T. Lee, B. Jung, Y. J. Ko, and S. K. Kim, *J. Am. Chem. Soc.* **124**, 12958 (2002)
- <sup>23</sup> B. Cohen, P. M. Hare, and B. Kohler, *J. Am. Chem. Soc.* **125**, 13594 (2003).
- <sup>24</sup> M. Zierhut, W. Roth, and I. Fischer, *Phys. Chem. Chem. Phys.* **6**, 5178 (2004).
- <sup>25</sup> I. Hünig, C. Plützer, K. A. Seefeld, D. Löwenich, M. Nispel, and K. Kleinermanns, *ChemPhysChem* **5**, 1427 (2004).
- <sup>26</sup> E. Samoylova, V.R. Smith, H.-H. Ritze, W. Radloff, M. Kabelac, and T. Schultz, *J. Am. Chem. Soc.* **128**, 15652 (2006)



## Curriculum vitae

### Personal information:

Full name: 曾建銘 (Chien-Ming Tseng), Jimmy Tseng

Institute of Atomic and Molecular Sciences, Academia Sinica

Address: P. O. Box 23-166, Lab 320, Taipei, Taiwan 10617

Tel: +886-2-23668268 (lab); Fax: +886-2-23620200

Born: Kaohsiung County, Taiwan, 1977/08/26

2000 B.S. National Taiwan University

2002 M.S. National Taiwan University

2003 Research Assistant in Institute of Atomic and Molecular Science

Dr. Chi. Kung Ni's Lab. (Defense Industry Reserve Duty System service)

2008 Ph.D. National Taiwan University,

Thesis adviser: Pro. Yuan T. Lee and Chi-Kung Ni

The research topic: Photodissociation dynamics of aromatic and bio-molecules  
studied by multimass ion imaging

Award: The 2006 Annual Best Article in Journal of the Chinese Chemical Society.

“Chien-Ming Tseng, Yuri A. Dyakov, Cheng-Liang Huang, Yuan T. Lee, Sheng Hsien Lin, and Chi-Kung Ni, *The role of seven-membered ring in the photoisomerization and photodissociation of small aromatic molecules*, J. Chin. Chem. Soc. 53, 33 (2006).”

### Publications:

1. Chun-Cing Chen, Hsing-Chen Wu, Chien-Ming Tseng, Yi-Han Yang, and Yit-Tsong Chen, *One- and two-photon excitation vibronic spectra of 2-methylallyl radical at 4.6-5.6 eV*, J. Chem. Phys. **119**, 241 (2003)
2. Chien-Ming Tseng, Cheng-Liang Huang, Yuan T. Lee, and Chi-Kung Ni, *Multimass ion imaging detection: Application to photodissociation.*, The Chinese Chem Soc., **61**, 401 (2003).
3. Cheng-Ming Tzeng, Y. M. Choi, Cheng-Liang Huang, Chi-Kung Ni, Yuan T. Lee, and M. C. Lin, *Photodissociation of nitrosobenzene and decomposition of phenyl radical*, J. Phys. Chem. A. **108**, 7928 (2004).
4. Chien-Ming Tseng, Yuri A. Dyakov, Cheng-Liang Huang, Alexander M. Mebel, Sheng Hsien Lin, Yuan T. Lee, and Chi-Kung Ni, *Photoisomerization and photodissociation of aniline and 4-methylpyridine*,

- J. Am. Chem. Soc. **126**, 8760 (2004).
5. Chien-Ming Tseng, Yuan T. Lee, and Chi-Kung Ni, *H atom elimination from the  $\pi \sigma^*$  state in the photodissociation of phenol*, J. Chem. Phys. **121**, 2459 (2004) (communication)
  6. Ming-Fu Lin, Yuri A. Dyakov, Chien-Ming Tseng, Alexander M. Mebel, Sheng Hsien Lin, Yuan T. Lee, and Chi-Kung Ni, *Photodissociation dynamics of pyridine*, J. Chem. Phys. **123**, 054309 (2005).
  7. Ming-Fu Lin, Chien-Ming Tseng, Yuan T. Lee, and Chi-Kung Ni, *Photodissociation dynamics of indole in a molecular beam*, J. Chem. Phys. **123**, 124303 (2005).
  8. Chien-Ming Tseng, Yuri A. Dyakov, Cheng-Liang Huang, Yuan T. Lee, Sheng Hsien Lin, and Chi-Kung Ni, *The role of seven-membered ring in the photoisomerization and photodissociation of small aromatic molecules*, J. Chin. Chem. Soc. **53**, 33 (2006).
  9. Ming-Fu Lin, Yuri A. Dyakov, Chien-Ming Tseng, Alexander M. Mebel, Sheng Hsien Lin, Yuan T. Lee, and Chi-Kung Ni, *Photodissociation dynamics of pyrimidine*, J. Chem. Phys. **124**, 084303 (2006).
  10. Cheng-Liang Huang, Jyh-Chiang Jiang, Yuri A. Dyakov, Ming-Fu Lin, Chien-Ming Tseng, S. H. Lin, Yuan T. Lee, and Chi-Kung Ni, *Photodissociation and photoisomerization of  $\alpha$ -fluorotoluene and 4-fluorotoluene in a molecular beam*, J. Chem. Phys. **125**, 133305 (2006).
  11. Ming-Fu Lin, Cheng-Ming Tseng, Yuri A. Dyakov, and Chi-Kung Ni, *Photostability of amino acids: Internal conversion versus dissociation*, J. Chem. Phys. **126**, 241104 (2007).
  12. Cheng-Ming Tseng, Yuan T. Lee, Chi-Kung Ni, Jia-Lin Chang, *Photodissociation dynamics of the chromophores of the amino acid tyrosine: *p*-methylphenol, *p*-ethylphenol, and *p*-(2-Aminoethyl)phenol*, J. Phys. Chem. A. **111**, 6674 (2007)
  13. Cheng-Ming Tseng, Yuan T. Lee, Ming-Fu Lin, Chi-Kung Ni, Suet-Yi Liu, Yuan-Pern Le, Z. F. Xu, and M.C. Lin, *Photodissociation of phenol*, J. Phys. Chem. A. **111**, 9463 (2007)
  14. Chi-Kung Ni, Cheng-Ming Tseng, Ming-Fu Lin, and Yuri A. Dyakov, *Photodissociation dynamics of small aromatic molecules Studied by multimass ion imaging*, J. Phys. Chem. B. **111**, 12631(2007) (Feature article).
  15. Cheng-Ming Tseng, Yuan T. Lee, Ming-Fu Lin, Chi-Kung Ni, *Photodissociation of 1-naphthol*, Mol. Phys. **106**, 233(2008).